Numerical investigation of different tip shapes for wind turbine blades. Aerodynamic and aeroacoustic aspects

Aagaard Madsen, H.; Fuglsang, P.

Publication date:
1997

Document Version
Publisher's PDF, also known as Version of record

RISØ

Risø-R-891(EN)

Numerical Investigation of Different Tip Shapes for Wind Turbine Blades

Aerodynamic and Aeroacoustic Aspects

Helge Aagaard Madsen, Peter Fuglsang

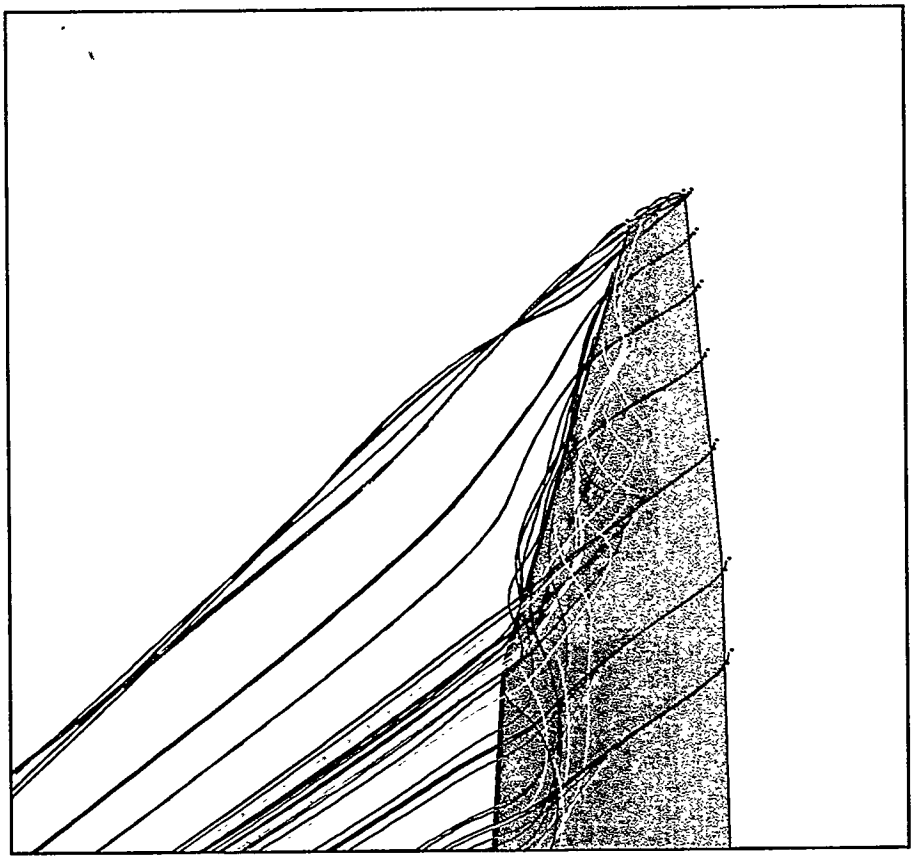

Risø National Laboratory, Roskilde, Denmark
December 1996

Risø-R-891(EN)

Numerical Investigation of Different Tip Shapes for Wind Turbine Blades

Aerodynamic and Aeroacoustic Aspects

Helge Aagaard Madsen, Peter Fuglsang

Risø National Laboratory, Roskilde, Denmark
December 1996

Abstract
Aspects of the aerodynamics and aeroacoustics related to the design of the tip region of wind turbine blades are treated in the present report.

The aerodynamic optimization of the tip region is discussed and it is concluded that in principle there is no main difference to the optimization problem of the rest of the blade except that the performance of the aerodynamic models as, e.g., the blade element momentum theory (BEM) is more uncertain in this region due to the complex, three dimensional flow field. It is shown that an optimization of an entire blade in general leads to a slender tip with a chord decreasing to zero at the blade tip. Finally, the influence on the blade aerodynamics from minor changes of the planform in the tip region is illustrated.

Two common aeroacoustic models are reviewed. The aerodynamic input parameters to both models are the strength of the tip vortex and the length of the separated flow bubble formed by the tip vortex at the trailing edge. In the original aeroacoustic models these two parameters are calculated from empirical relations based on different experiments, e.g., using flow visualization. In the present work the two parameters was compared with the results of a CFD calculation of the flow around a rectangular shaped tip. The principal influence of sweep of the tip axis has also been investigated from detailed CFD simulations. It is found that sweeping the leading edge towards the trailing edge results in a stronger flow separation at moderate and high angles of attack compared to, when the trailing edge is swept towards the leading edge. This can have a considerable influence on the total loading on the blade. Similar tendencies have been found in full scale experiments.

At the end of the report the application of the results from the present study are discussed for practical tip design. As the tip noise is linked to the strength of the tip vortex and the extension of the separation region these two parameters should be reduced in order to lower the tip noise. Finally, a blade tip design with a nonseparating tip vortex (NSTV tip) is sketched and proposed as one way to reduce the tip noise.

The EFP program of the Danish Ministry of Energy supported the present work under the contracts:

ENS-1364/93-0006 "Aerodynamisk Støj"
ENS-1364/93-0001 "Rotor Aerodynamik"
ENS-1363/95-0001 "Vingeprojekt"

This report has passed an internal review at the Test Station for Wind Turbines, Risø performed by

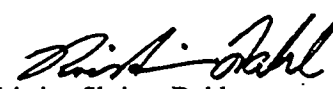

Kristian Skriver Dahl

Flemming Rasmussen

ISBN 87-550-2177-8
ISSN 0106-2840

Grafisk Service, Risø, 1996

Contents

1. Introduction

In recent years the aerodynamic performance of wind turbine blades has been improved considerably. This has contributed to an overall reduction in the cost of wind power produced electricity. The most pronounced changes in the aerodynamic design have been in the planform of the blades. Design trends are towards increased tip speed and slender blades with less weight and less material consumption. More recently, new airfoil designs have been introduced with performance characteristics tailored to the specific requirements on a wind turbine blade.

The tip section of the blade is important for the overall aerodynamic as well as the aeroacoustic characteristics. Many different blade tip designs have been proposed and used until now. However, in general the design and analysis tools used for blade design do not resolve the details of the complex flow at the tip and therefore, the tip design has mainly been based on intuition and experiments.

A considerable experimental research has been carried out on blade tip aerodynamics and aeroacoustics within the last 5-10 years. In a project funded by the Danish Ministry of Energy and the Commission of the European Communities, seven different tip shapes were tested in full scale on a 300 kW turbine, **Jakobsen and Andersen (1993)**. Both noise measurements and aerodynamic measurements were carried out. One of the main findings was that the so-called O-gee tip reduced the total A-weighted noise with 2-3 dB. The same tips have been tested stationary in a wind tunnel at DEWI in Germany, **Bareiss et al. (1993)**. The preliminary wind tunnel results, however, do not correlate fully with the field data. In another project acoustic and aerodynamic measurements on a full scale turbine was carried out at the University of Stuttgart, and the O-gee tip was found to generate more noise than the reference tip, **Bareiss (1995)**.

Five different tip shapes were tested on a full scale 100 kW turbine at Risø in a project funded by the Danish Ministry of energy and the Commission of the European Communities. One of the three blades was modified so that the tip segment (about half a meter in the spanwise length) could be mounted on a balance enabling the measurement of the aerodynamic forces on the tip. Because only one tip was changed the use of a near field or focusing measurement technique was investigated. Using a gate width of 40 degrees of azimuth rotation, the noise spectra for the different blade tips could be compared, **Antoniou et al. (1993)**. The A-weighted noise in the frequency band from 2-5 kHz seemed to be lower for the O-gee tip but the interpretation is somewhat uncertain (it is mentioned that the window of 40 degrees might be too narrow). The aerodynamic measurements from the same experiments were presented by **Antoniou et al. (1994)** and flapwise blade root moments and power output were shown as function of measured angle of attack. For particular one of the tips (the swept, tapered tip) a significant influence on the flapwise blade root moment from the tip shape was seen in the stall and post stall area.

A considerable amount of innovation and experimental work is done on the tip design in the wind turbine industry. For competitive reasons much of this work is not published but recently **Petersen et al. (1993)** briefly described some of the means used by Bonus for noise control on a 450 kW turbine. As concerns the tip design a small torpedo is used to reduce the noise from the tip region.

The intentions with the present study is to investigate the aerodynamics and the aeroacoustics of three different tip shapes in order to suggest improvements on the tip design of modern wind turbines. The state of the art in aeroacoustic modeling of the tip flow is given. Detailed numerical aerodynamic calculations of the flow around different tip shapes are performed to study both the aerodynamic and aeroacoustic characteristics of the different tip shapes. The flow is computed with a general purpose CFD (computational fluid dynamics) solver for two and three dimensional flows. All the computations have been performed on a nonrotating tip in order to simplify the complex flow problem. Particularly in the separated regions the rotation has some influence on the flow field but on the other hand the gross effect on the flow from the tip design is expected to be valid with the present type of computation. Furthermore it allows for a relative comparison of the flow for the different tip shapes.

The outline of the report is as follows:

Chapter 2: Aspects of blade and tip design related to the lifting line models, that are often used for blade design.

Chapter 3: Aeroacoustic models for the noise emission from the tip section.

Chapter 4: Mesh generation and the governing equations for the numerical calculations of the tip flow.

Chapter 5: Numerical results for the tip flow near-field for three different tip shapes, using a general purpose CFD solver.

Chapter 6: Conclusions and design guide lines for reduction of the tip noise.

2. BLADE TIP AERODYNAMICS

The flow at the blade tip is a complex three-dimensional flow. It is often associated with some flow separation. This means that also viscous effects are important. Therefore, simple flow models (e.g. models for potential flow) will not resolve the full details of the flow. On the other hand, the gross flow effect from the tip which is the shed vorticity from the finite span forming the tip vortices is captured by such simple methods as, e.g., lifting line or lifting panel models. The shed vorticity induces flow at the blade which influences the effective angle of attack and hence the aerodynamic loading on the blade. A lifting line model which models the influence from the shed vorticity is therefore expected to predict the variation of the loading along the blade reasonably well, whereas the flow field close to the blade will not be correct.

2.1 Aerodynamic design aspects of the tip shape

A wide variety of tip shapes have been used on commercial blades so far. The main reason for this is probably that there is no firm basis for design of tips and therefore tip design is mostly based on intuition and experimental experiences. Aerodynamic and aeroacoustic characteristics for 7 different tip designs, Figure 2-1 were measured by **Jakobsen and Andersen (1993)** in a series of full scale measurements on a 300 kW turbine. The standard tip shape is shown to the left in Figure 2-1. Most of the tips are tapered and swept back towards the trailing edge, tip E and I whereas tip J is more like a delta wing. Tip O, the O-gee tip is tapered and swept forward towards the leading edge. Tip M is extended with a torpedo, for capturing the tip vortex.

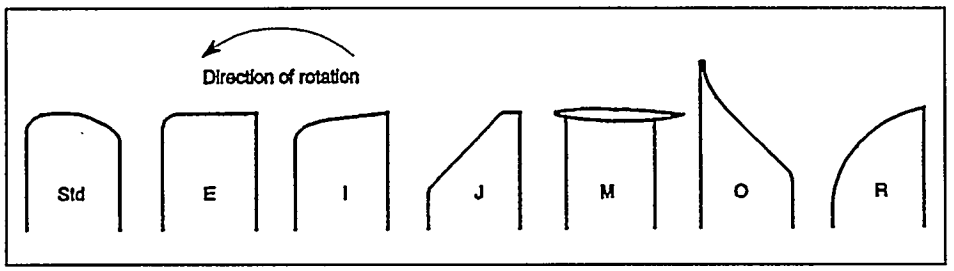

Figure 2-1 *Different tip designs tested by Jakobsen and Andersen (1993) in full scale measurements on a 300 kW turbine.*

In principle, the aerodynamic design of the tip region is not different from the rest of the blade as concerns the design goals or objectives. One design approach for blades has been to design for a constant induction factor along the blade at a fixed design wind speed to maximize the rotor power efficiency. This single point approach can of course be used also in the tip region to give the planform and twist distribution but with the important restriction that the results from the applied aerodynamic theory, the blade element momentum (BEM) theory, is uncertain in this region. Another approach which is not much different is to optimize the local aerodynamic performance along the blade at a certain fixed wind speed, again using BEM theory. This design approach has been used by **Madsen (1994)** to design a 12.6 m rotor.

Recently, a new optimization and design model for blades has been developed at Risø, **Fuglsang and Madsen (1995)**. Here, the design of the blade is optimized in order to minimize the cost of the produced energy. One of the basic differences from the above mentioned approaches is, that with the latter method, the final optimized design is not the one with maximum aerodynamic efficiency in a single design point, but a result of minimization of some design objective. This objective is often chosen as the cost per produced energy unit, which basically depends on both the production (efficiency) and the extreme and fatigue loads. Again this method can be used in the tip region but with the same uncertainty related to the BEM method as mentioned above. As an example is shown the chord and twist distribution for an optimized 28 m blade, Figure 2-2, Figure 2-3 and Figure 2-4, based on the approach of **Madsen (1994)** and **Fuglsang and Madsen (1995).** It is seen that the blade based on the multipoint optimization procedure is more slender in the tip region, due to the constraints on loads. However, both design procedures tend to reduce the chord almost to zero, resulting in a tapered tip, which is different from most of the industrial designs, at least the designs which are a few years old.

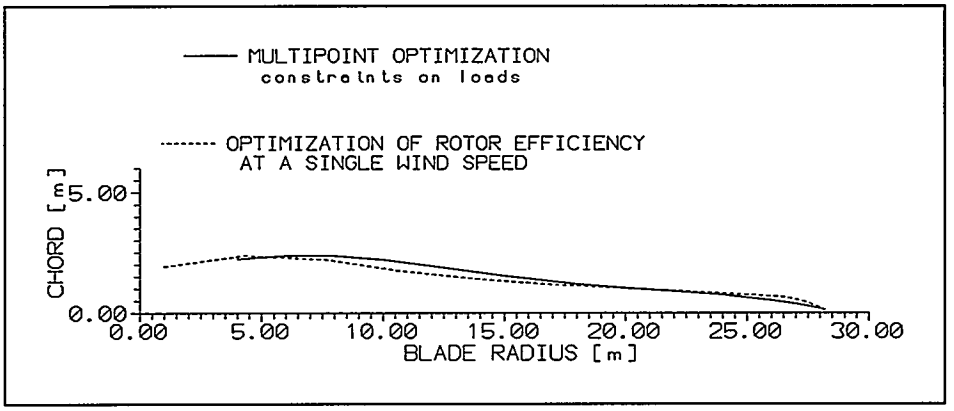

Figure 2-2 *Comparison of the resulting blade planform from a single point and a multipoint design approach.*

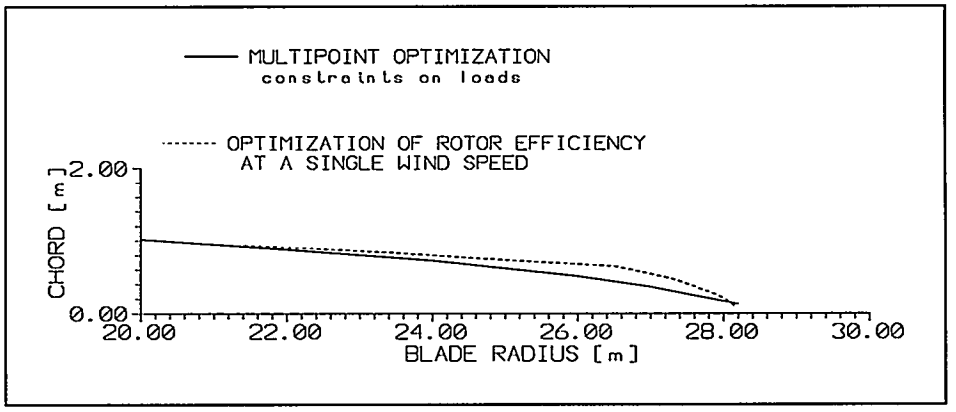

Figure 2-3 *Detail of Figure 2.2 showing the design of planform in the tip region.*

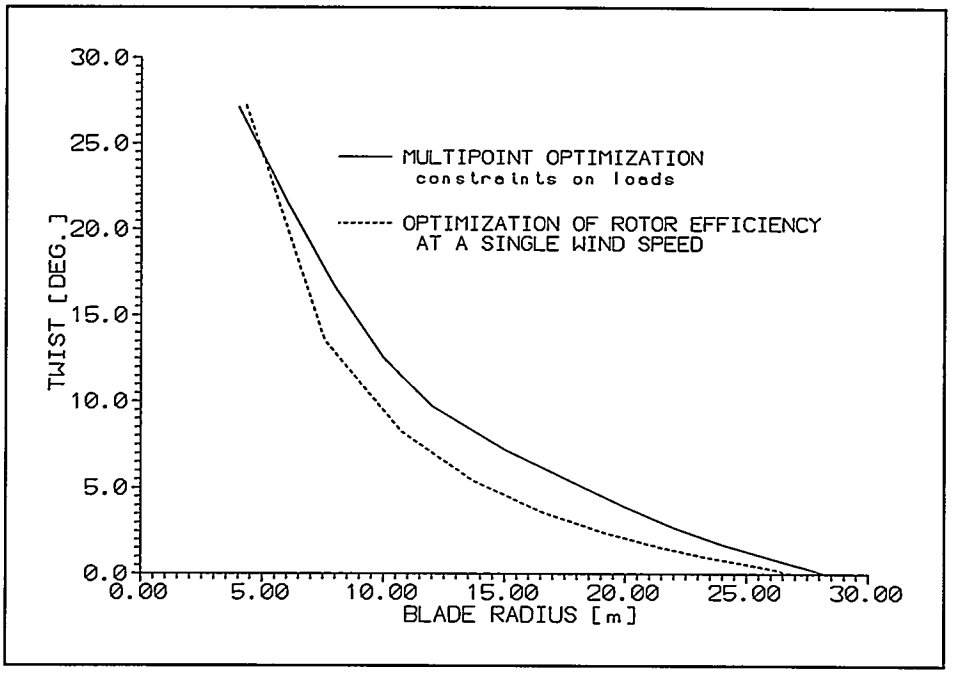

Figure 2-4 *The twist distribution resulting from a single point and a multipoint design approach.*

The principal differences between the tapered tip and the rectangular tip is further elaborated in Figure 2-5 , Figure 2-6, Figure 2-7 and Figure 2-8. In Figure 2-5, the two designs are compared and the only difference is in the tip region where design 1 is tapered and design 2 has a rectangular tip planform. The latter design has a higher loading in the tip region and therefore a more abrupt decrease of the bound circulation to zero as seen in the comparison of the circulation in Figure 2-6. This results in a stronger and more concentrated tip vortex as the strength of the tip vortex is proportional to the radial derivative of the bound circulation, Figure 2-7 and Figure 2-8. At angles of attack before stall, the strong shed vorticity for the rectangular tip reduces the effective incidence considerably, Figure 2-6, and thus also the lift coefficient in the tip region, Figure 2-8.

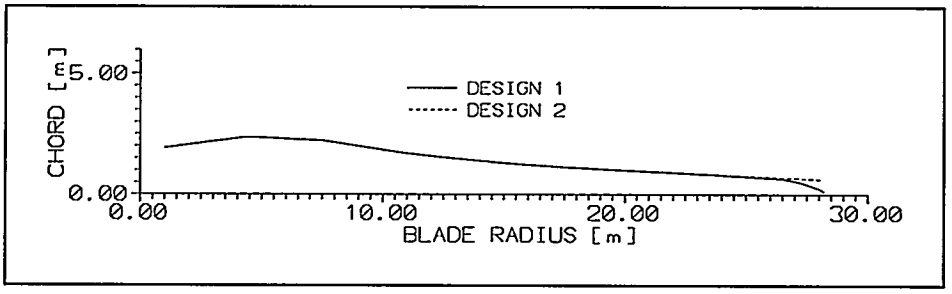

Figure 2-5 *Comparison of two different tip designs, a tapered tip and a rectangular tip.*

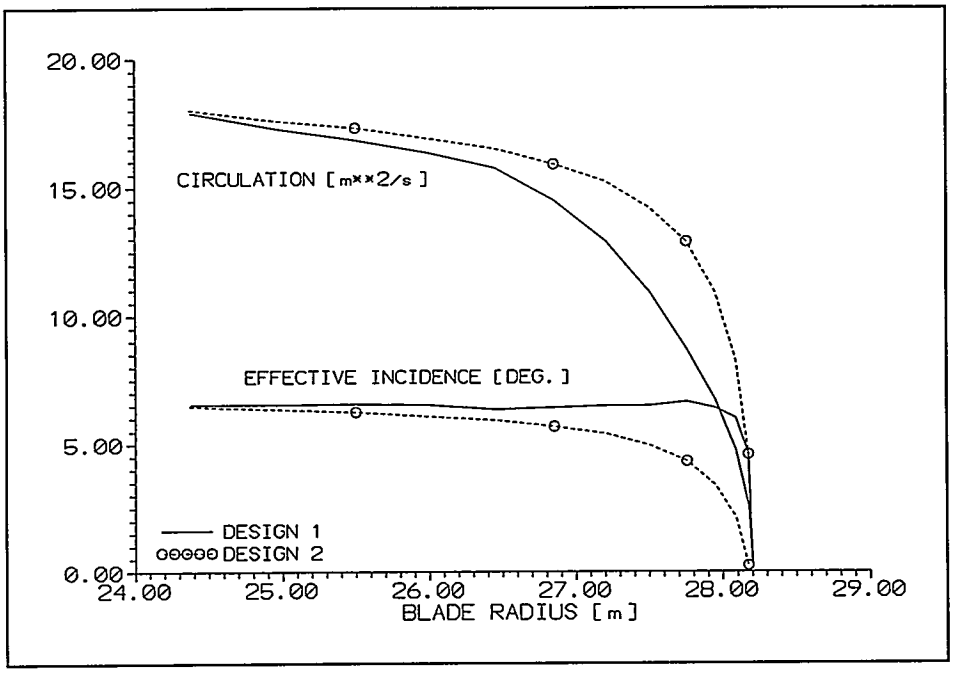

Figure 2-6 *Comparison of the circulation and the effective incidence for the two tip designs shown in Figure 2.5. Wind speed 8 m/s.*

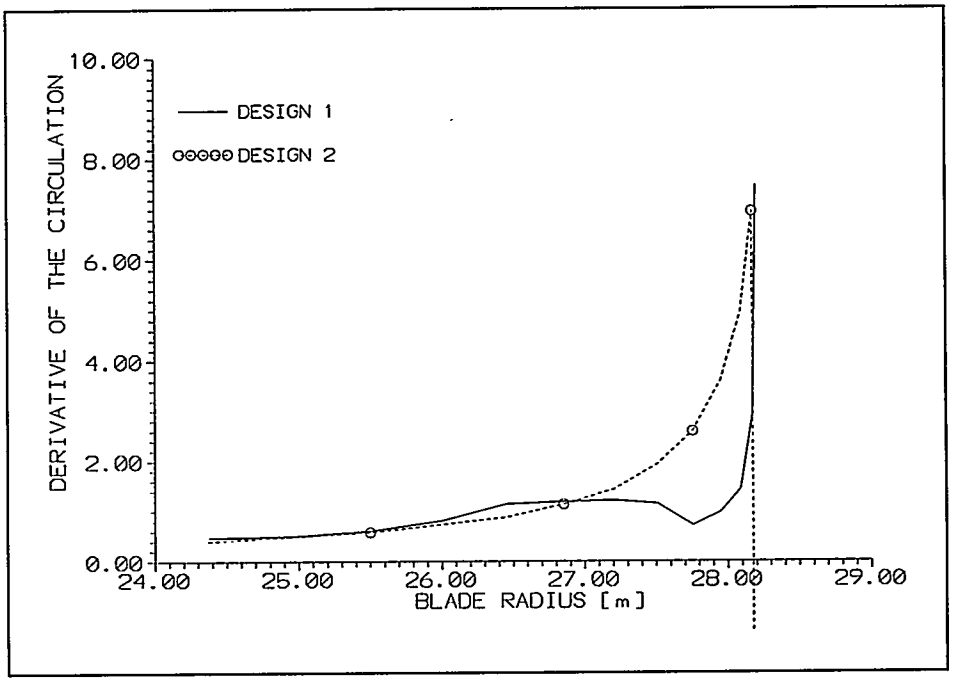

Figure 2-7 *Comparison of the derivative of the bound circulation for the two tip designs shown in Figure 2-5 (strength of the shed vorticity).*

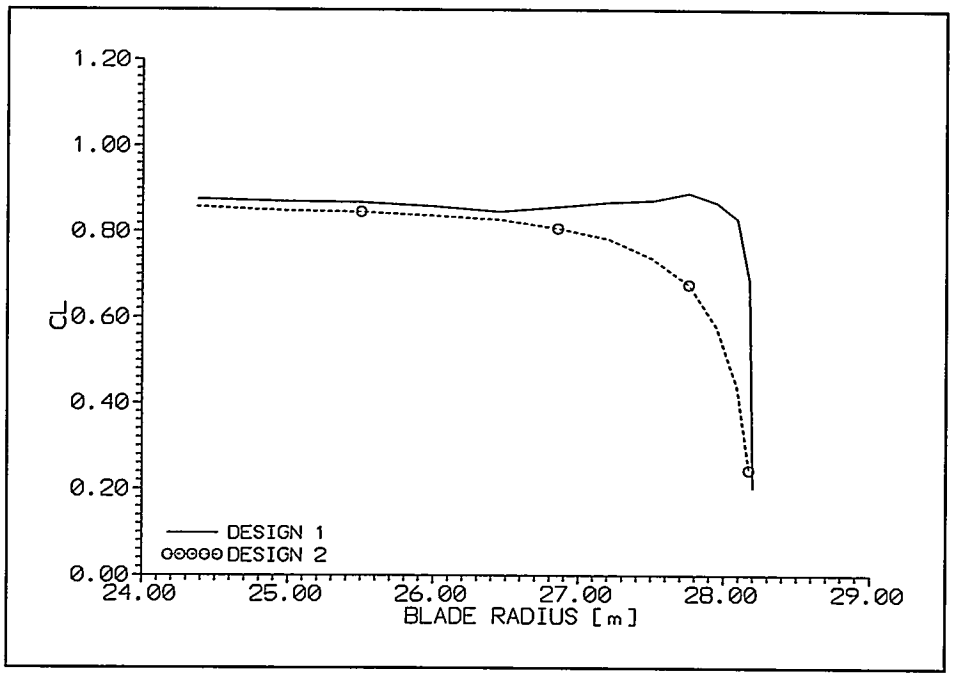

Figure 2-8 *Comparison of the CL distribution for the two tip designs shown in Figure 2-5. Wind speed 8 m/s.*

Contour plots of the tip vortex strength are shown in Figure 2-9 and Figure 2-10. It appears clearly that the rectangular tip has a stronger and more concentrated tip vortex compared to the tapered tip.

The overall blade loading and stall characteristics are therefore to some degree influenced by the particular tip design and a further discussion of advantages/disadvantages in relation to the different tip designs will be presented in Chapter 6.

The results presented above were derived with a combined lifting line/ blade element momentum code which has been developed at Risø for tip design studies. It is a fast code and can therefore be used in the design process and basically it gives the relation between the tip planform and the bound circulation. However, a straight lifting line is assumed and the code can therefore not give any information about the effect of sweeping the tip forward or backward. Likewise it can not be used to investigate the detailed layout of the tip. For such detailed modeling a full 3D model must be used and this type of modeling will be presented in Chapter 4 and 5 using a CFD code.

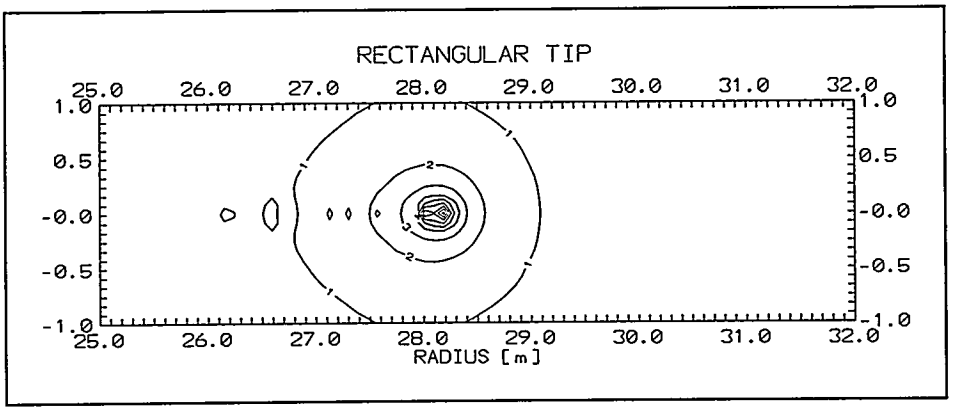

Figure 2-9 *Contour plot of the tip vortex strength (contour of the lateral velocity). Wind speed 8 m/s.*

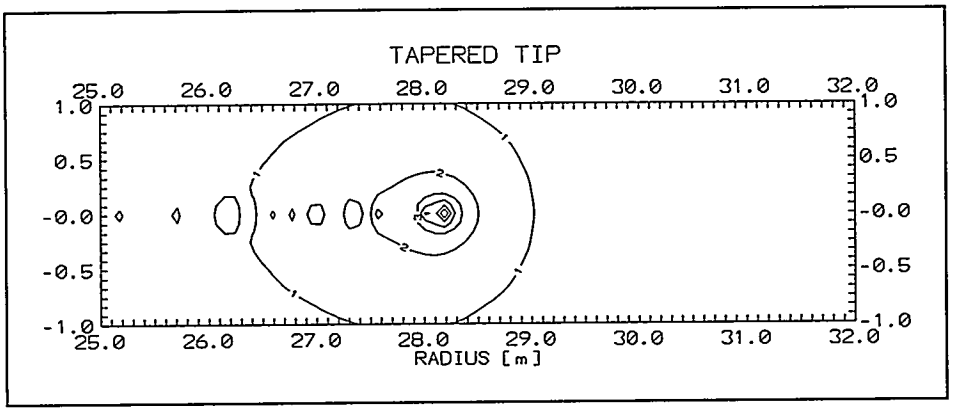

Figure 2-10 *Contour plot of the tip vortex strength (contour of the lateral velocity) Wind speed 8 m/s.*

3. Blade tip aeroacoustics

Experiments conducted in the beginning of the 1970's showed that the blade tip shape has a significant influence on the high frequency broadband aerodynamic noise from rotors. However, first in 1980, a physical model of the tip noise mechanism was proposed by **George et al. (1980)** followed by a slightly revised model in 1984 by **George and Chou (1984)**. In the same period a comprehensive experimental study of tip noise was presented by **Brooks and Marcolini (1986)** and their work also included a prediction model. Below, a short description of these two models which are rather similar will be presented. Finally, an alternative description of the tip noise mechanism will shortly be commented on.

3.1 Model of George and Chou (1984)

Due to the pressure difference, a flow is seen from the pressure side to the suction side of the blade at the tip. This is the starting point of the tip vortex, Figure 3-1.

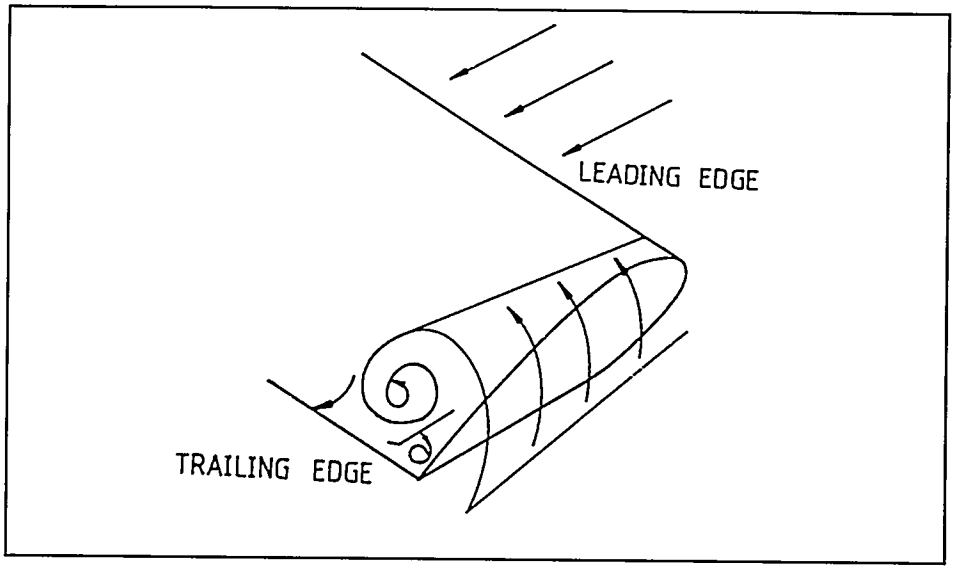

Figure 3-1 *The formation of the tip vortex flow due to the pressure difference between the lower and the upper side of the blade, **George and Chou (1984).***

This lateral flow separates at the tip and reattaches somewhat inboard on the blade suction side. Depicted in a plane perpendicular to the main flow an analogy to two-dimensional separating flow can be drawn, Figure 3-2. For such two-dimensional separating flows different investigations have shown strong pressure fluctuations at the reattachment line. To establish the correlation to the noise emission for the above model of the tip flow **George et al. (1980)** use their model for trailing edge noise, which is due to the turbulent boundary layer passing over the trailing edge.

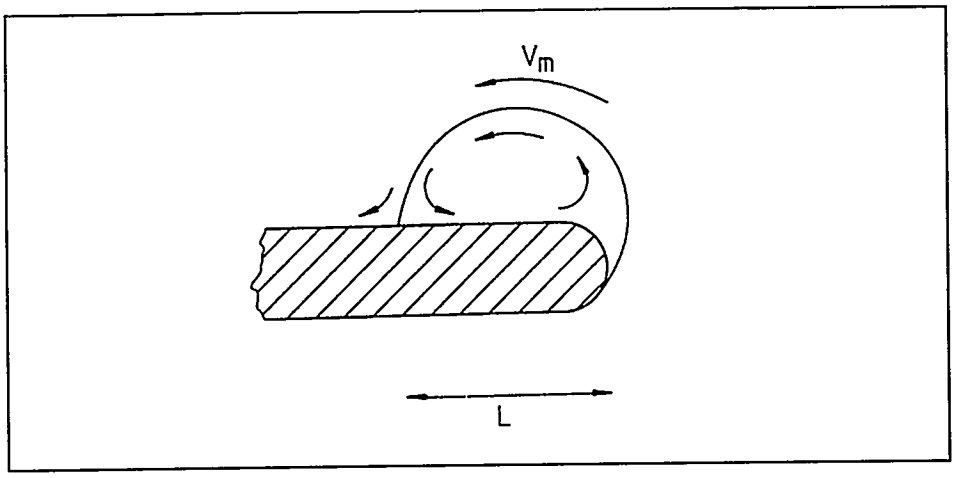

Figure 3-2 *The two main parameters describing the tip vortex, the lateral flow velocity, V_m, just outside the separation bubble and the separation length, L, at the trailing edge,* ***George and Chou (1984).***

For a rotor as shown in Figure 3-3, the far field sound pressure level from the tip vortex can according to **George et al. (1980)** and **George and Chou (1984)** be derived as:

$$\left(\left\langle S_1(x,f)\right\rangle\right) = \frac{Bf^2b^2U_c^2\sin^2\Phi}{2\pi\rho c_0^3 r^2}\sum_{n=-\infty}^{n=\infty}\frac{F_g\left(|f-n\Omega|\right)S_{pp}\left(|f-n\Omega|\right)}{(f-n\Omega)^2\left(1+\dfrac{L}{\ell_2\left(|f-n\Omega|\right)}\right)}J_n^2\left(\tfrac{f}{\Omega}M_0\cos\Phi\right)$$

(3-1)

where
- B = number of blades
- f = acoustic frequency in Hertz
- L = length of the separation bubble at the trailing edge due to the tip vortex
- U_c = turbulence convection velocity
- Φ = elevation angle of observer from the rotor plane
- ρ = density of the acoustic media
- c_0 = the undisturbed sound speed
- r = distance from rotor hub to observer
- $F_g = F^2 + G^2$
- S_{pp} = surface spectral density
- ℓ = spanwise correlation length of surface pressure

and

$$F = \left(\tfrac{\mu+M\mu+K_1}{\mu+M\mu}\right)^{1/2}\left\{\left(c_1+s_1\right)\cos 2K_1 + \left(c_1-s_1\right)\sin 2K_1\ \right\} + 1 - \left(c_2+s_2\right)$$

$$G = \left(\tfrac{\mu+M\mu+K_1}{\mu+M\mu}\right)^{1/2}\left\{\left(c_1-s_1\right)\cos 2K_1 - \left(c_1+s_1\right)\sin 2K_1\ \right\} - \left(c_2+s_2\right)$$

$$c_1 - is_1 = E^*\left[2\mu(1+M)\right]$$

$$c_2 - is_2 = E^*\left[2(\mu+\mu M+K_1)\right]$$

$$K_1 = \frac{\omega c}{2U_c} \ , \ \mu = \frac{Mk}{\beta^2}$$

The functions $E^*(\ )$ are Fresnel functions and J_n^2 is the Bessel function of first kind and order n.

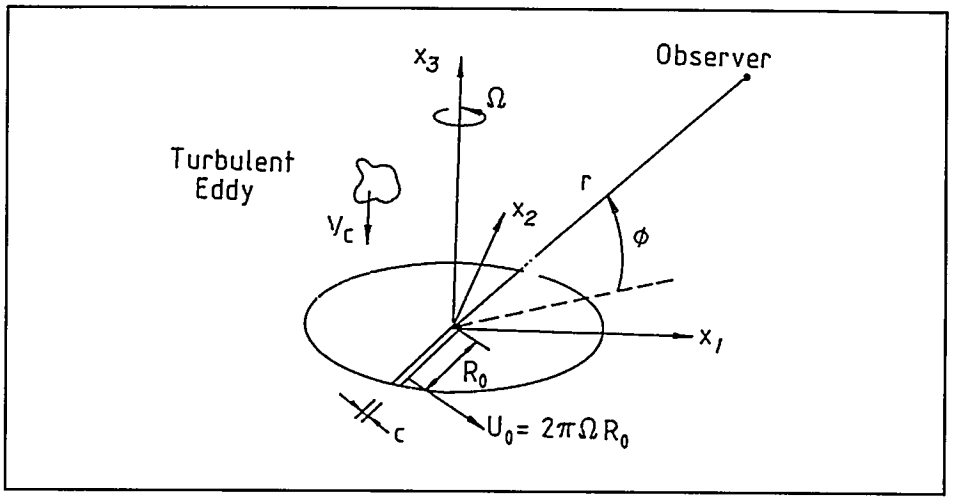

Figure 3-3 *The notation used by **George and Chou (1984)** to calculate the sound pressure level from trailing edge noise and tip noise at an observer position.*

This rather complex equation is somewhat reduced if the observer position is selected far upstream or far downstream of the rotor which means that Φ is put equal to 90^0. In this case the expression reduces to:

$$\left\langle S_1(x,f)\right\rangle = \frac{Bf^2b^2U_c^2}{2\pi\rho c_0^3 r^2}\sum_{n=-\infty}^{n=\infty}\frac{F_g(|f-n\Omega|)S_{pp}(|f-n\Omega|)}{(f-n\Omega)^2\left(1+\dfrac{b}{\ell_2(|f-n\Omega|)}\right)}J_n^2(0)$$

(3-2)

or

$$\left\langle S_1(x,f)\right\rangle = \frac{Bf^2L^2U_c^2}{2\pi\rho c_0^3 r^2}\frac{F_g(f)S_{pp}(f)}{f^2\left(1+\dfrac{L}{\ell_2(f)}\right)}$$

(3-3)

Due to the similarity between the separation of the tip vortex flow in the plane perpendicular to the main stream, Figure 3-2 and a two-dimensional separation bubble, **George and Chou (1984)** use spectra from measurements of the pressure fluctuations from different experiments. Scaling the pressure fluctuations as

$$\hat{S} = S_{pp}V_m q^{-2}L^{-1}$$

(3-4)

and

$$\hat{f} = fLV_m^{-1} \tag{3-5}$$

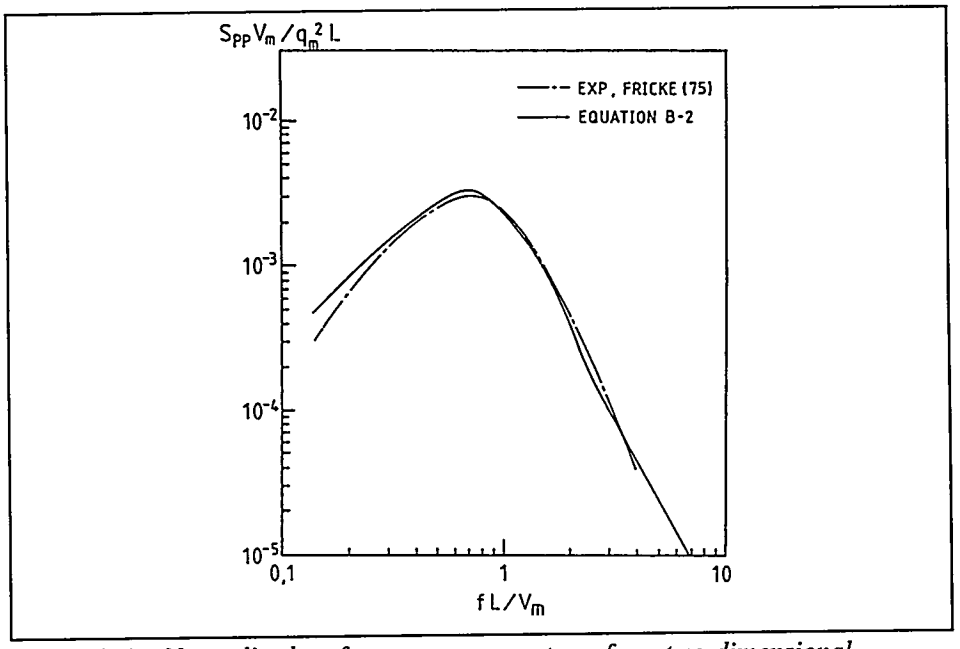

Figure 3-4 Normalized surface pressure spectrum from two-dimensional separation from **George and Chou (1984).**

a good correlation was found for rather different geometries when the length of the separation bubble L and the maximum velocity, V_m, along the separating streamline of the bubble was used as scaling parameters. They derived the following fit to the experimental data, Figure 3-4:

$$\begin{aligned}
&\hat{f} < 0.1375 && \hat{S} = 0.0;\\
&0.1375 < \hat{f} < 0.3872 && \hat{S} = 5.9703\times10^{-3}\,\hat{f} - 3.5673\times10^{-4};\\
&0.3872 < \hat{f} < 0.7935 && \hat{S} = 3.144\times10^{-3}\sin\left(3.2388\hat{f} - 0.5506\right)\\
&0.7935 < \hat{f} < 1.0605 && \hat{S} = \left(93.035 + 557.09\hat{f}\right)^{-1};\\
&1.0605 < \hat{f} && \hat{S} =\\
&\left(-258{,}896 + 1964.19\hat{f} - 2416.78\hat{f}^2 + 1288.94\hat{f}^3 - 100.862\hat{f}^4\right)^{-1};
\end{aligned} \tag{3-6}$$

Another source of pressure data used by **George and Chou (1984)** in their tip noise modeling is spectra measured at the separating leading edge vortex on a delta wing as sketched in Figure 3-5, Figure 3-6 and Figure 3-7.

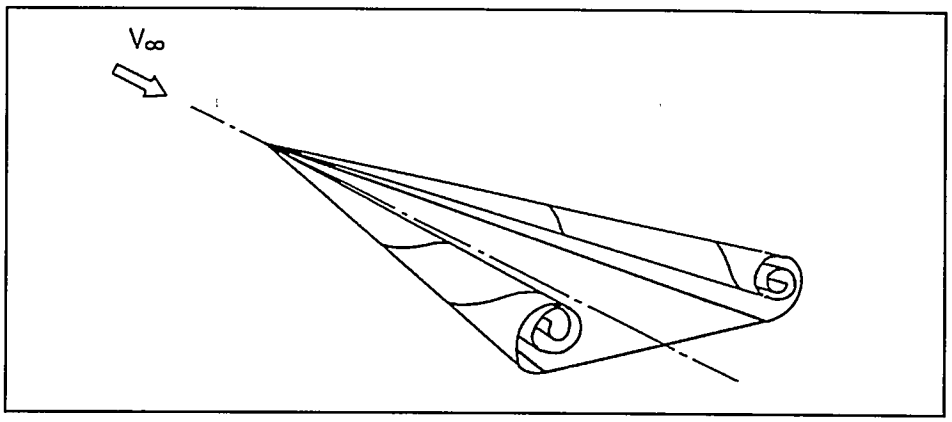

Figure 3-5 *Sketch of the formation of a leading edge vortex on a delta wing from George and Chou (1984).*

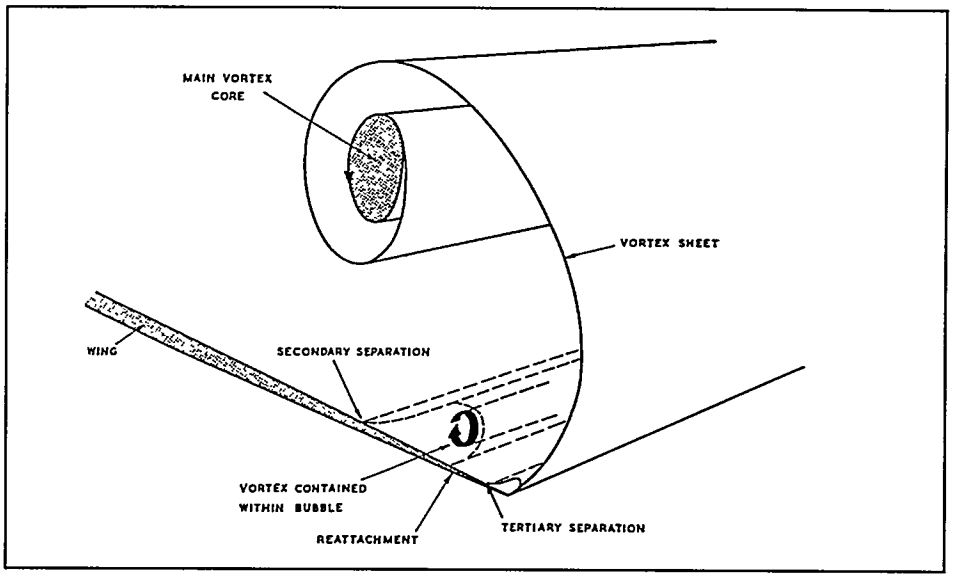

Figure 3-6 *Details of the role-up mechanism on a delta wing, Harvey (1966).*

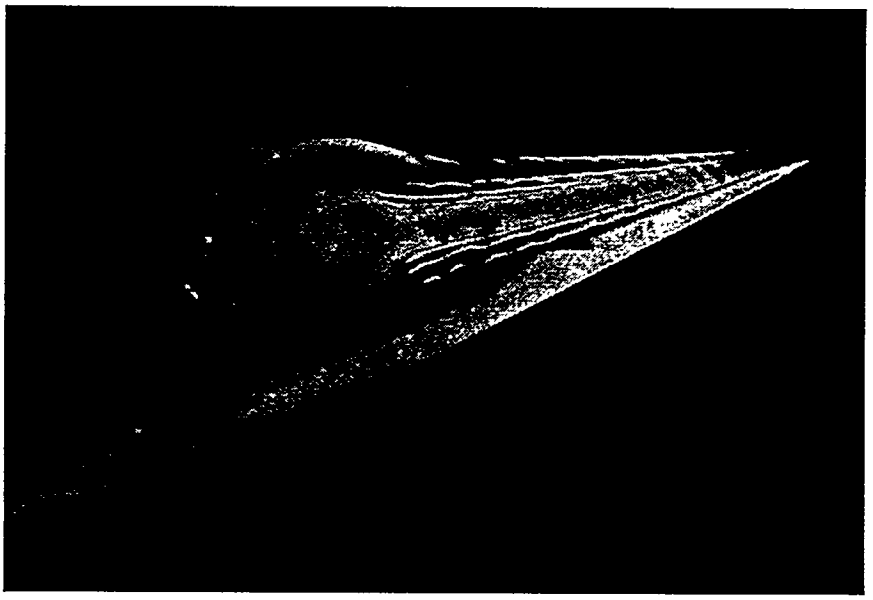

Figure 3-7 *Flow visualization of the role-up of the leading edge vortex on a delta wing, Harvey (1966).*

The flow over a delta wing is comparable with the flow over a blade tip with the leading edge swept towards the trailing edge in a steep angle. One main characteristic of the flow is the presence of a secondary tip vortex which probably is important for the generation of the fluctuating pressure. Using again the separation length L and velocity V_m for the transverse separating flow **George and Chou (1984)** correlated a number of measurements from different experiments, Figure 3-8.

They proposed the following fit to the data:

$$\log_{10} \hat{S} = -3.475 - 1.654(\log_{10} \hat{f} + 0.82)^2$$

for $\log_{10} \hat{f} \langle -0.82$

$$\log_{10} \hat{S} = -3.475 - 0.984(\log_{10} \hat{f} + 0.82)^2$$

for $\log_{10} \hat{f} \rangle -0.82$

and

$$\hat{S} = 0 \text{ for } \hat{f} \langle 0.0$$

(3-7)

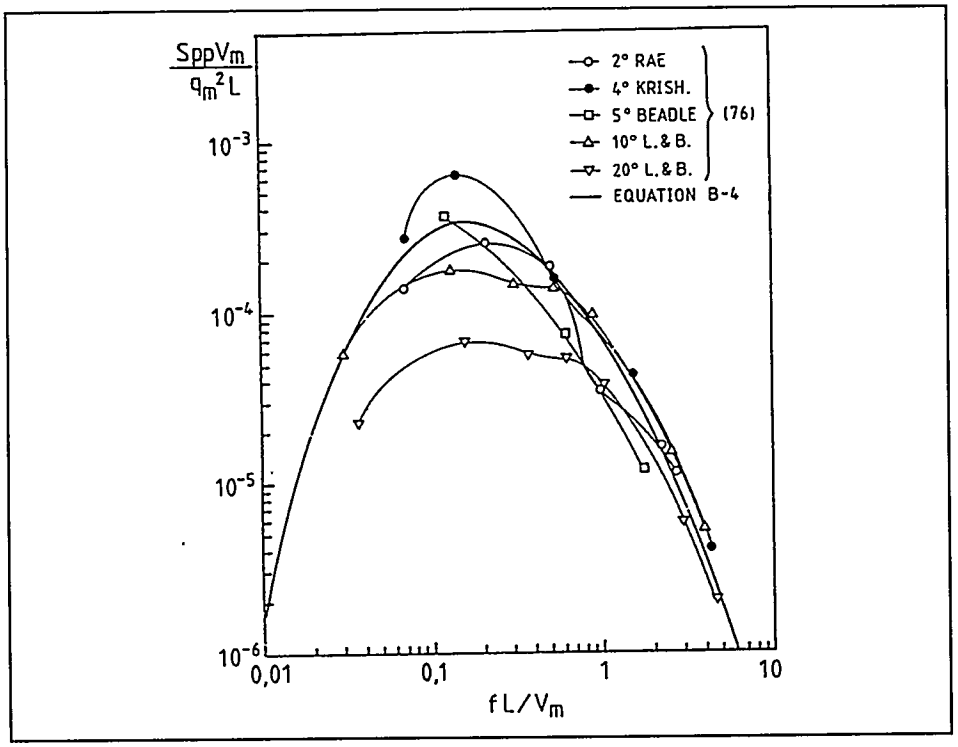

Figure 3-8 *Normalized surface pressure spectra for different delta wing experiments, **George and Chou (1984).***

To calculate the tip noise from (3-1), estimates of the tip vortex separation length L and the velocity V_m just outside the separating vortex must be derived for the blade tips at different angles of attack. **George and Chou (1984)** used flow visualization, pressure measurements and velocity measurements of **Gray et al. (1980)** and **Chigier and Corsiglia (1971)** and derived the following fits to the experimental data shown in Figure 3-9 and Figure 3-10:

$$V_m / U = 1.0 + 0.0359\alpha$$

(3-8)

where α is the local tip angle of attack in degrees.

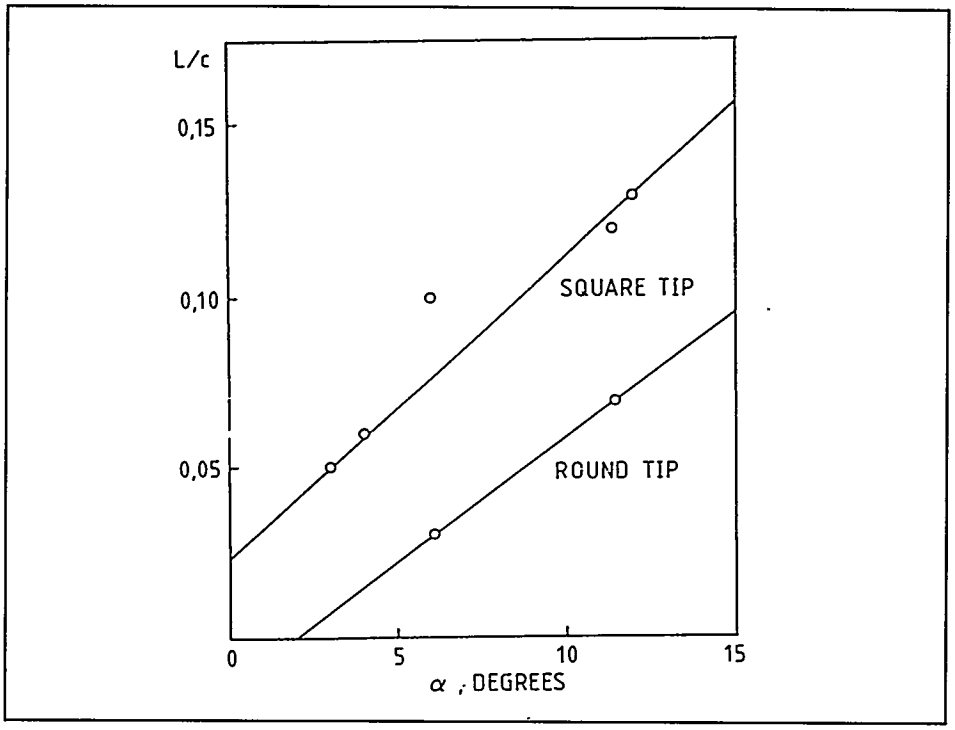

Figure 3-9 *Curve fit to the experimental data for the length L of the tip vortex separation at the trailing edge* ***George and Chou (1984).***

For the separation length L for a square tip cross section, the following expression was proposed:

$$L / c = 0.023 + 0.0089\alpha$$

(3-9)

For a rounded tip cross section, the following was proposed:

$$L / c = 0.074(\alpha - 2.0)$$

(3-10)

The above empirical relations for V_m and L will in Chapter 5 be compared with results from CFD simulations of the flow around a rectangular tip.

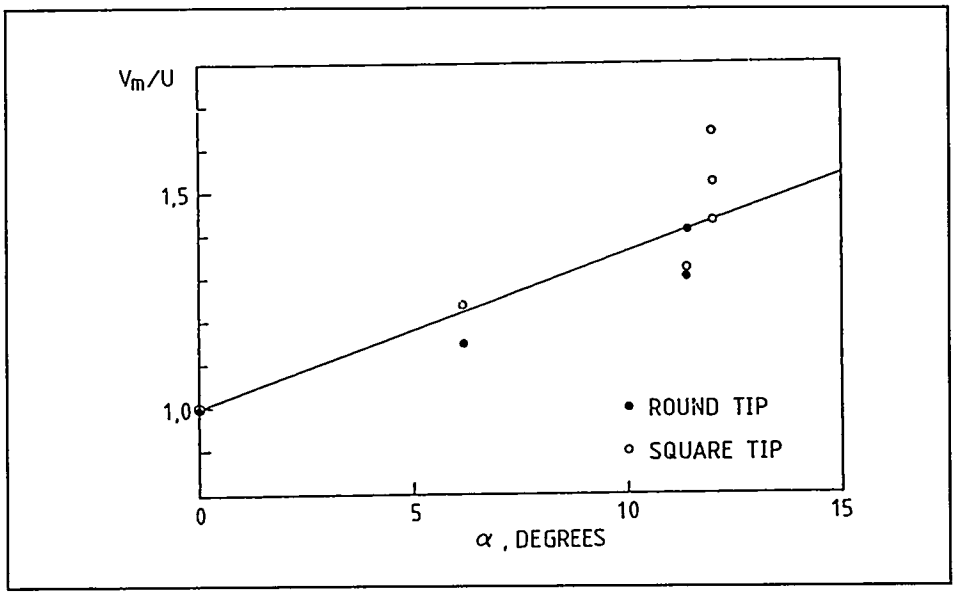

Figure 3-10 *Curve fit to the experimental data for the velocity V_m of the tip vortex flow just outside the separation bubble,* ***George and Chou (1984).***

Finally, the turbulence convection velocity U_c and the spanwise correlation length ℓ_2 have still to be determined in equation (3-1) before the tip noise can be calculated and the following relations are proposed by **George and Chou (1984)**:

$$U_c = 0.8U \tag{3-11}$$

and

$$\ell_2(\omega) = 2.1(U_c / \omega) \tag{3-12}$$

To summarize, the tip noise can now be calculated from equation(3-1) in combination with (3-8), (3-9) or (3-10), (3-11), (3-12) and one of the surface pressure fits (3-6) or (3-7).

3.2 Model of Brooks and Marcolini (1986)

Another important contribution to the tip modeling is due to **Brooks and Marcolini (1986)**. Their description of the mechanism of the generation at the tip noise by the separating vortex is in principle the same as the one described above by **George et al. (1980)**. The starting point is also a model for the trailing edge noise although somewhat different from the model of **George et al. (1980)** as they have left out the directivity. However, the main difference is now that **Brooks and Marcolini (1986)** directly measure the tip noise in a comprehensive wind tunnel experiment and use their trailing edge noise model to scale their experimental data.

Their expression for the far field sound spectrum from trailing edge noise is:

$$S(f)=\frac{1}{8\pi^2 R^2}\left(\frac{U_c L}{c_0}\right)\ell_y(f)\Phi(f)$$

(3-13)

where

U_c = turbulence convection velocity
L = spanwise extent of the edge passed by the turbulent flow
c_0 = speed of sound
$\Phi(f)$ = the power spectral density of the surface pressure fluctuations
ℓ_y = = lateral coherence of the surface pressure fluctuations

The form of the surface pressure is taken as:

$$\phi(f)=\phi(\hat{f})Lq^2/U_m$$

(3-14)

where $q=1/2\rho U_m^2$, ρ is the air density, U_m the maximum velocity along the separation streamline.

The normalization of the frequency is performed as:

$$\hat{f}=fL/U_m$$

(3-15)

For the lateral coherence of the surface pressure fluctuations the following relationship is assumed:

$$\ell_y(f)=U_c/\varsigma 2\pi f$$

(3-16)

where ς is an empirical constant.

Inserting now (3-14), (3-15) and (3-16) into (3-13) and rearranging the scaled one-third octave band pressure level "scaled $SPL_{1/3}$" can now according to **Brooks and Marcolini (1986)** be written as:

$$SPL_{1/3}-10\log\left[\frac{M^2 M_m^3 L^2}{R^2}\right]$$

$$=10\log\left[\frac{0.2308c_0^4(\rho/g)^2}{64\pi^3\zeta p_0^2}\left(\frac{M_c}{M}\right)^2\right]+10\log\phi(\hat{f})$$

(3-17)

where M, M_c and M_m are the Mach numbers corresponding to U, U_c and U_m.

The advantage of this arrangement according to **Brooks and Marcolini (1986)** is that the parameters requiring the crudest approximation, i.e. ζ, M_c and $\phi(\hat{f})$ are grouped together on the right-hand side (RHS). The left-hand side is therefore used for normalization of the measured data.

The tip noise spectra are derived by comparing noise measurements on two-dimensional airfoil models with measurements on three-dimensional models. All the tips were with a rounded edge at the tip. The difference between the noise spectra is ascribed to the tip noise and one example is presented in Figure 3-11.

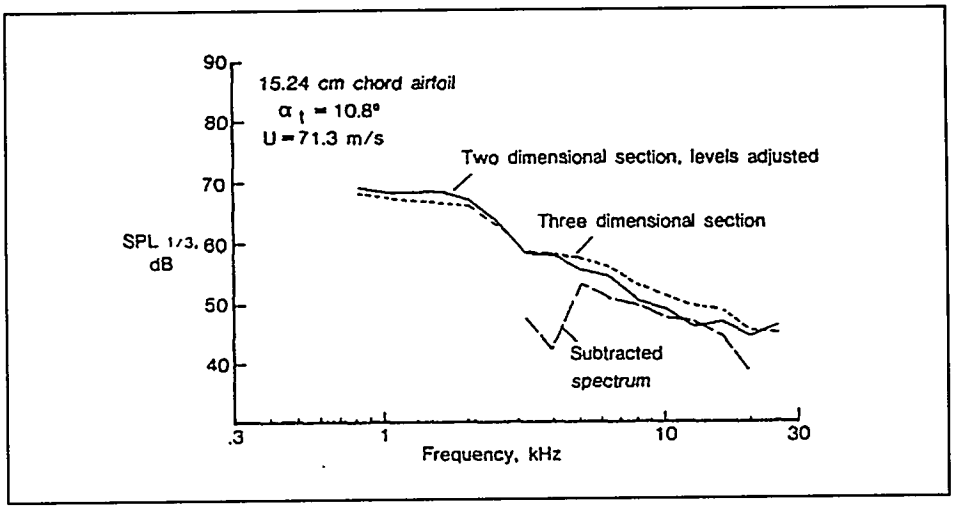

Figure 3-11 *The tip noise spectra derived as the difference between a three-dimensional and a two-dimensional wind tunnel airfoil section, **Brooks and Marcolini (1986).***

It is seen that the tip noise spectrum is only a small part of the total spectrum and this indicates that a considerable uncertainty is associated with the procedure. Besides the acoustic measurements, detailed flow measurements were carried out with hot wire equipment to determine the details of the tip vortex. On this basis the following relations for L and M_m were derived as function of angle of attack with dimension (degrees):

$$L / c \approx 0.008\alpha_{tip} \qquad (3\text{-}18)$$

and

$$M_m / M \approx \left(1 + 0.036\alpha_{tip}\right) \qquad (3\text{-}19)$$

The LHS of (3-17) with L and M_m determined by (3-18) and (3-19) is then used to normalize the measured tip noise and one example is shown in Figure 3-12.

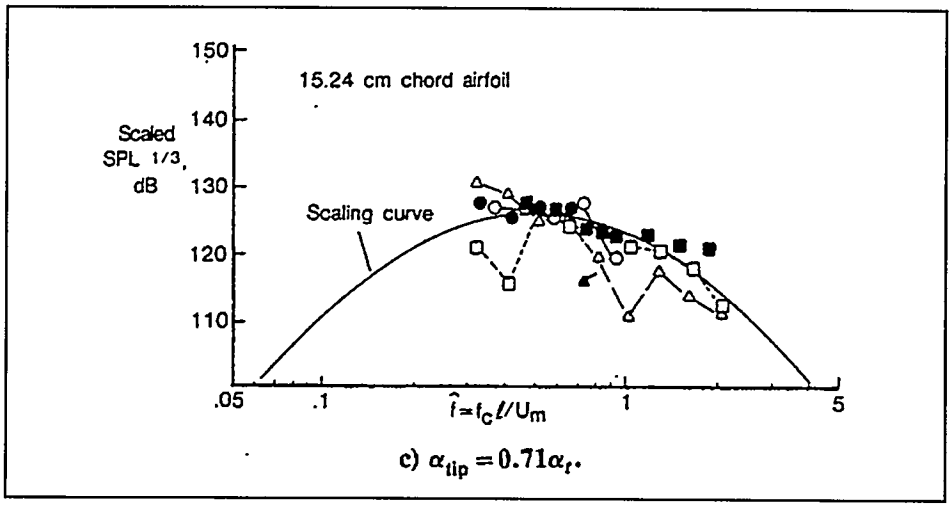

Figure 3-12 *Normalized tip noise spectra and curve fit to the data, **Brooks and Marcolini (1986).***

Based on all the normalized spectra (experiments with different chord sizes, inflow velocity and angle of attack) the following best fit to the noise spectral data was derived:

$$ScaledSPL_{1/3} = 126 - 30.5\left(\log \hat{f} + 0.3\right)^2 \qquad (3\text{-}20)$$

which is a parabolic fit about a peak Strouhal number of $\hat{f} = 0.5$.

To predict the noise the fit for the scaled sound pressure level (3-20) can now be equated to the left hand side of (3-17) and we get the following expression for prediction of the noise:

$$SPL_{1/3} = 10\log\left[\frac{M^2 M_m^3 L^2}{R^2}\right] - 30.5(\log \hat{f} + 0.3)^2 + 126 \qquad (3\text{-}21)$$

It should be noted that the hot wire measurements performed **by Brooks and Marcolini (1986)** did not confirm the expression (3-10) found by **George and Chou (1984)** for the separation length L of the tip vortex but instead they derived the fit (3-18) to their data.

However, for the maximum velocity in the separating vortex their measurements were in rough agreement (5-10 percent) with the expression (3-8) used by **George and Chou (1984)** and they propose therefore the same relationship (3-19).
Finally, it is also of interest to compare the two prediction models described above. **Brooks and Marcolini (1984)** did this by choosing the expression of **George and Chou (1984)** (3-10) for L in the normalization of their own data. If the same data set as shown in Figure 3-12 is normalized in this way it changes to the spectrum shown in Figure 3-13. It is seen that the data at the lower frequencies are stretched somewhat more in Figure 3-13.

A further comparison is possible if the pressure spectra, $\hat{S}$, (3-6), (3-7) used by **George and Chou (1984)** are inserted in eq. (3-17) for $\Phi(f)$ together with M_c = 0.8M and $\zeta = 0.48$. These scaled pressure curves are also shown in Figure 3-13 and it is clearly seen that the pressure spectra from the delta wing experiments are much closer to the tip data than the pressure spectra from the two-dimensional separation tests. It is also seen that in general the predicted noise using the expression of **George and Chou (1984)** is higher than what is predicted by **Brooks and Marcolini (1984).**

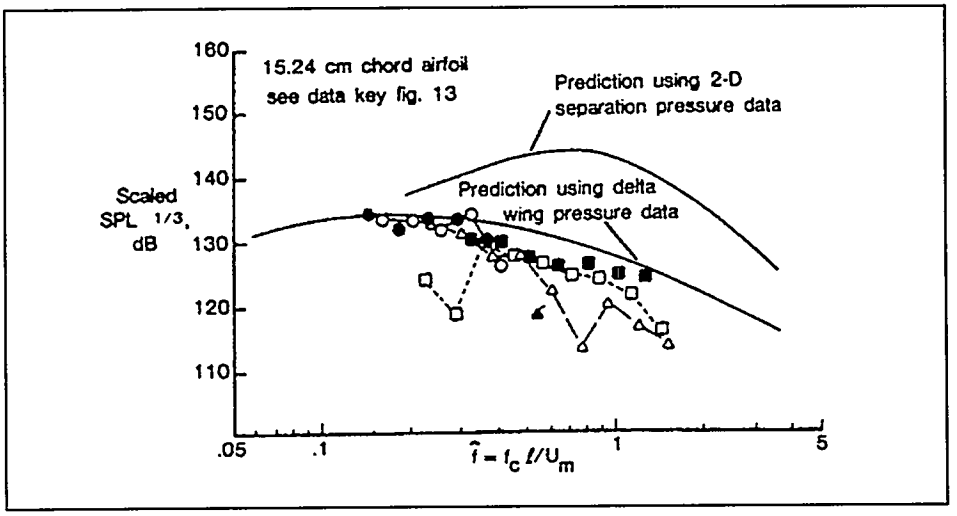

Figure 3-13 *The data of **Brooks and Marcolini (1986)** nondimensionalized and compared with the model of **George and Chou (1984).***

Finally, the importance of laminar boundary layer vortex shedding noise (LBL-VS) should be mentioned. LBL-VS noise occurs when the boundary layer over a considerable part of the airfoil is laminar and vortex shedding can develop when laminar boundary layer separation is interacting with the trailing edge. ***Brooks and Marcolini (1986)*** used tripped boundary layers to avoid this phenomenon. However, they also showed an example of how dominating LBL-VS can be, Figure 3-14.

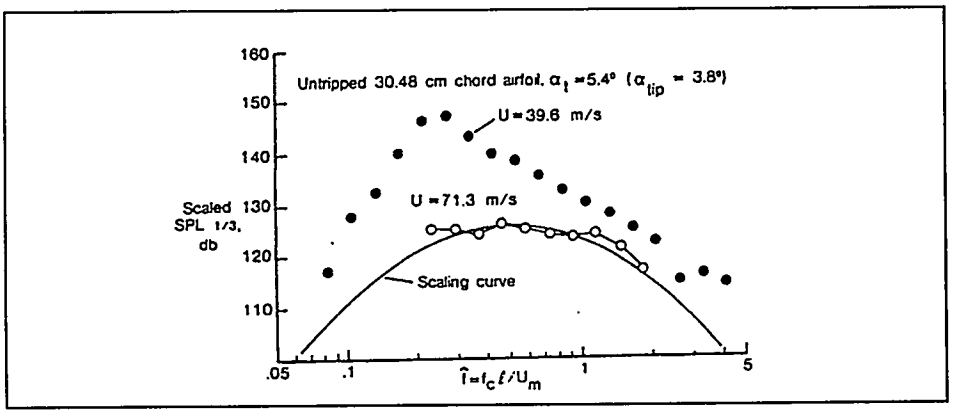

Figure 3-14 *Normalized tip noise spectra for untripped boundary layer and compared with scaling curve for the tripped cases, **Brooks and Marcolini (1986).***

The tip noise for two tunnel wind speeds are shown and the case with the lowest speed equal to 39.6 m/s shows much higher noise due to LBL-VS. The Reynolds number (Re.) is an important parameter for LBL-VS which increases for decreasing Re..This was examined by **Brooks and Marcolini (1985)** for trailing edge noise. The overall sound pressure level as function of Re. is shown in Figure 3-15 and up to Re. equal to 0.8 to 1.0 mill. the phenomenon seems to dominate the noise. However, the Re. is not the only parameter which determines the importance of LBL-VS. Also the free stream turbulence and angle of attack has considerable influence on LBL-VS as the location of the boundary layer transition position depends on these parameters.

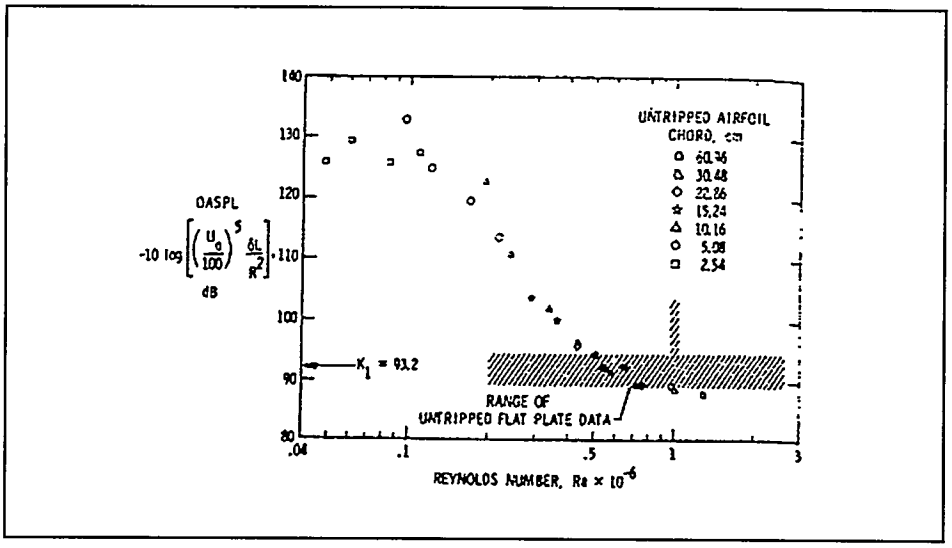

Figure 3-15 *Effects of Reynolds number of normalized overall trailing edge noise pressure level for untripped airfoils,* ***Brooks and Marcolini (1985).***

3.3 Other tip noise models

Lowson (1994) discusses another group of tip noise models which are fundamentally different from the two models described above. The model description is originally due to **Hardin (1980)** and contrary to the earlier mentioned models, where the noise is thought to be generated at the trailing edge, the main noise generation mechanism is proposed to be the sweeping of the wing vorticity field around the outer edge of the tip. A sketch of this is shown in Figure 3-16.

However, **Lowson (1994)** argues that eddies will only pass around the tip edge at low angles of attack, whereas at higher angles of attack separation will occur with large scale eddy activity. These large scale eddies were the main source of noise generation in the above models of **George and Chou (1984)** and **Brooks and Marcolini (1986)** but where they assume interaction with the trailing edge **Lowson (1994)** proposes that the noise generation takes place at the outer edge of the tip. In this way it is a combination of the two basic model types. This type of models will not be further considered in the present report but it seems likely that noise generation will occur both at the trailing edge of the tip and at the outer edge of the tip.

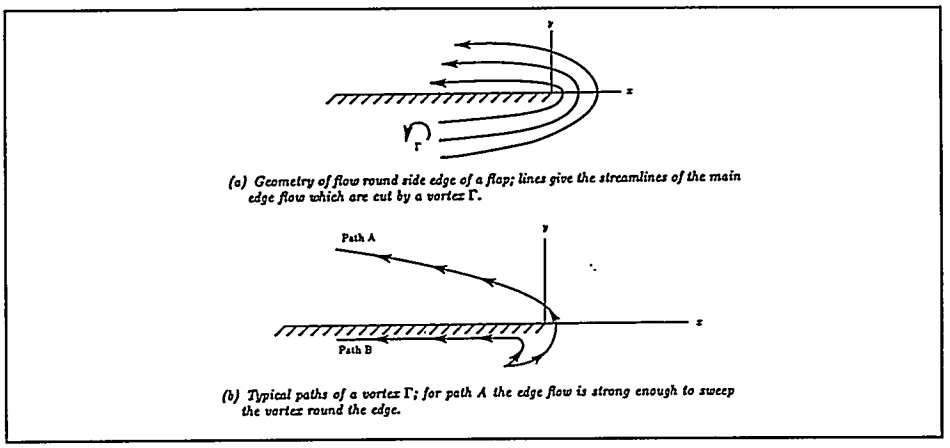

Figure 3-16 *The basic noise generation mechanism in the model of* ***Hardin (1980)*** *is the sweeping of vorticity around the outer tip edge.*

4. Numerical calculation

This chapter contains a brief description of the background for the numerical calculations on three different tip shapes. First the involved tip shapes are shown. Next, the governing equations are presented, the mesh generation and the applied boundary conditions are explained. Finally the numerical solution of the equations is briefly mentioned.

The numerical calculations are carried out with the commercial code, FIDAP. Concerning the turbulence modeling and the mesh generation, the choice of problem setup has in some ways been determined by the possibilities in FIDAP version 7.5, **FIDAP documentation (1993-1995)**.

4.1 Problem delimitation.

It was chosen to limit the numerical investigation to three fundamentally different tip shapes, shown in Figure 4-1. The tip shapes were chosen, so that they in principle cover most of the tip shapes in Figure 2-1, including the standard tip. The shapes of the tapered tips correspond to tip shapes used by **Antoniou et al. (1993, 1994)**. Here, power and overall noise measurements were carried out for a number of different tip shapes on a wind turbine operating in natural conditions.

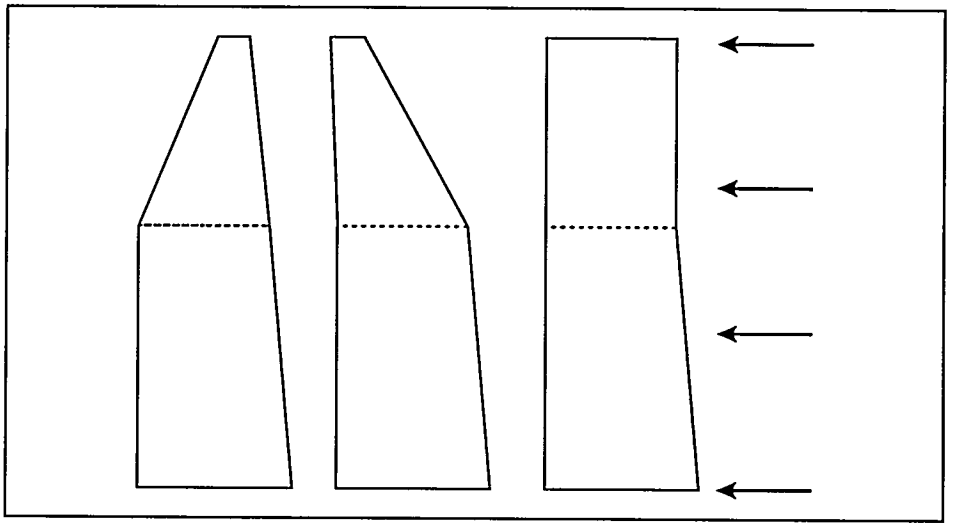

Figure 4-1. *The different investigated tip shapes. To the left, the tapered tip, in the middle, the swept, tapered tip and to the right, the rectangular tip. The flow direction is from right to left.*

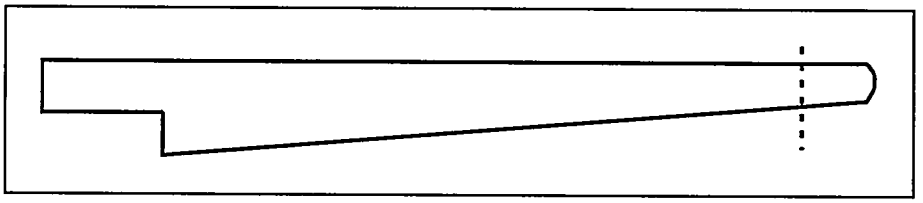

Figure 4-2 *Sketch of the blade used for measurements in Antoniou et al. (1993, 1994). The tip intersection (dotted line in Figure 4-1) is shown for comparison.*

- The tapered tip is shown to the left in Figure 4-1. The chordwise position of the airfoil aerodynamic center is constant and the tip chord is reduced to 25% of the tip intersection chord (dotted line), which primarily involves a forward displacement of the airfoil trailing edge towards the tip, whereas the leading edge is slightly moved backward relative to the oncoming flow.

- The swept, tapered tip is shown in the middle of Figure 4-1. The trailing edge is almost straight out to the tip and the decrease in chord length to 25 % at the tip gives an leading edge line which is bend towards the trailing edge.

- The rectangular tip is shown to the right in Figure 4-1. The chord and relative thickness are kept constant from the tip section chord towards the tip.

To investigate both attached and separated flow, calculations are performed at angles of attack of 5^0, 10^0 and 17^0 . The Reynolds number was in all calculations, Re. = $2 \cdot 10^6$.

The flow modeling is limited to the tip section region at the outer part of the blade as shown in Figure 4-2. Calculations are performed in a non rotating frame of reference. Therefore, centrifugal and coriolis effects from rotation are neglected. It is furthermore assumed, that the flow is fully turbulent on the entire blade.

4.2 Governing equations

It is chosen to solve the pressure velocity formulation of the Reynolds averaged Navier-Stokes equations for fluid motion. It is assumed that the fluid is incompressible, isothermal and nonexpanding. Furthermore only the steady state flow situation is considered. The governing equations shown in this section have been reduced according to these assumptions.

Adequate turbulence modeling is important for accurate computations of separated flows. Flow phenomena such as transition from laminar to turbulent flow and large scale flow separation are major challenges that have not yet been accurately modeled. A considerable research is ongoing within this field and a status on the present stage of turbulence modeling can be found in **Ekaterinaris et al. (1994)**. In the present study, the flow turbulence is described by the eddy-viscosity renormalization group (RNG) k-ε model by **Yakhot et al. (1992)**, developed for high Reynolds number flows. This model is one of the recently implemented turbulence models in FIDAP. It is well known, that the standard k-ε model is inadequate for prediction of separation and, that especially airfoil drag is determined with some uncertainty. Drag is of minor importance to this study and the RNG k-ε model should be better suited for predicting separated flow than the standard k-ε model, **FIDAP documentation (1993-1995)**.

The steady state governing Reynolds averaged Navier-Stokes equations of motion and the continuity equation can then be written:

$$\rho_0 u_j u_{i,j} = -p_{,i} + \rho_0 f_i + \left[\mu\left(u_{i,j} + u_{j,i}\right) - \rho_0 \overline{u_i u_j}\right]_j \qquad (4\text{-}1)$$

$$u_{j,j} = 0$$

(4-2)

where u_j denotes the 3 velocity components, p is the pressure, ρ_0 is the constant density and f is the body force vector.

To simplify notation, the overbar symbol, that denotes an average or mean value, was removed from terms that do not involve fluctuating quantities, but retained for the last term in equation (4-1) that involves correlation between fluctuating quantities. This term, $-\rho_0 \overline{u_i u_j}$, is often referred to as the Reynolds stress tensor. Even though it results from the convective terms, it is often grouped together with the laminar viscosity. It expresses the turbulent flux of the x_i-component of momentum in the x_j-direction or the x_j-component of momentum in the x_i-direction, since it is a symmetric tensor.

The introduction of the Reynolds stress tensor involves the turbulent closure problem, since it should be approximated to make the number of unknowns equal to the number of equations. This can be done by the Boussinesq approximation based on the so called eddy viscosity/ diffusivity concept:

$$-\rho_0 \overline{u_i u_j} = \mu_t \left(u_{i,j} + u_{j,i} \right)$$

(4-3)

where μ_t is the turbulent viscosity.

In the standard k-ε turbulence model, μ_t is computed from:

$$\mu_t = \rho_0 c_\mu \frac{k^2}{\varepsilon}$$

(4-4)

where k is the turbulent kinetic energy, $k = \frac{1}{2} \overline{u_i u_i}$, ε is the viscous rate of turbulent kinetic energy, $\varepsilon = \nu \overline{u_{i,j} u_{i,j}}$, ν is the kinematic viscosity and c_μ is an empirical constant.

Transport equations for k and ε can be obtained from the Navier-Stokes equations by a sequence of algebraic manipulations:

$$\rho_0 u_j k_{,j} = \left(\mu_0 + \frac{\mu_t}{\sigma_k} k_{,j} \right)_{,j} + \mu_t 2\varepsilon_{ij}\varepsilon_{ij} - \rho_0 \varepsilon$$

(4-5)

$$\rho_0 u_j \varepsilon_{,j} = \left(\mu_0 + \frac{\mu_t}{\sigma_\varepsilon} \varepsilon_{,j} \right)_{,j} + c_1 \frac{\varepsilon}{k} \mu_t 2\varepsilon_{ij}\varepsilon_{ij} - \rho_0 c_2 \frac{\varepsilon^2}{k}$$

(4-6)

where c_1, c_2, σ_k and σ_ε are empirical constants.

The RNG *k*-ε model is due to **Yakhot et al. (1992)**. It is based on their renormalization group approach. Compared to the standard k-ε model it employs an additional source/sink term in the ε transport equation (4-6) and employs different values for the various model coefficients. The transport equation for ε is modified to:

$$\rho_0 u_j \varepsilon_{,j} = \left(\mu_0 + \frac{\mu_t}{\sigma_\varepsilon} \varepsilon_{,j} \right)_{,j} + c_1 \frac{\varepsilon}{k} \mu_t 2\varepsilon_{ij}\varepsilon_{ij} - \frac{c_\mu \eta^3 \left(1 - \frac{\eta}{\eta_0} \right) \varepsilon^2}{1 + \beta \eta^3} \frac{\varepsilon^2}{k} - \rho_0 c_2 \frac{\varepsilon^2}{k}$$

(4-7)

where η is the ratio between characteristic time scales of turbulence and the mean flow fields:

$$\eta = s \frac{k}{\varepsilon},$$
$$s = \sqrt{2 s_{ij} s_{ij}}$$

(4-8)

s_{ij} is the strain rate tensor.

We hereby have a total set of six equations for the corresponding unknowns: the 3 velocity components in u_j, the pressure, p, the turbulent kinetic energy, k, and the viscous rate of turbulent energy, ε in the equations (4-1), (4-2), (4-5) and (4-8).

In FIDAP version 7.5 the empirical constants, including the Von Karman constant, κ, are defined as in Table 4-1.

Table 4-1 FIDAP 7.5 RNG k-e turbulence modeling empirical constants.

c_μ	σ_k	σ_ε	c_1	c_2	κ
0.085	0.7179	0.7179	1.42	1.68	0.3875

β and η are directly obtainable from the other constants.

4.3 Mesh generation

The mesh generation is an important part of the numerical solution of a flow problem since the solution reliability to a large extent relies on the quality of the mesh. In the present case, the mesh has resulted as a compromise from the following considerations:

- The number of elements should be restricted in order to limit the total calculation time.
- The modeling of the tip should be as close as possible to the shape of the real tip.
- Near the blade surface, the mesh density should be large to ensure a sufficient resolution of the viscous boundary layer.
- Near the blade surface, the elements should be orthogonal to the surface to minimize numerical diffusion and to enhance the rate of convergence.
- The mesh should be constructed in a flexible way, so that the shape of the tip is changeable with a minimum of effort.

To limit the total calculation time, the fluid domain is limited to the tip region. In the modeling of the different tips, it is chosen to apply the correct airfoil section and a variable chord and relative thickness along the span, whereas the twist is kept constant since this is almost the case in the tip region for the modeled blade.

The calculation domain is sketched in Figure 4-3, with the calculation domain bounded by 4 external faces. Taking the chord in the tip intersection as reference, the blade is being intersected by the bottom face 2 chord lengths from the tip intersection. Since the tip itself is 1.5 chord lengths, the total span is 3.5 chord lengths. The fluid region is extended on top of the tip until 7 chord lengths above the bottom face leaving a distance of 3.5 chord lengths for capturing the tip vortex.

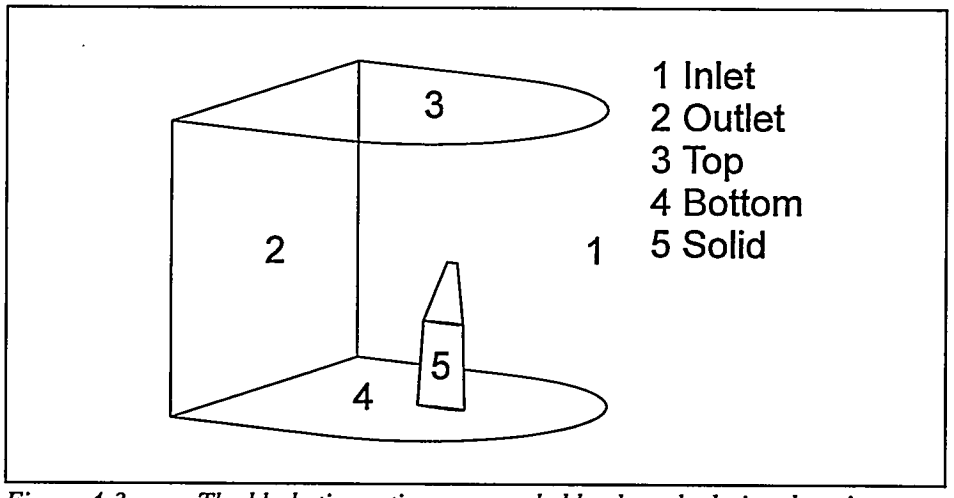

Figure 4-3. The blade tip section surrounded by the calculation domain.

In a plane perpendicular to the spanwise direction, the domain is extended 4 chord lengths to the inlet and 3 chord lengths to the outlet. It is assumed that a mesh of this size is sufficient for a relative comparison between the different tip shapes. However, the far field influence on the tip flow from the external boundaries was not investigated.

The variation of the tip geometry in the spanwise direction introduces some difficulty. One way to generate the final mesh is to generate a mesh covering half of the bottom face intersected by the airfoil section chord line. This mesh is then drawn along the blade span, continued around the blade tip and finally ended on the other half of the bottom face. This has caused some problems with an unstructured mesh. Instead, a C-type mesh is located perpendicular to the spanwise direction. This is then extended in the spanwise direction from the bottom face to the top face. The elements within the blade is modeled as solid wall elements.

The application of unstructured meshes is one of the significant advantages of the finite element formulation and attractive, since it saves elements but allows for high mesh density in important areas. FIDAP has this feature, even though it is somewhat restricted in three dimensions. The mesh can be fully unstructured in two dimensions, whereas it has to be structured in the third direction. The uniformity of the C-mesh is well suited for the use of an unstructured mesh. The mesh is then structured in the spanwise direction. However, the application of the unstructured mesh is impossible near the blade surface because the blade geometry changes along the span and the near wall boundary region elements can not be sufficiently orthogonal.

To overcome this problem, the solution domain has been divided into an inner and an outer region as shown in Figure 4-4, where the bottom plane of the calculation domain is showed. The inner region contains a structured mesh, that is dense near the surface and gradually becomes coarser away from the surface. Behind the airfoil trailing edge, the inner region is extended to obtain a better resolution in the airfoil wake. Even though the mesh near the surface is structured, it is difficult to maintain a good mesh quality along the entire span when the trailing edge and the leading edge of the airfoil is displaced. The mesh will therefore always be a compromise on the orthogonality.

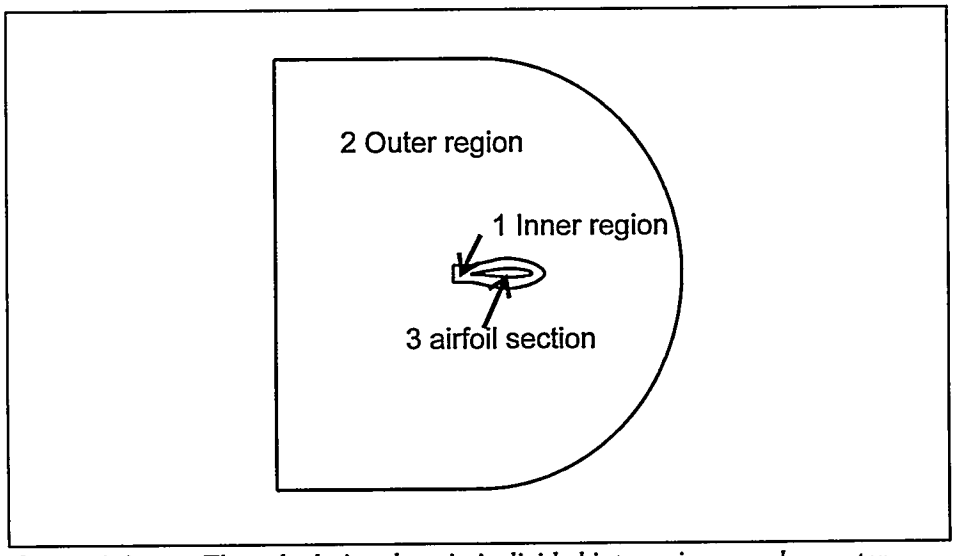

Figure 4-4 *The calculation domain is divided into an inner and an outer region as shown in the bottom plane.*

The outer region contains an unstructured mesh, where the transition from the dense inner mesh to very coarse boundary elements takes place. In this way, the number of elements in each spanwise mesh block can be reduced to 5200 elements. Since the border between the inner and the outer region is constant along the blade span, the unstructured mesh is simply extruded along this.

The use of both an inner and an outer region saves elements and ensures a dense mesh near the blade surface. However to improve the orthogonality of the mesh at the blade surface, the inner region is furthermore divided into 4 blocks besides the airfoil block and the outer region, a total of 6 blocks, Figure 4-5. Because of the change of the blade along the span and the free tip, the spanwise direction is divided into 3 blocks, Figure 4-6. In total, the calculation domain contains 18 blocks. The division in blocks has furthermore the advantage, that when the tip geometry is changed, only the blocks around and on top of the tip have to be regenerated.

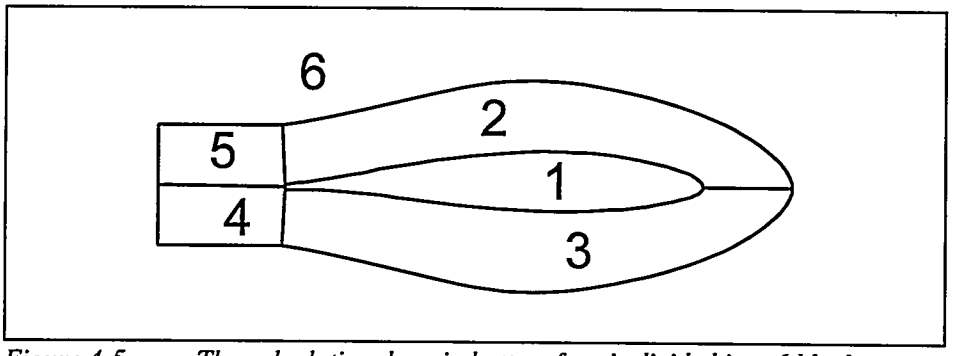

Figure 4-5 *The calculation domain bottom face is divided into 6 blocks.*

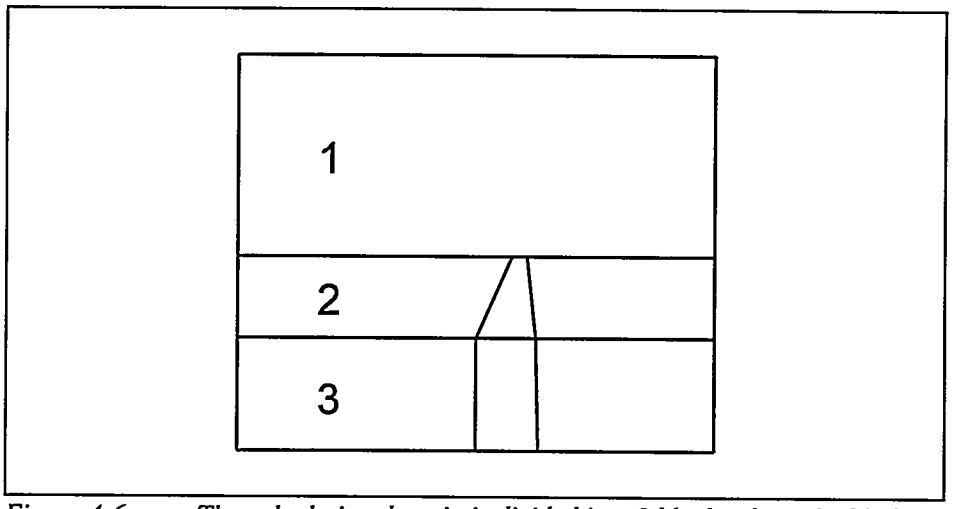

Figure 4-6 *The calculation domain is divided into 3 blocks along the blade span.*

In Figure 4-7 and Figure 4-8, the generated mesh for the tapered tip is shown in both the inner and the outer region. Figure 4-7 gives an overall impression of the outer region with the grading along the blade span to gain maximum density at the free tip, Figure 4-8. All in all, the mesh has a total of approximately 78000 elements with around 73000 nodes.

Figure 4-8 shows the meshing of the inner region near the airfoil surface and the bottom of the tip section. The reason for the dense mesh in the entire region is to take into account the change in geometry, that takes place along the span as the tip is encountered, since the solid region decreases.

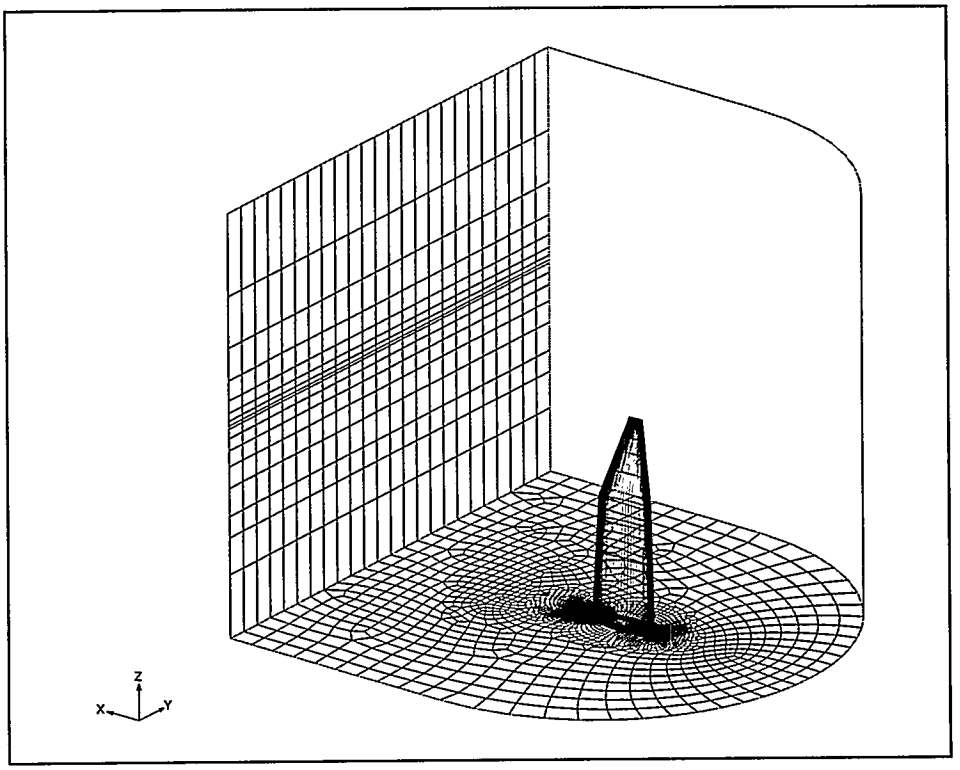

Figure 4-7 *The generated mesh in the outer region of the domain for the tapered tip.*

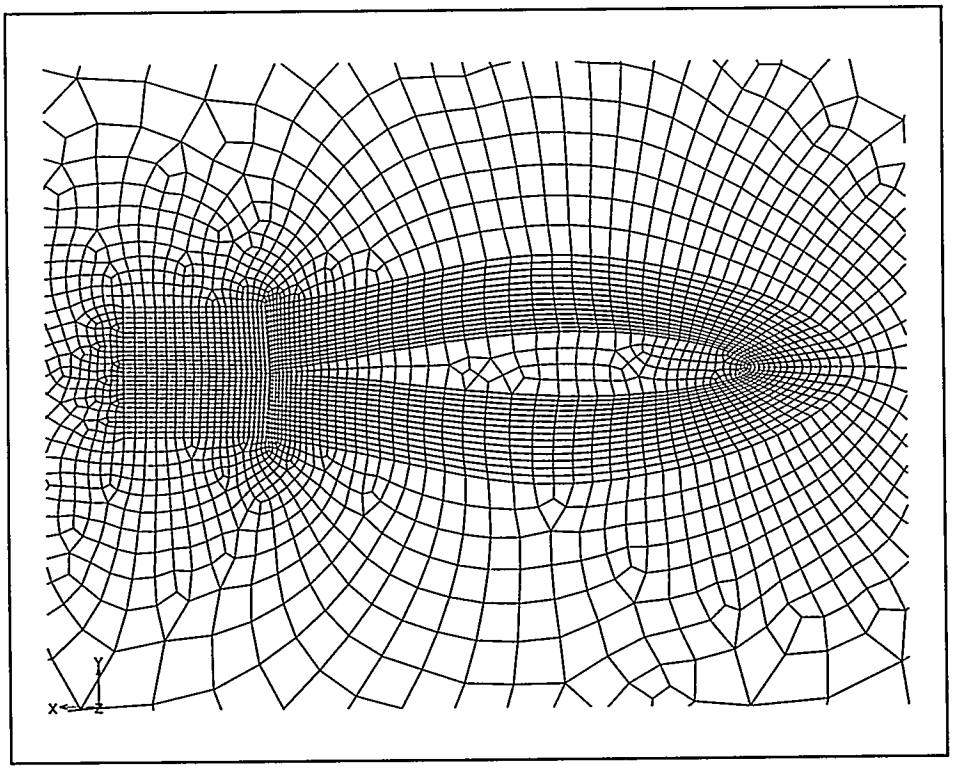

Figure 4-8 *The generated structured mesh in the inner region for the tapered tip.*

4.4 Boundary conditions

In Figure 4-2 the calculation domain was shown. The explicit boundary conditions for the different solution variables on the mesh boundaries are given in this section. The pressure is treated implicit and does not require any boundary conditions.

The inlet face (1) and the top face (3) are traditional Dirichlet boundaries. The velocity together with k and ε are prescribed. The vertical velocity component is set to zero, whereas the remaining components are set to the actual airfoil angle of attack. k is set to 0.03, whereas ε is set to 0.032.

The outlet face (2) is a Neumann boundary. The derivatives of both the velocity, k and ε are set to zero.

At the bottom face (4), it is assumed that the flow is 2-dimensional and the spanwise (vertical) flow component is neglected, whereas the remaining velocity components satisfy a Neumann boundary condition..

At the solid tip section (5), the fluid elements are special elements that follows the law of the wall for turbulent flow.

4.5 Flow equation solver

In FIDAP, the governing equations are discretized by the finite element method. The application of the finite element method discretization on the continuos flow problem results in a nonlinear system of matrix equations. Since the number of equations is high, a full coupled solution of the flow problem would require to much physical storage. Therefore, the different flow equations are solved iteratively in a sequential manner by a segregated algorithm.

5. Numerical results

This chapter contains results from the numerical calculations on the three different tip shapes shown in Figure 4-1. To cover both attached and separated flow, calculations are performed for angles of attack of 5, 10 and 17 deg respectively. The Reynolds number is in all cases, Re. = $2x10^6$. First the general flow picture is described with pressure distributions and particle traces. Next the tip vortices are studied. The flow separation lines are found and the tip loading is calculated. Finally, the two aerodynamic parameters required for computation of the aeroacoustics, as described in Chapter 3, are compared with the empirical data. For practical reasons, figures of the numerical results are placed in Appendix A.

5.1 General flow picture

Presenting the overall flow picture of a complex 3-dimensional flow problem is not an easy task. In the study, use of intersecting planes and the release of mass-less particles in the flow field together with the use of colors have been utilized. The primary focus is directed towards the boundary layer flow together with the near flow field in the wake downstream from the tip region, whereas the oncoming flow and the outer flow regions are of minor importance.

To limit the extent of the chapter, primary attention is in some cases given to the rectangular tip for an angle of attack of 10 deg and the results from the other tips are then compared to this.

Figure A-1 and Figure A-2 show velocity vectors in two different intersection planes for the rectangular tip at an angle of attack of 10 deg. In Figure A-1, the plane is intersecting the blade at the blade tip section perpendicular to the spanwise direction. It appears that the flow on the airfoil suction (upper) side becomes detached at approximately 30% chord and a zone of separated recirculating flow is located above the remaining part of the suction side. The vorticity within this zone is then convected downstream in the airfoil wake.

Judging from Figure A-1 alone the flow reminds of ordinary 2-dimensional flow. However, the formation of the tip vortex at the free blade tip, and the trailing vorticity from changes in the blade loading leads to rotation downstream from the blade trailing edge. Furthermore low momentum fluid from the separated flow region also tends to develop spanwise flow components which is reflected in Figure A-2. Figure A-2 shows the velocity vectors in a plane perpendicular to the main flow direction just downstream of the trailing edge. The blade suction side appears to the right. The bottom of the figure roughly corresponds to the tip section. The ending of the blade is marked with lines and the in-plane velocity components originating mainly from the tip vortex, is revealed. It appears that a single strong vortex exists. The direction of rotation corresponds to the flow coming from the pressure side onto the suction side. Despite the tip vortex, smaller scale rotation from the low momentum fluid in the boundary layer exists further away from the tip.

The tapered tips do in general follow the same flow pattern. Because of the change in blade loading from the change in the chord away from the tip, the strength of the tip vortex is less compared to the rectangular tip, whereas the vorticity from the trailing edge is increased in the tapered region. This will be further discussed in the next section.

Pressure distributions

Figure A-3 to Figure A-8 contain contour plots of the pressure distribution for the different tips. In Figure A-3, the pressure distribution on the suction side is shown for the rectangular tip at an angle of attack of 10 deg. It can be seen, that the pressure minimum (suction peak) appears close to the airfoil leading edge. Afterwards, the pressure is recovered along the airfoil chord. At the very local area around the tip, a strong 3-dimensional behavior from the tip flow motion is revealed, and the maximum pressure appears at the tip trailing edge. Further down from the tip, the spanwise variation of the pressure appears to be very small. However the induction from the tip vortex has some effect on the blade loading and hence the pressure distribution. Figure A-4 shows the corresponding pressure distribution on the pressure side. Since the magnitude of the pressure is different from the suction side, the color range is adjusted for maximum resolution. In general the pressure variation is smaller on the pressure side. The local 3-dimensional behavior at the tip is found again.

Figure A-5 and Figure A-6 show the pressure distribution on the suction side for the tapered and the swept, tapered tip, respectively at 10 deg angle of attack. The pressure distribution for the tapered tip in Figure A-5 shows a change when the tip section starts. On the mid span of the tip section, the pressure remains almost 2-dimensional when the tapering is taken into account. This could be because the streamwise induced flow components from each of the shed vortices from the trailing edge is eliminated because the strengths of the vortices are almost equal due to a constant slope on the bound circulation from the linear reduction in chord. This will be further examined in section 5.4. On the far outer tip region, the 3-dimensional effects are dominating the flow.

The swept, tapered tip in Figure A-6 shows a similar flow picture despite that, the contours of the pressure are swept back with the quarter chord line. The trailing edge of the tip has an increased pressure compared to the tapered tip.

The flow pictures at an angle of attack of 5 deg are similar to the above mentioned. At 17 deg angle of attack, massive separation tend to dominate the flows. The suction side pressure distributions for the rectangular tip and the tapered tip are shown in Figure A-7 and Figure A-8 respectively. The suction side pressure distribution for the swept, tapered tip is not shown, since it shows only little variation indicating that the entire suction side flow is separated. The pressure distribution for the rectangular tip in Figure A-7 apparently has an area of low pressure just below the outer tip region. This is probably because the tip vortex induction declines the effective angle of attack in the tip region. A secondary area of low pressure is located at the trailing edge approximately one chord from the tip. This secondary area could be due to the tip vortex, but could also origin from interaction from stall bubbles leading to spanwise changes in the extent of the separation. For the tapered tip Figure A-8 shows the same both at the tip and before the tapered section.

Particle traces

All in all, the shown pressure distributions have given information about the gross flow effects and the overall influence on the pressure from the tip vortex. However to gain detailed information about the formation of the tip vortex and the extent of attached and detached flow regions, a number of particle traces was calculated. The particles are injected at different spanwise locations in the flow in the outer part of the boundary layer along the chord line, mainly on the suction side. They

are mass less and are therefore simply convected with the local fluid motion. The color code for the particles corresponds to the starting chordwise location.

Figure A-9 concerns the rectangular tip at an angle of attack on 10 deg. Particles are introduced along the pressure and suction side at the end of the span and furthermore on the leading edge at three different spanwise locations. The particles at the end of the span clearly reveal the formation of the tip vortex. The flow convects from the pressure side to the suction side as the airfoil chord line is passed and the flow rotation continues in the wake region. It appears, that the formation of the tip vortex is a local phenomenon and the tip vortex itself is quite concentrated. This corresponds well with the shown pressure distributions. The particles released further down the span appear to be almost unaffected by the tip vortex.

To investigate the tip vortex formation together with the general flow picture, Figure A-10 to Figure A-16 contain particle traces from the different tips, where particles are introduced on the suction side along the entire span.

Figure A-10, Figure A-11 and Figure A-12 concern the rectangular tip at the angles of attack, 5, 10 and 17 deg, respectively. At 5 deg (Figure A-10), the flow appears to be smooth along the chord with only very little separation a chord distance from the tip. The tip vortex formation affects only the far upper part of the span. It appears though, that the flow below the tip vortex is slightly displaced downwards on the upper half of the tip section. At 10 deg (Figure A-11), the tip vortex has become stronger, since the rotational flow components have increased. However the tip vortex spanwise extension is nearly unchanged. The tip vortex reduces the extent of separation just below the tip. Further down, the flow is separated approximately from the mid span. This loss of momentum causes the downward displacement to increase, so that the flow below the tip is displaced around half a chord distance inward. The general flow picture at 17 deg (Figure A-12) is very different from the lower angles of attack and tends to be dominated by massive separation despite the region just below the tip vortex. This region corresponds well with the low pressure area found in Figure A-7. The rotation in the tip vortex has increased and flow from below the far outer tip region appears to be rolled up into the tip vortex some distance downstream from the trailing edge. This has probably prevented the previously shown downward flow component. Furthermore a huge stall bubble affects the flow on the mid span. Obviously, the flow is highly instationary.

Figure A-13 and Figure A-14 show particle traces for the tapered tip at 5 and 10 deg respectively. The flow at 5 deg in Figure A-13 shows a weaker tip vortex compared to the rectangular tip (Figure A-10). This is because of the gradual reduction in the bound vorticity from the tapering. Trailing edge vorticity is shed from the tip along the tapered region. This can however not be seen on the particle motion in the wake. It appears that flow is streaming around the trailing edge from the pressure side onto the suction side and apparently this amplifies the downward displacement of the flow below the tip vortex. Below the tapered region, the flow is only slightly affected by this additional vorticity. Figure A-14 shows the flow picture at 10 deg. Compared to Figure A-13, the tip vortex strength is increased. However the main difference is the increased downward fluid flow at the trailing edge. This now influences almost the entire tip region. This tendency is also present for the flow picture at 17 deg (not shown).

Figure A-15 and Figure A-16 concern the swept, tapered tip at 5 and 10 deg. In contrast to the other tips, it appears that the tapered part of the tip region for the

swept, tapered tip has upward displacement of the flow from the mid chord untill the trailing edge. Figure A-15 shows the flow at 5 deg. In general, the particle traces show almost attached flow except for the tapered region where separation is initiating. Because of the upward flow motion, fluid from below the tip is enclosed into the tip vortex downstream of the trailing edge. At 10 deg (Figure A-16), the flow upward displacement is increased at the tapered part of the span. Below, the flow is displaced downwards. It is not possible to judge, whether the tip vortex is stronger than for the tapered tip, however more fluid seems to be included. Further down the span the upward displacement is replaced by downward fluid motion from the trailing edge. It appears that the flow is more separated than the other tip flows at 10 deg (Figure A-11 and Figure A-14). This tendency is again found at 17 deg (not shown).

All in all, this section has shown both the gross flow effects and the near field flow downstream of the trailing edge for the different tips. Main results are in summary:

- The tip vortex strength was verified to be lower for the tapered tips.
- The general flow picture concerning the tip vortex formation in the wake is similar for the three tips. In contrast, the near flow field downstream of the trailing edge is different.
- The fluid at the trailing edge is displaced either upward or downward. This is believed to depend on the sweep of the trailing edge, since the swept, tapered tip, that is swept backward, showed upward fluid motion, whereas the other tips showed downward fluid motion.
- The suction side pressure distributions and the particle traces at high incidence indicate separation over the entire suction side for the swept, tapered tip. The tapered tip and the rectangular tip show areas of attached flow. These differences are apparent though the tapered tips would show equal behavior in lifting line calculations.

5.2 Tip vortex flow

In the previous section, the formation of the tip vortex was shown as well as the trailing edge wake flow by use of particles. These, however gave only an overall impression of the flow picture. This section is a further investigation of the tip vortex from the trailing edge and downstream in the wake. To show the vortex properly one has to separate the rotation in the vortex from the main flow. This can only partially be done by calculating either the vorticity or the velocity components in a plane perpendicular to the main flow direction. It is instead chosen to calculate the local helicity.

Taking a volume of a closed surface, the local helicity, H, is calculated as **Kida (1994)**:

$$H = \int_V \vec{u} \cdot \vec{\omega} \cdot dV \qquad (5\text{-}1)$$

Where $\vec{u}$ is the velocity vector and $\vec{\omega}$ is the vorticity vector.

In the following, the helicity is referred to as the integration body, $\vec{u} \cdot \vec{\omega}$. Calculating this will reveal vorticity mainly in the wake where both the velocity and the vorticity is high which are the two terms in the product forming the helicity. In the boundary, the vorticity is large, while the velocities are small and in

the undisturbed flow, the vorticity is low, while the velocity is large. In both cases the helicity will in general be lower than in the wake with vorticity. The helicity has furthermore the advantage, that the direction of motion is captured in the sign.

In Figure A-17 the helicity for the rectangular tip at an angle of attack of 10 deg is shown in a plane perpendicular to the flow direction 0.5 chord length downstream of the trailing edge. The plot contains the upper part of the tip section only. The tip vortex is seen just below the tip. An additional counter rotating secondary vortex appears further away from the suction side. Below the tip vortex, boundary layer vorticity appears. This is convected downstream from the trailing edge.

To show the development of the tip vortex downstream of the trailing edge, the helicity was calculated in several planes at different locations in the wake, all perpendicular to the main flow direction as in Figure A-17. Areas with low helicity are filtered away. The planes are the chord mean line, the trailing edge, planes with a distance of 0.5 chord until 2 chords downstream and then planes with a distance of 1 chord. To prevent the perspective view to distort the location of the tip vortex, two particles are released from the tip trailing edge. These are then located in the vortex core downstream throughout the wake.

Figure A-18, Figure A-19 and Figure A-20 concern the rectangular tip at 5, 10 and 17 deg respectively. At 5 deg (Figure A-18) the boundary layer does not form a significant amount of helicity. As it was also shown in Figure A-17, the tip vortex appears together with a counter rotating secondary vortex further away from the suction side. The secondary vortex vanishes at around 1 - 1.5 chord length behind the trailing edge, while the tip vortex remains in the flow until the outlet of the calculation domain. In the beginning, the tip vortex vorticity is concentrated in an annular ring with a non rotating core. As the vorticity is convected downstream, the diffusion from viscosity and turbulence mixes the flow so that the rotation is equalized with the core and the extent for the vortex is slightly increased towards the outlet. The change of shape towards the outlet is also partially because of the coarsening of the mesh.

At 10 deg, Figure A-19, the overall vortex picture is the same as at 5 deg. The vortex strength and extent has grown corresponding to the increase in the bound circulation. Additionally boundary layer from separation at the suction side appears just after the trailing edge, but dies out shortly afterwards. The picture is almost the same at 17 deg (Figure A-20). However the flow field has become very complex because of the massive separation. Additional vortices with different directions of rotation are created in the boundary layer and convected downstream from the trailing edge in the wake. Still, they tend to die out before the tip vortex.

Figure A-21 and Figure A-22 contain the vortex picture at 10 deg for the tapered and the swept, tapered tip respectively. Compared to the rectangular tip in Figure A-19, the strength and the extent of the tip vortex is reduced as it could be expected. However whereas the rectangular tip had no significant trailing vorticity the tapered tips show a vortex sheet forming from the trailing edge. The vortex picture of the tapered tip in Figure A-21 shows a lengthy secondary vortex in connection with the trailing vorticity.It vanishes just after the trailing edge. The trailing edge vorticity remains in the wake until about 1 - 2 chord lengths downstream from the tip.

The swept, tapered tip is shown in Figure A-22. Because of the sweep back of the leading edge, the tip vortex will start to roll up already around the leading edge as the flow passes the airfoil, as it is known from delta wings. The delta wing tip

vortex hits the suction side and can affect the suction side pressure and form a small secondary vortex close to the leading edge. These are however small scale effects, and was not found in this case, both because of the coarse mesh and a relatively small sweep angle. The vortex picture does show a secondary vortex forming just next to the tip trailing edge, however it is very small and exists no longer than 0.5 chord length downstream. Again the trailing edge vorticity is seen. Here, it vanishes about 1 chord after the trailing edge. Taking into account that the tip vortex starts earlier for the swept, tapered tip because of the sweep back of the leading edge, the magnitude of the trailing edge vorticity is comparable with the tapered tip, but the formation of the secondary vortex is apparently prevented.

Figure A-23 to Figure A-26 contain contour plots of the helicity for the different tips at an angle of attack on 10 deg in planes that are aligned with the main flow direction. Figure A-23 shows the rectangular tip, Figure A-24 the tapered tip and Figure A-25 and Figure A-26 the swept, tapered tip. This is another way of showing the helicity in the wake, though it is only a snapshot in a single plane. Because of the curvature of the airfoil surface, the distance from the surface to the intersecting plane will not be constant along the chord and the view will somehow become distorted. However. The described tip vortex formations and the secondary vortices are again found. The development of the secondary vortex for the tapered tip is clearly seen (Figure A-24) and the early roll up of the tip vortex for the swept, tapered tip is shown in two different planes, where the plane in Figure A-26 is translated 0.05 chord length towards the pressure side compared to Figure A-25. Figure A-26 then shows the starting of the vortex, whereas Figure A-25 shows the continuing roll up.

Results from this section are in summary:

- The helicity is found suitable for revealing the vortex picture of a viscous wake flow.
- Downstream in the wake, the tip vortex rotation is equalized and the non rotating vortex core is swallowed by the vortex.
- At high angles of attack, a significant amount of vorticity from the boundary layer is convected downstream.
- For the rectangular tip and the tapered tip, a large secondary vortex is found next to the tip vortex further away from the suction side. This vortex is of less strength, but could affect the near field of the tip flow.
- The trailing edge vorticity seems to be stronger for the swept, tapered tip than for the tapered tip.
- Even though the tapered and the swept, tapered tip chord distribution is equal, the difference in the sweep of the leading and trailing edge appears to have a significant influence on the flow because of the different vortex roll up.

5.3 Flow separation

To further investigate the differences of the tip flows, separation lines were found for the flow on the suction side and these are commented in this section. The separation lines were determined by two different methods.

In Figure A-27, the viscous force from the wall acting on the fluid is shown for the suction side of the rectangular tip at 10 deg. The flow direction is from right to left. Close to the leading edge, the viscous force direction is opposite to the main flow direction indicating attached flow. At the mid chord, the viscous force is reduced substantially because of the weakening of the boundary layer from the adverse pressure gradient. Towards the trailing edge, the direction of the viscous force

vector is changed to have a horizontal component aligned with the flow direction and the flow is separated.

Figure A-28 shows mass less particles, that are released close to the surface, again for the rectangular tip at 10 deg. The particle traces behave like tufts, which are wool threads fastened to the surface with tape. The tufts align with the local boundary layer flow and hence reveal if separation and reversed flow appears. Furthermore they will show a possible spanwise flow component within the zone of separation.

Whereas the flow at 5 deg mainly is attached and hence of less interest, separation lines for the flow at 10 and 17 deg are shown for the different tips in Figure 5-1 and Figure 5-2. The chordwise position is measured from the trailing edge, meaning that 100% correspond to entirely separated flow. The spanwise position is given with reference to the chord at the tip root section. In this way, 0 corresponds to the start of the tapered part for the tapered tips (dotted line in Figure 4-1). The separation lines are not smooth because the separation points at different locations are connected with straight lines.

At 10 deg (Figure 5-1), separation at the inboard part of the blade starts at about 20 - 30 % for the different tips. 2-dimensional calculations on the airfoil section with the XFOIL code by **Drela (1987)** with forced transition on the leading edge resulted in about 25% and hence is in fair agreement. In general, the inboard section appears to be quite similar for the different tips, whereas the outboard section differs substantially. For the rectangular tip, the separation line remains at about 30% until approximately 2 chord lengths from the tip. After this, the separation point moves backward to 43% at the starting of the tip section. Then it is reduced towards the trailing edge in the tip region. The attached flow in the outer tip region is due to the tip vortex, that reduces the effective angle of attack.

The tapered tips show a similar pattern until around the starting of the tip section. The separation point is then moved further towards the leading edge. For the tapered tip, the separation point is moved towards the trailing edge just after the beginning of the tip section. This is due to the beginning of the tapered region, that results in a vortex from the change in the bound vorticity. The swept, tapered tip does however not show a movement towards the trailing edge after the starting of the tapered section. Approximately one chord from the tip, the tapered tip show a reduction in the separation whereas the swept, tapered tip becomes totally separated at the tip. Even though the two tapered tips have a similar chord distribution, the separation at the tip is very different. The tip vortex for the tapered tip is reduced compared to the rectangular tip, but still, it results in a reduction of the effective angle of attack. In contrast, the flow around the tip for the swept, tapered tip indicates that the effective angle of attack is not reduced correspondingly.

The separation lines at 17 deg are shown in Figure 5-2. Compared to 10 deg, massive separation now tends to dominate the flow. At the inboard section all tip flows separate at the leading edge. This is again in good agreement with XFOIL. For the rectangular tip, the tip vortex moves the separation point towards the trailing edge at the tip. The tapered tip shows a region just below the beginning of the tip section where the separation point is moved from 93% to 67% because of the beginning of the tip vortex. After this, the separation point increases to 81% towards the tip before the tip vortex finally reduces it to below 40%. The swept, tapered tip shows detached flow on the entire suction side at the entire span.

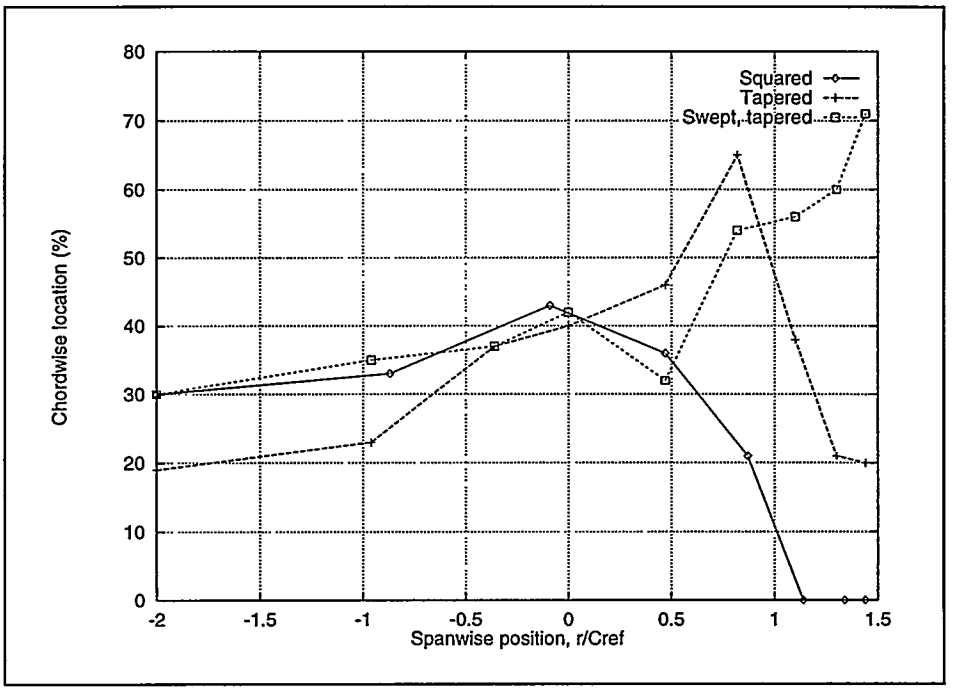

Figure 5-1 *Separation lines for the different tips at an angle of attack on 10 deg.*

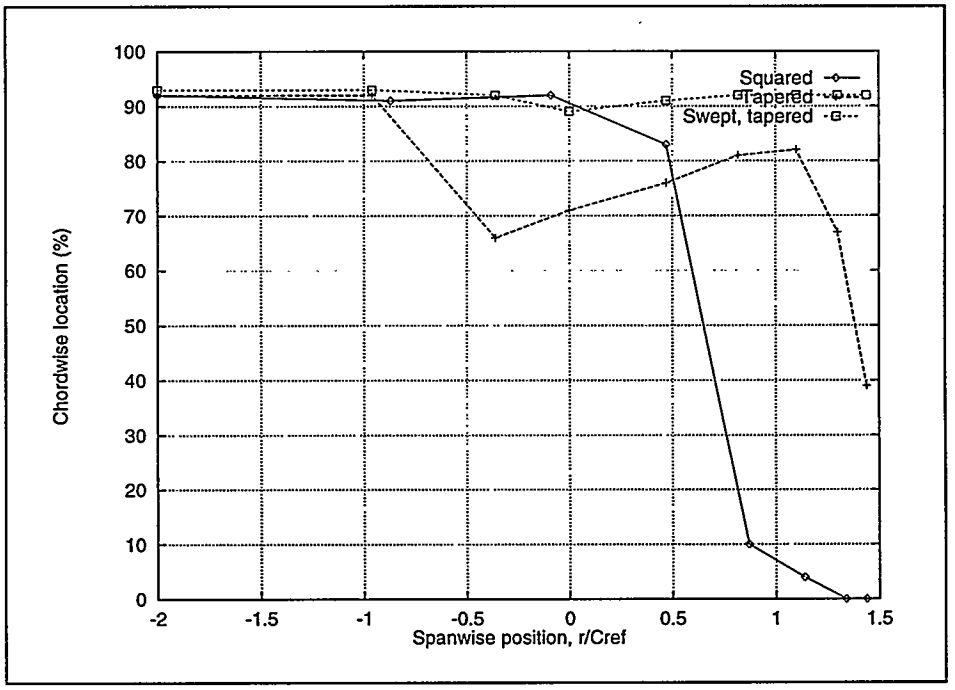

Figure 5-2 *Separation lines for the different tips at an angle of attack on 17 deg.*

The above considerations are in summary:

- The 3-dimensional behavior of the flow separation on the suction side was compared for the three tips. They show a similar behavior on the inboard section, whereas the outboard section is different.
- The effective angle of attack for the rectangular tip and the tapered tip is reduced at the tip. At the starting of the tip region, the tapered tip furthermore show an additional reduction in the extent of separation from trailing vorticity.
- The swept, tapered tip does not show any corresponding reduction in the effective angle of attack.

5.4 Spanwise loading

In this section, the influence on the spanwise loading from the revealed differences in the flow pictures for the different tips are investigated. Furthermore comparisons will be carried out with results from the lifting line calculation model mentioned in Chapter 2. The induced velocities at the lifting line are calculated from the shed vorticity in the wake. Both the wake near field and far field are taken into account. An eventual contribution from the bound circulation itself is neglected and hence the difference between the two tapered tips can not be resolved with the lifting line model.

The spanwise distribution of the circulation and the lift coefficient for the different tips at 5 deg is shown in Figure 5-3 and Figure 5-4. The tapered tips appear to behave similar, since there is good agreement on the outer part of the tip. The slope of the bound circulation is flatter than the rectangular tip, as it could be expected. For the rectangular tip, the slope is gradually becoming steeper towards the tip, whereas the slope for the tapered tip has a change at the tip root section, indicating the beginning of the tapered section. Apparently the swept, tapered tip does not show this. The lift distribution for the rectangular tip follows the circulation quite well with a reduction towards the tip from the decrease in the effective angle of attack.

The lifting line results are shown for comparison. In general the correlation between the two calculation methods is good. The CFD calculation underestimates the circulation, Figure 5-3, but the relative difference for the circulation appears to be the same throughout the span. The reason for the underestimation is probably, that the airfoil suction peak is insufficiently resolved and hence the lift coefficient underestimated as shown in Figure 5-4. Because of the limited calculation domain, the wake from the CFD calculation does not contain the far field. Inclusion of this would increase the induced velocities and therefore lower the circulation another few percent.

The lift coefficient for the outer part of the tapered tips is somewhat different for the two calculation methods. Both models show an increase in the lift coefficient. Whereas the CFD result is nearly constant, the lifting line model shows a larger increase in the lift towards the tip. The increase is partially because the strength of the shed vorticity from the tip is reduced. As it was explained in Chapter 2, this increases the effective angle of attack. Furthermore, the slope of the circulation towards the tip is nearly constant in a broad region. Taking some point on the lifting line in this constant area, the free stream component of the induced velocities in this point from two equally strong shed vortices on each side will cancel out. This is nearly not seen in the CFD calculation probably because of viscous effects.

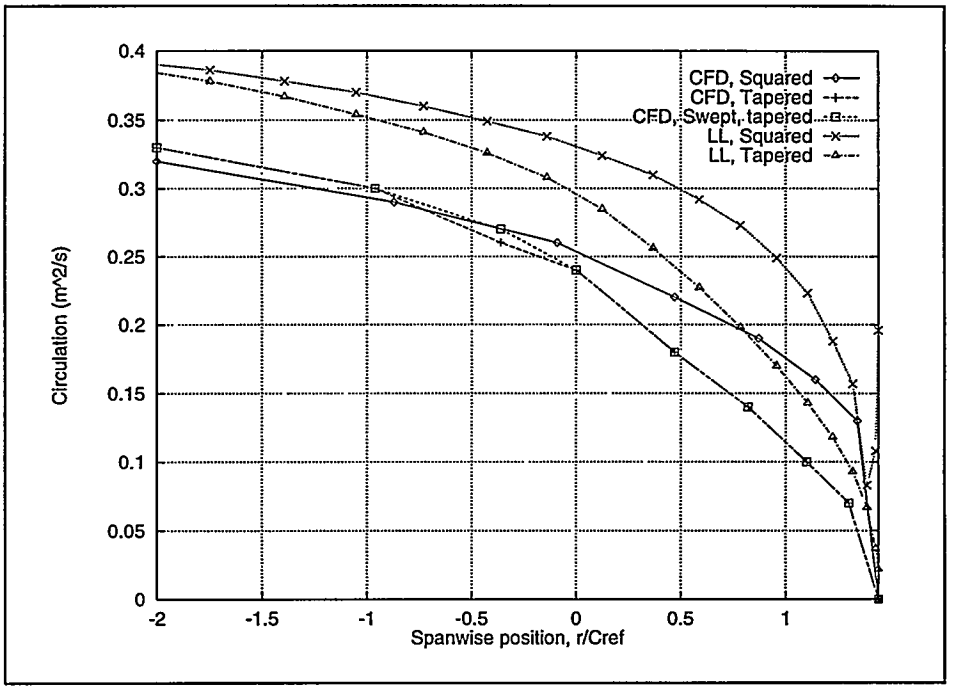

Figure 5-3 *Spanwise distribution of circulation from CFD and lifting line calculations for the different tips at an angle of attack on 5 deg.*

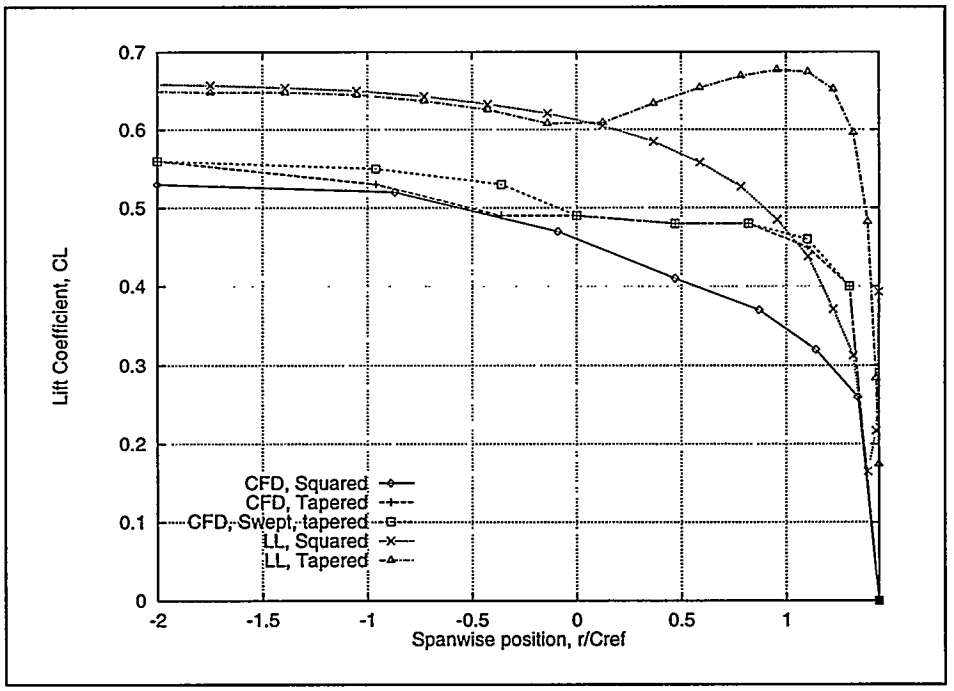

Figure 5-4 *Spanwise distribution of the lift coefficient from CFD and lifting line calculations for the different tips at an angle of attack on 5 deg.*

In Figure 5-5 and Figure 5-6 the spanwise circulation and the lift coefficient is shown for the angle of attack on 10 deg. In general the picture is somewhat the same as at 5 deg concerning the rectangular tip. The circulation for the tapered tips are however no longer the same. The difference in the root region is of less importance. More important is it, that the swept, tapered tip has lower circulation

in the tip region. This is apparently because of the difference in the lift coefficient towards the tip. The lifting line theory again shows an increase in the lift coefficient towards the tip for the tapered tip and again this is not seen in the CFD results.

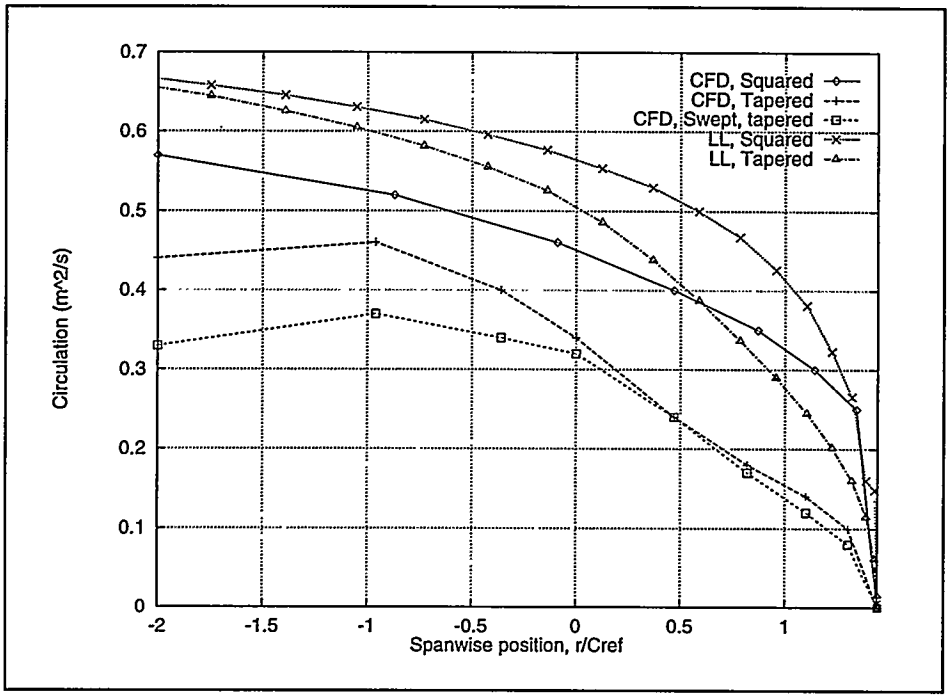

Figure 5-5 *Spanwise distribution of circulation from CFD and lifting line calculations for the different tips at an angle of attack on 10 deg.*

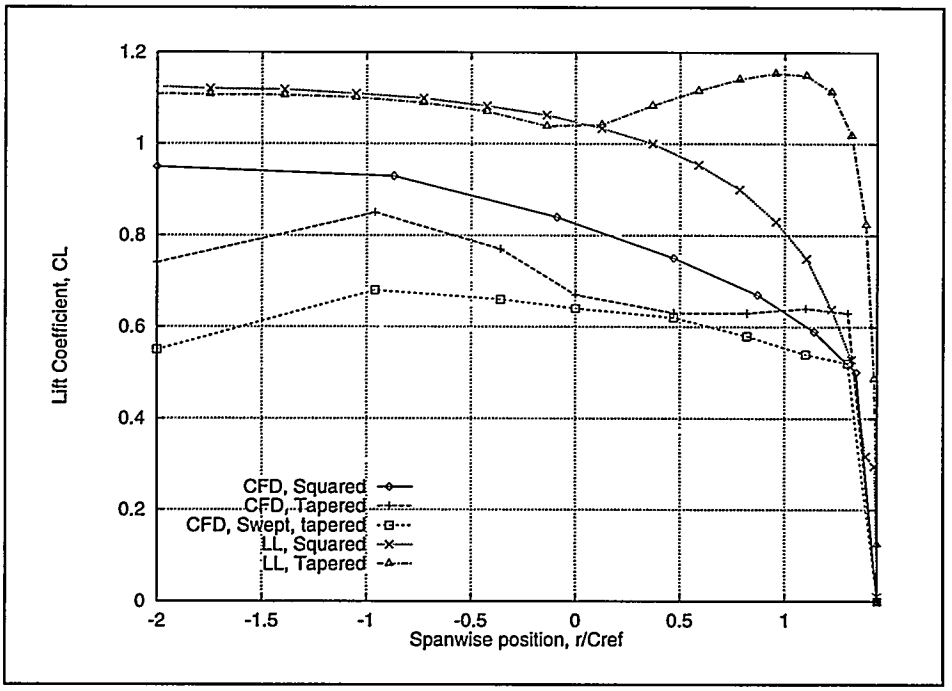

Figure 5-6 *Spanwise distribution of the lift coefficient from CFD and lifting line calculations for the different tips at an angle of attack on 10 deg.*

Figure 5-7 and Figure 5-8 show the circulation and the lift coefficient for the angle of attack on 17 deg. It has not been possible to converge the lifting line model at this high incidence. Compared to the lower angles of attack, the flow is now more or less separated and this has strongly affected the circulation at the inboard section, where the circulation has dropped compared to 10 deg. Towards the tip, the rectangular tip gain in circulation. This is because the flow becomes attached in the tip region from the reduction in the effective angle of attack from the tip vortex. As it can be seen on the lift coefficient this is also the case for the tapered tip. However the swept, tapered tip does not show an increase in the lift coefficient, and hence in the circulation.

The results from this section can be summarized in the following:

- At separated flow, the tip vortex enhances circulation because of the reduction in the effective angle of attack. This is in contrast to attached flow.
- The tapered tips perform equal at low angles of attack. The circulation is lower for the swept, tapered tip than for the tapered tip at high angles of attack. Inviscid lifting line calculations show equal performance.
- Comparison with CFD and lifting line theory has validated the CFD results, though the lift is underestimated because of poor resolution of the airfoil suction peak.
- The lifting line theory can only be used with success at low angles of attack, where the flow has not separated.

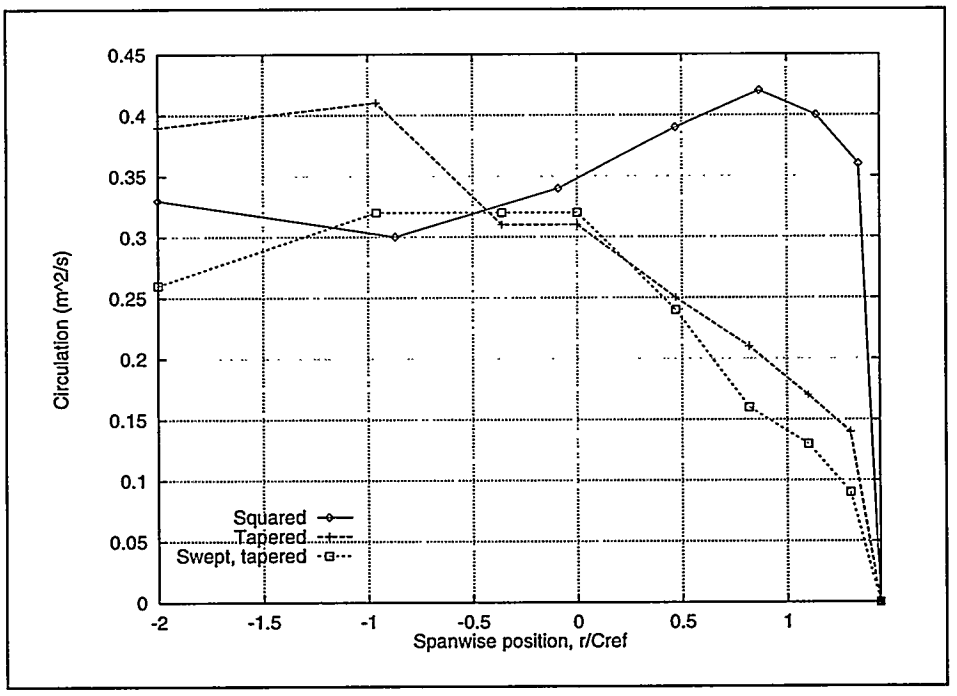

Figure 5-7 *Spanwise distribution of circulation from CFD and lifting line calculations for the different tips at an angle of attack on 17 deg.*

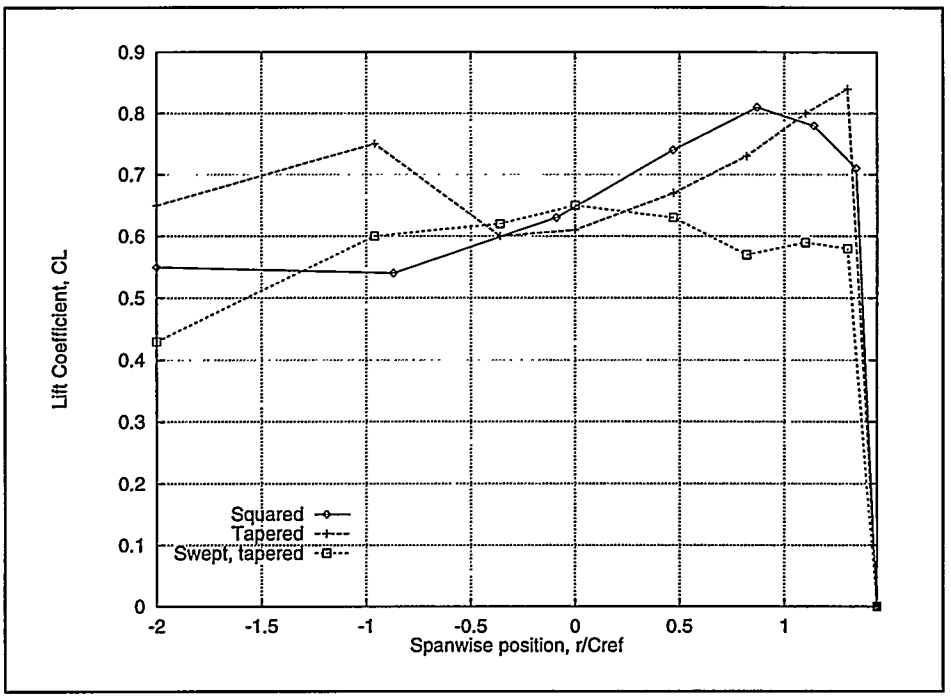

Figure 5-8 *Spanwise distribution of the lift coefficient from CFD and lifting line calculations for the different tips at an angle of attack on 17 deg.*

5.5 Tip vortex characteristics

Whereas the previous sections in this chapter mainly have concerned the flow around the tip with respect to the overall aerodynamics and the blade loading, this section concerns the aerodynamic parameters used as input data for the aeroacoustic computations. In Chapter 3, it was explained how the tip noise spectra can be described according to **George et al. (1980)** and **Brooks & Marcolini (1984)**. The input for the calculation of the tip noise spectra is the characteristic length of the tip vortex, ℓ, and the maximum velocity in the vicinity of the vortex core, V_m. From experimental results they are described to depend on the angle of attack at the tip, α_{tip}. In this section, these properties are determined from the CFD solutions at different angles of attack for the rectangular tip. Since the experimental values are obtained for non tapered tips only, the tapered and the swept, tapered tip will not be treated.

The determination of the characteristic length of the separation zone depends on a number of factors. The criteria for reattachment was in **Brooks & Marcolini, (1984)** chosen to be when the magnitude of the turbulence intensity was decreased to 5%. Probably because this is a measurable quantity with the hot-wire equipment they used in the experiment. Other criteria could be either the velocity in the vicinity of the blade or the stagnation point from the reattachment of the vortex on the suction side surface. Obviously the measured separation size would vary with the different criteria used. It is thus important, that the relationship between the separation length and the angle of attack is correct, whereas the offset is of less importance since the calculation of the tip noise spectra are scaled with the experimental results and hereby the offset is removed.

For a number of reasons, the offset is difficult to determine for a CFD calculation:

- The turbulence model that were used is known to have difficulties predicting separation well.
- The mesh density will probably influence the extent of the separation zone.
- The theory were developed for a infinite 2-dimensional span. It is difficult to take into account the reduction in the loading from the finite span and "tunnel effects", from the limited calculation domain.

It was chosen to determine the characteristic length of the separation, ℓ, by calculating the turbulent kinetic energy and find the contour line that holds 0.05. The turbulent kinetic energy corresponds somewhat to the turbulence intensity, that was used by **Brooks & Marcolini (1984)**.

The turbulent kinetic energy is defined as:

$$k = \tfrac{1}{2}\overline{u_i u_i} \qquad (5\text{-}2)$$

The maximum speed in the vicinity of the tip vortex is found by plotting contour lines of the speed.

The contour lines of the turbulent kinetic energy has been plotted for the rectangular tip at 5, 10 and 17 deg respectively in Figure 5-9, Figure 5-11 and Figure 5-13. The contour lines are somewhat distorted by the changes in the mesh resolution. It appears that an area of higher turbulent kinetic energy exists at the suction side of the tip. The vertical extent of the area is about the same for all angles, whereas the maximum energy and the horizontal extent is increasing with the angle of attack. Further down from the tip, the energy is decreased, where after it is again increased towards the bottom. The picture of the contour lines of the turbulent kinetic energy compares very well with the turbulence intensities from **Brooks & Marcolini, (1984)**, Figure 5-15, where it was also found, that the vertical extension of the area of contour lines was about the same for all angles.

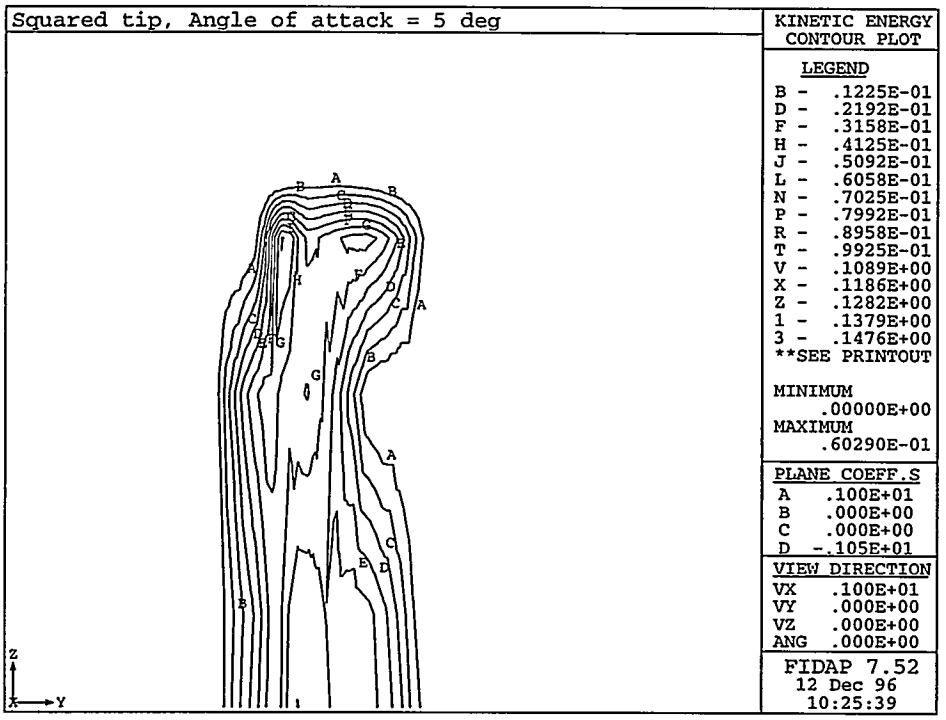

Figure 5-9 *Contour plot of the turbulent kinetic energy for the squared tip at 5 deg in the plane perpendicular to the span and to the flow, 0.05 chord downstream from the trailing edge.*

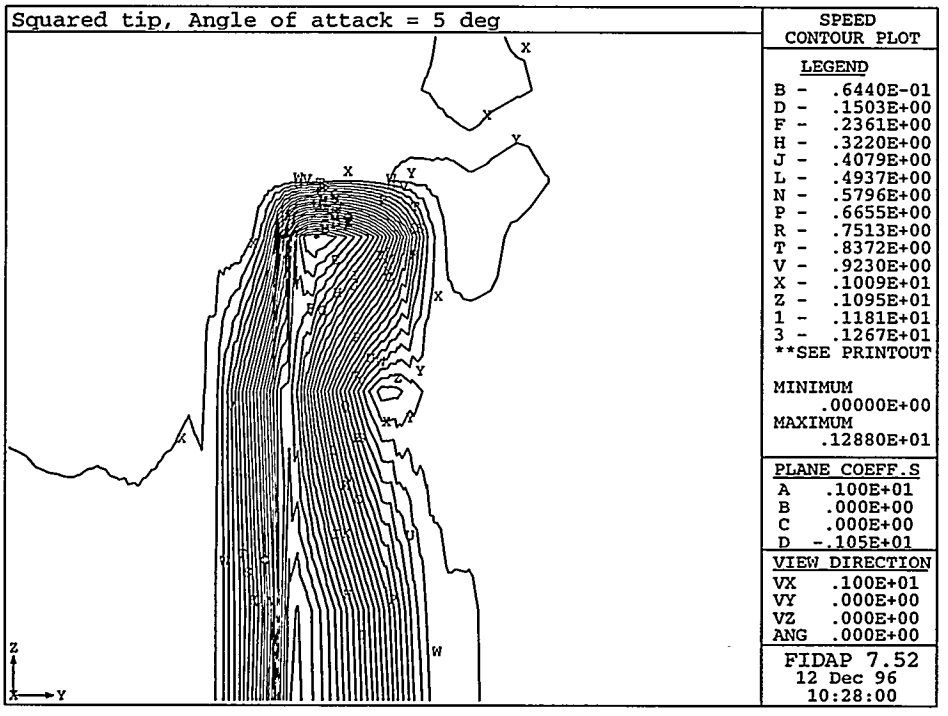

Figure 5-10 *Contour plot of the velocity magnitude for the squared tip at 5 deg in the plane perpendicular to the span and to the flow, 0.05 chord downstream from the trailing edge.*

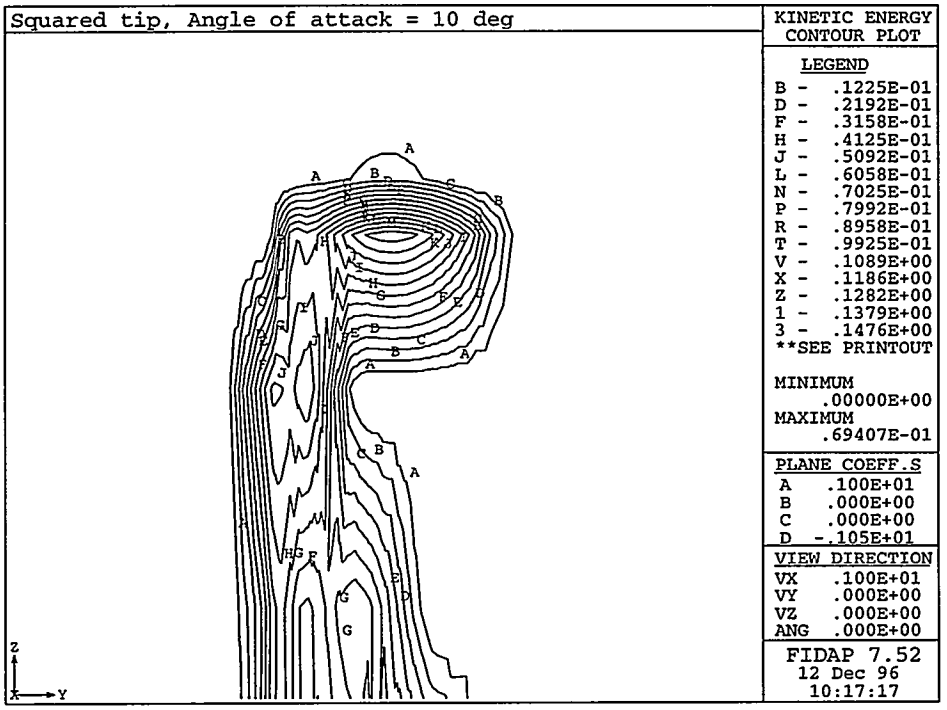

Figure 5-11 *Contour plot of the turbulent kinetic energy for the squared tip at 10 deg in the plane perpendicular to the span and to the flow, 0.05 chord downstream from the trailing edge.*

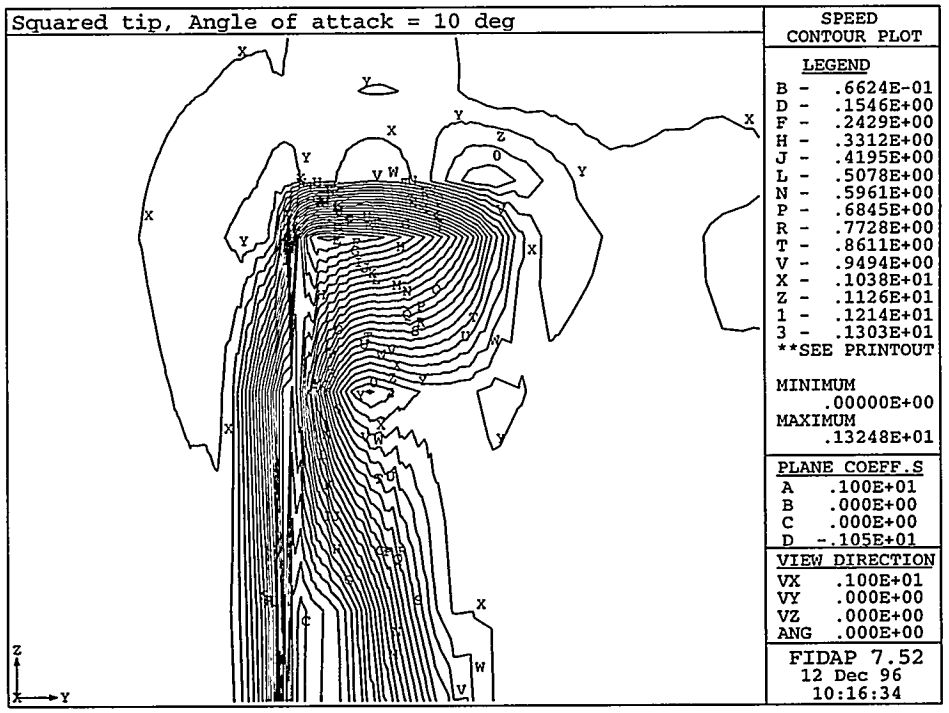

Figure 5-12 *Contour plot of the velocity magnitude for the squared tip at 10 deg in the plane perpendicular to the span and to the flow, 0.05 chord downstream from the trailing edge.*

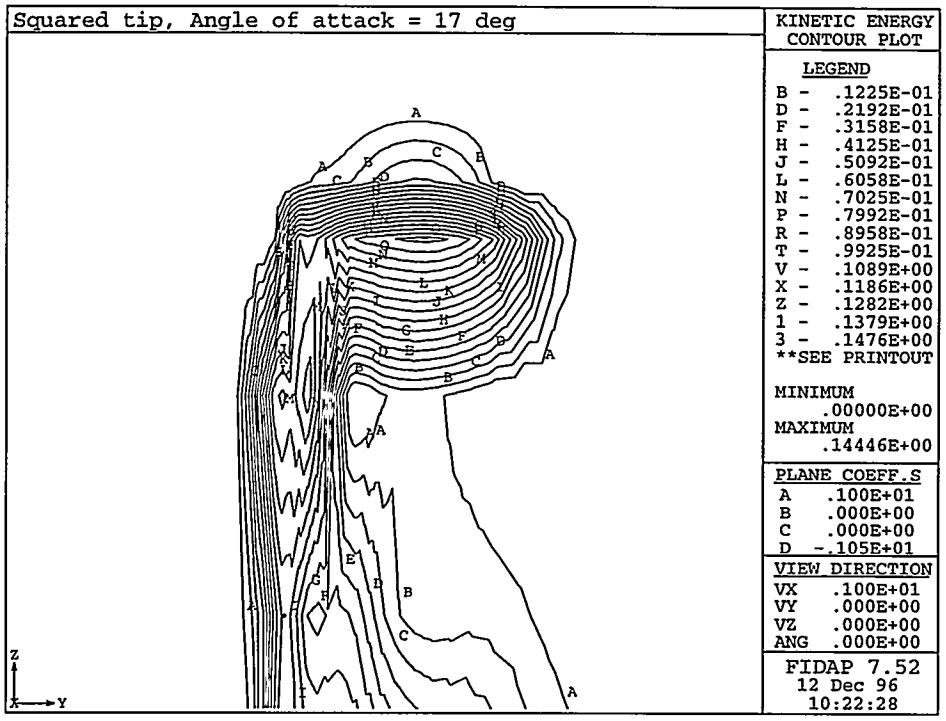

Figure 5-13 *Contour plot of the turbulent kinetic energy for the squared tip at 17 deg in the plane perpendicular to the span and to the flow, 0.05 chord downstream from the trailing edge.*

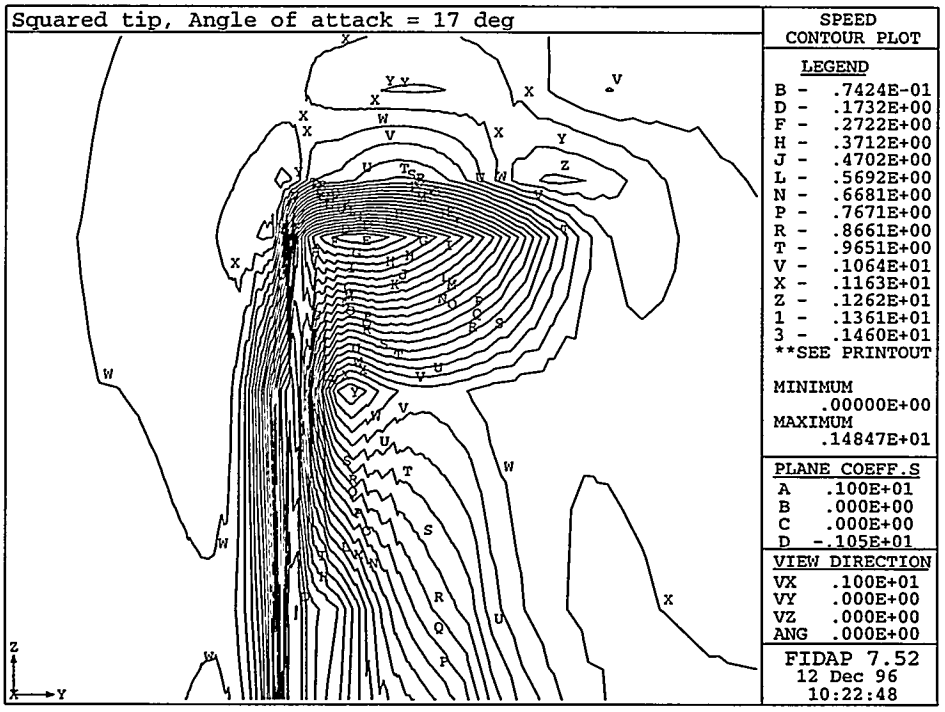

Figure 5-14 *Contour plot of the velocity magnitude for the squared tip at 17 deg in the plane perpendicular to the span and to the flow, 0.05 chord downstream from the trailing edge.*

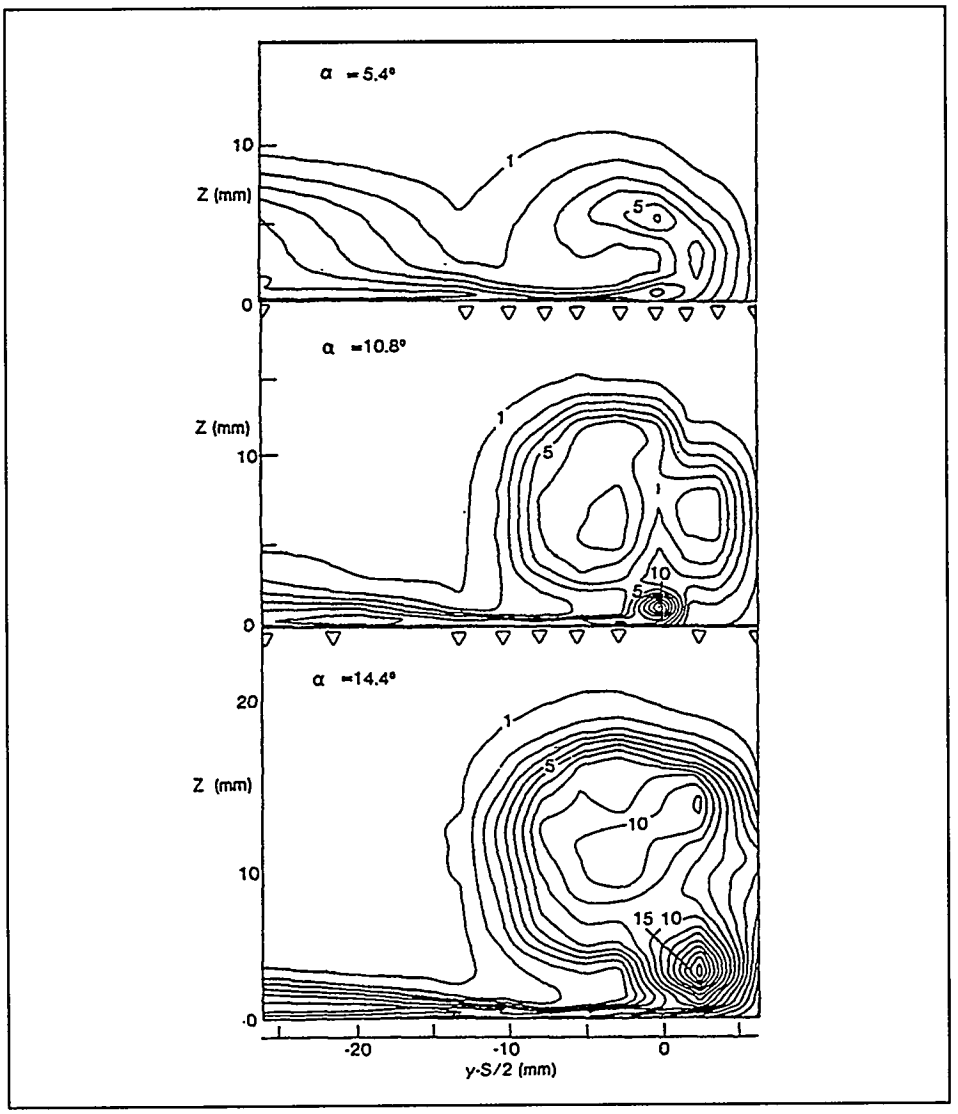

Figure 5-15 *Measured turbulence intensity, u'/U contours on the suction side of a tip region for three different angles, from* ***Brooks & Marcolini (1984).***

Figure 5-10, Figure 5-12 and Figure 5-14 show the corresponding contour lines of the speed. It can be seen that the area of maximum speed is found just outside the vortex core in the area below the tip region. This is in the area of low turbulent energy and it compares well with **George et al. (1980)**. It appears that additional secondary areas of high speed are located around the vortex core, especially for higher angles of attack.

Before the predicted values can be plotted as a function of the angle of attack at the tip, α_{tip}, this has to be corrected to compensate for the finite span. According to **Brooks & Marcolini (1984)**, this can be done by defining a reference loading in free 2-dimensional flow for an infinite span. In this way the angle of attack can be corrected from the following:

$$\alpha'_{tip} = \left[\left(\frac{\partial L / \partial z}{\partial L / \partial z_{ref}} \right)_{z \to z_{tip}} \right] \cdot \alpha_{tip} \qquad (5\text{-}3)$$

where L is the lift per unit span and z is the spanwise direction.

In this way the slope of the circulation towards the end of the span for the actual case is compared with the reference case. In our case, the aspect ratio is 7, which gives a value of approximately 0.8 for the expression in square bracketts (5-3) according to **Brooks & Marcolini (1984).**

Figure 5-16 shows the separation length versus angle of attack for the rectangular tip. It is compared with expressions obtained from experiments by **George et al. (1980)** and **Brooks & Marcolini (1984).** It appears that the rectangular tip separation size is somewhat overestimated. However, more important is that the slope of the curve is in good agreement with the experiments. The result at 17 deg (corrected to 13.6 deg) is of less relevance since the suction side flow is detached.

Figure 5-17 shows the maximum velocity, V_m versus the angle of attack. This is compared to **George et al. (1980). Brooks & Marcolini (1984)** used the same expression. Again a fair agreement is obtained. The deviation between the two curves is below 10% at low angles of attack and almost zero at higher angles of attack.

Results from this section in summary:

- The contour plot of the turbulent kinetic energy is found to be well suited for finding the characteristic size of the separation zone.
- The contour plot of the speed is used for finding the maximum velocity in the vicinity of the tip vortex core.
- Fair agreement is found between the CFD results and the experimental results. The slope of the separation length and the maximum velocity with angle of attack compares very well, whereas the offset of the characteristic length is somewhat overestimated.

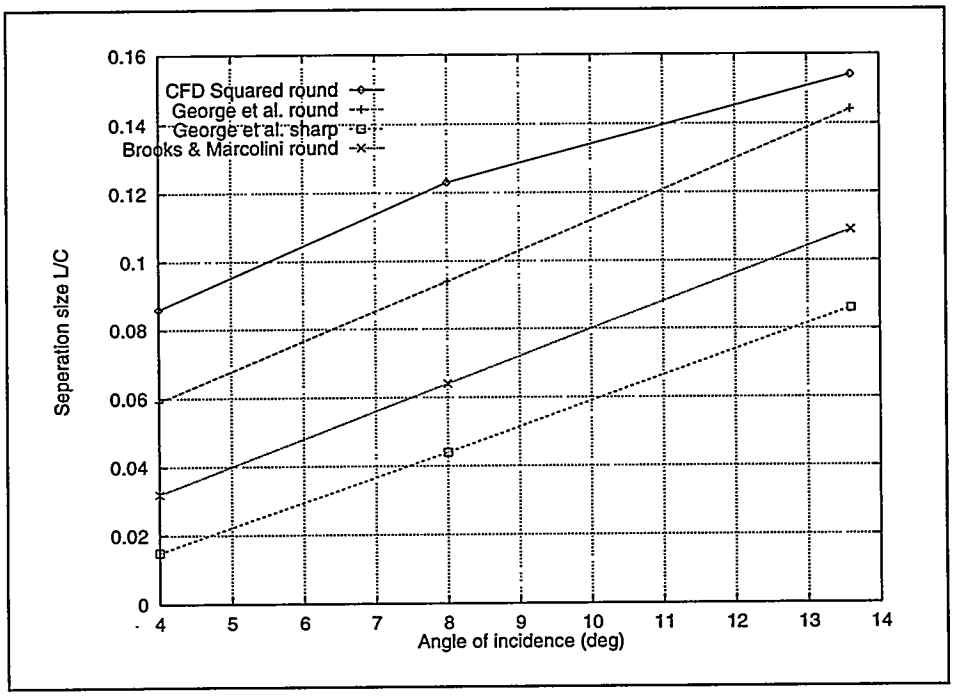

Figure 5-16 *The size of the tip vortex separation zone for CFD results from the rectangular tip compared with experimental results used by* ***George et al. (1980)*** *and* ***Brooks & Marcolini (1984).***

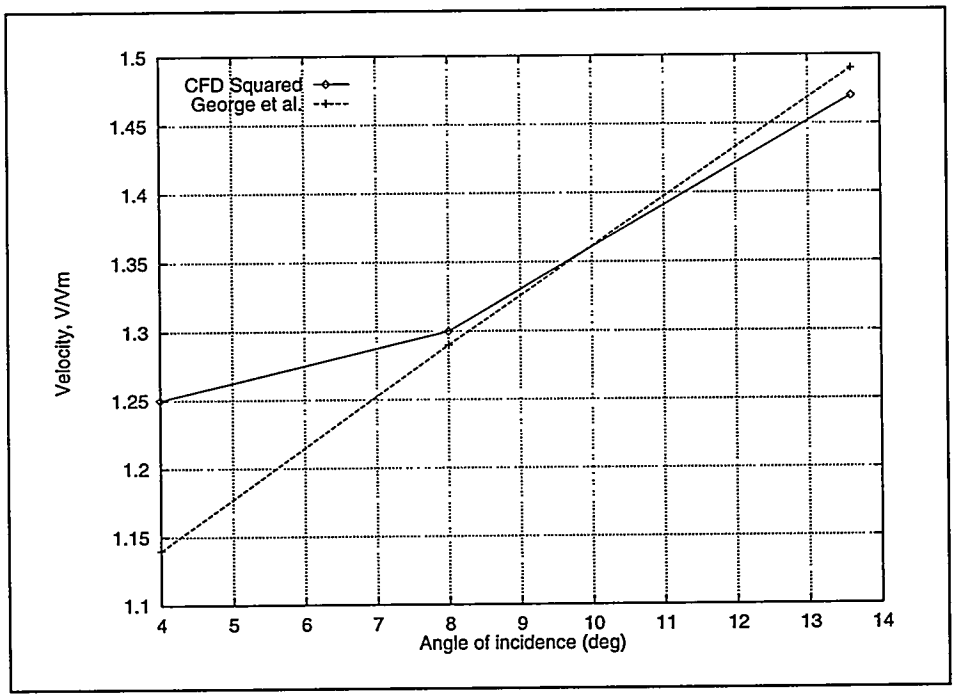

Figure 5-17 *The maximum velocity in the vicinity of the tip vortex for the CFD results from the rectangular tip compared with experimental results used by* ***George et al. (1980)*** *and* ***Brooks & Marcolini (1984).***

6. Discussion of Design Aspects

In this chapter different aspects of tip design will be commented on, based on the results of the previous chapters. Finally, some guidelines for tip design will be presented.

6.1 Requirements to an optimal tip

A number of requirements can be set up for an optimized tip:

- Low noise emission
- Optimal aerodynamic and aeroelastic characteristics
- Good manufacturing qualities
- Robust for transport and handling of the hole blade
- Good aesthetics

The different requirements are listed in accordance to a judgment of their individual relative importance. By the optimal aerodynamic and aeroelastic characteristics is meant the requirements that will be the result of an overall optimization of the blade as mentioned in Chapter 2. Therefore, it is not necessarily a tip shape with the maximum aerodynamic efficiency that will be the target.

It was also shown in Chapter 2, Figure 2-5 and Figure 2-8 that changes of the tip shape can have a considerable influence on the C_L distribution in the tip region and thus also on the stall characteristics of the blade. This again couples to the dynamics of the blade in stall and specific requirements to the tip design could thus arise from detailed analysis of loads and blade dynamics in stall.

6.2 Design aspects

As a starting point in a tip design process it seems convenient to start with an optimized blade using, e.g., the comprehensive numerical optimization procedure of **Fuglsang and Madsen (1995)**. This fulfills partly item b in the above list although it does not give the exact design of the tip planform, but only the twist and chord distribution.

Recently, the optimization procedure was extended to also include aerodynamic noise. An aeroacoustic model based mainly on the work of **Brooks, Pope and Marcolini (1989)** was implemented, **Fuglsang and Madsen (1996).** This is an important step since constraints can now be applied to the overall noise emission. The aeroacoustic model includes the tip noise model of **Brooks and Marcolini (1986)** and principally an aeroacoustic optimization of the tip is thus included. However, it seems that this tip noise model cannot handle tip designs basically different from rectangular tip planforms and even for these tips, the coupling of the aeroacoustics to the flow and thus also the geometry is only through two parameters, the tip vortex separation length L and the maximum vortex velocity V_m.

Before a more detailed and sophisticated tip noise model is developed the tip design as concerns the aeroacoustics has to be performed in a more "soft" way and not directly coupled to numerical optimization. Continuing from an optimized blade as, e.g., shown in Figure 2-2 and Figure 2-3 we will define the tip design problem as the detailed design of the most outer part of the blade, e.g., the last half

meter of the span. It is important to note at this point, that the tip design problem also involves considerations about the other noise sources as for example the trailing edge noise from the turbulent boundary layer. However, the principal discussion of design aspects will here be limited to tip noise because a detailed design must be based on detailed numerical calculations of the different noise sources.

Since the tip noise arises from the separation of the tip vortex there seems to be two different design directions to choose in order to limit the tip noise:

1) Reduce the tip vortex strength as much as possible
2) Reduce or remove the separation of the tip vortex by proper design of the tip.

A combination of the two directions is also possible, at least to some extent.

Comments on approach 1

To reduce the tip vortex strength, the circulation should be gradually decreased to zero as it was demonstrated in Chapter 2, when comparing the characteristics of the two different tip shapes in Figure 2-5. The circulation is proportional to both the chord and the angle of attack, hence these are the two important parameters for controlling the spanwise variation of the circulation. However, even for the blade with the rather slender tip planform and with the chord decreasing almost to zero, Figure 2-5, a concentrated tip vortex is still created as it was shown in Figure 2-10. The drawback by reducing the tip chord to a very small value is that also the Reynolds number is reduced and this increases the risk for laminar vortex shedding. A considerable influence from laminar vortex shedding was shown in Figure 3-14 for a Reynolds number around 0.9 mill. Furthermore, it was shown in Figure 3-15, that the effect of laminar vortex shedding decreases for an increasing Reynolds Number up to around 1 mill. If the limit for minimum Reynolds number is set to 1 mill in order to minimize the influence from laminar vortex shedding the minimum chord length will be around 0.21 m for a tip speed of 60 m/s.

The other parameter controlling the circulation is the angle of attack, which can be changed by changing the twist distribution of the blade. As an example is shown a twist distribution in Figure 6-1, where the twist is increased up to 5 degrees over the last 1 m of the span at the tip in order to decrease the angle of attack. However, in most of the tip region a surprisingly small effect is seen on the circulation, Figure 6-2 and its derivative, Figure 6-3.

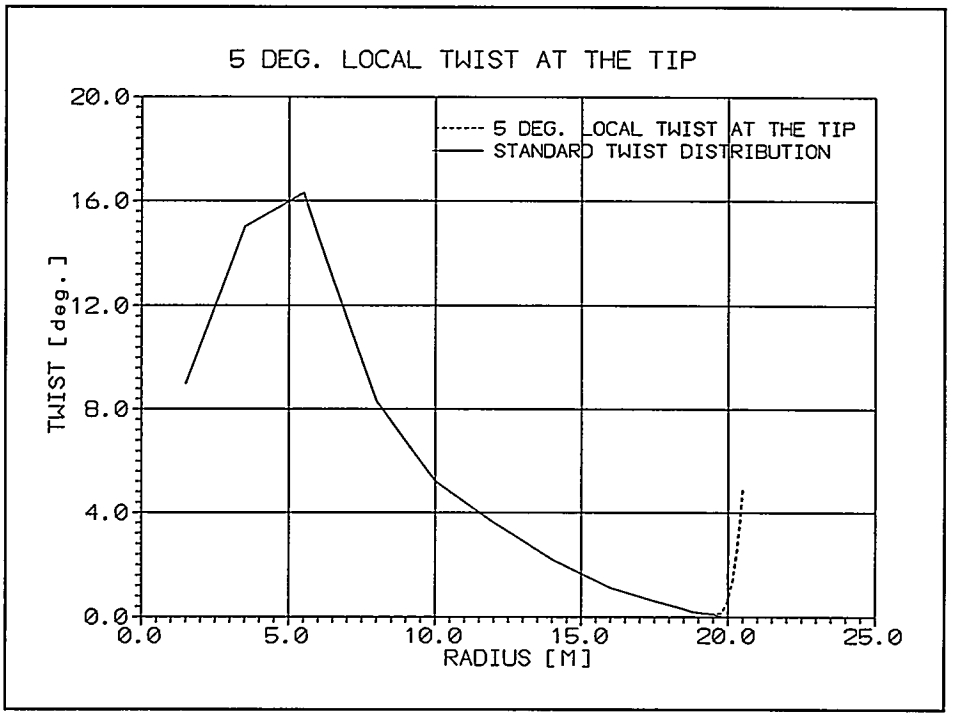

Figure 6-1 *Example of using local positive blade twist at the tip to reduce the loading and the circulation.*

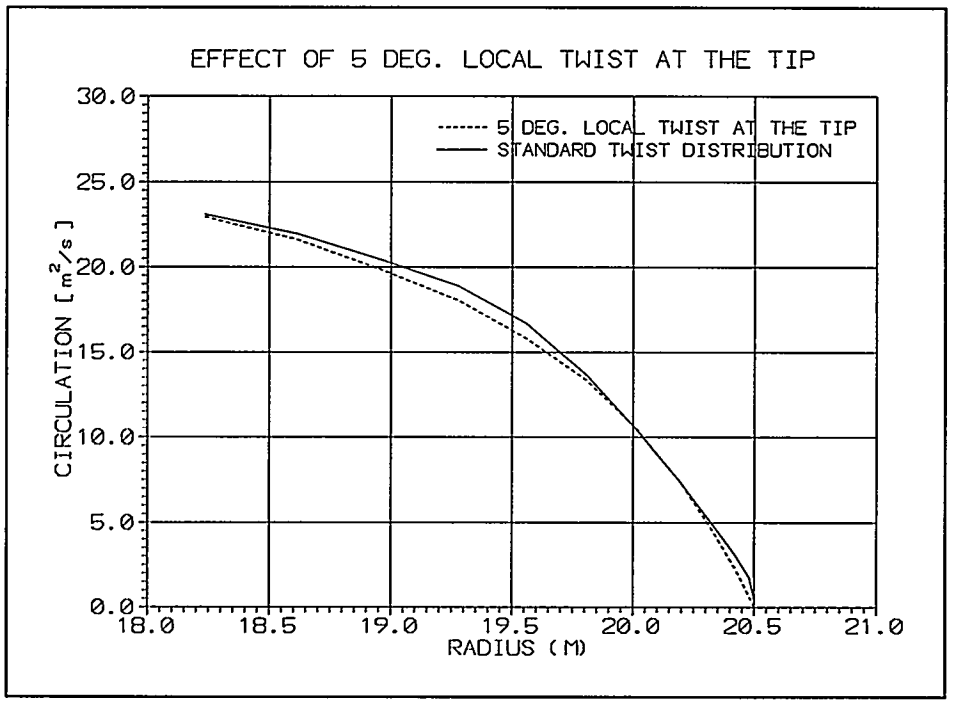

Figure 6-2 *Effect on the circulation from local positive twist at the tip of the blade.*

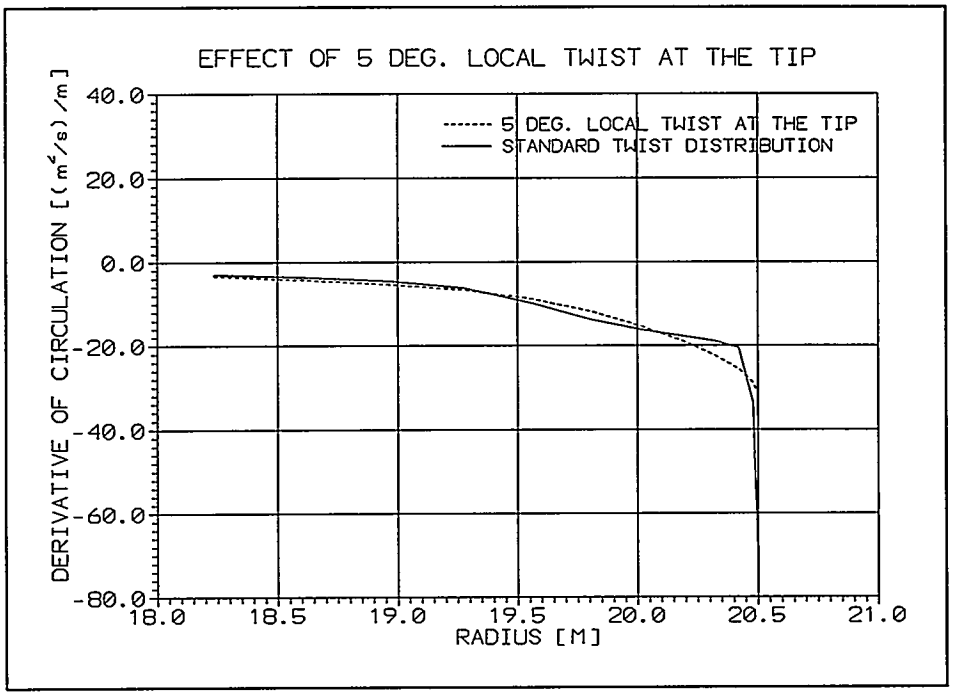

Figure 6-3 *The influence on the derivative of the circulation from the local positive twist of the blade at the tip.*

Comments on approach 2

It is clear from the models of the tip noise described in Chapter 3 that the tip noise can be removed if the tip is designed in such a way that no separation occurs in the tip region. The main idea in this second approach is to reduce or completely remove flow separation caused by the tip vortex by proper design of the tip.

A sketch of this tip, designed for a nonseparating tip vortex (NSTV Tip) will be derived from studies of the tip vortex by both experimental results as well as the CFD simulations shown in Chapter 5. During the past many different experimental studies of the tip vortex role up mechanism have been carried out and results from three such experiments will be shown here.

Hoffman and Velkoff (1971) studied the local flow around a rectangular tip using flow visualization with ammonia vapor expelled from a network of small orifices in the tip, Figure 6-4. The flow from the pressure to the suction side starts close to the leading edge and at 50% chord (section B-B) two secondary vortices are clearly seen. Close to the trailing edge, the nature of the flow is not clearly illustrated with the flow visualization technique as noted by **Hoffman and Velkoff (1971)** and the sketch for the flow at section C-C should be considered uncertain.

Francis and Kennedy (1979) used hot-wire equipment to measure the flow around a rectangular tip in a wind tunnel, Figure 6-5. Again two secondary tip vortices are seen at around mid-chord location. At the trailing edge these vortices disappear again and the lift off of the main vortex from the surface is seen.

Finally, **McInerny and Meecham (1990)** derived a sketch of the tip vortex formation based on pressure measurements, Figure 6-6 and Figure 6-7. A good agreement with the above experiments are found but it should be noted that the study was mainly focused on measuring pressure fluctuations and the above sketches should be considered qualitatively.

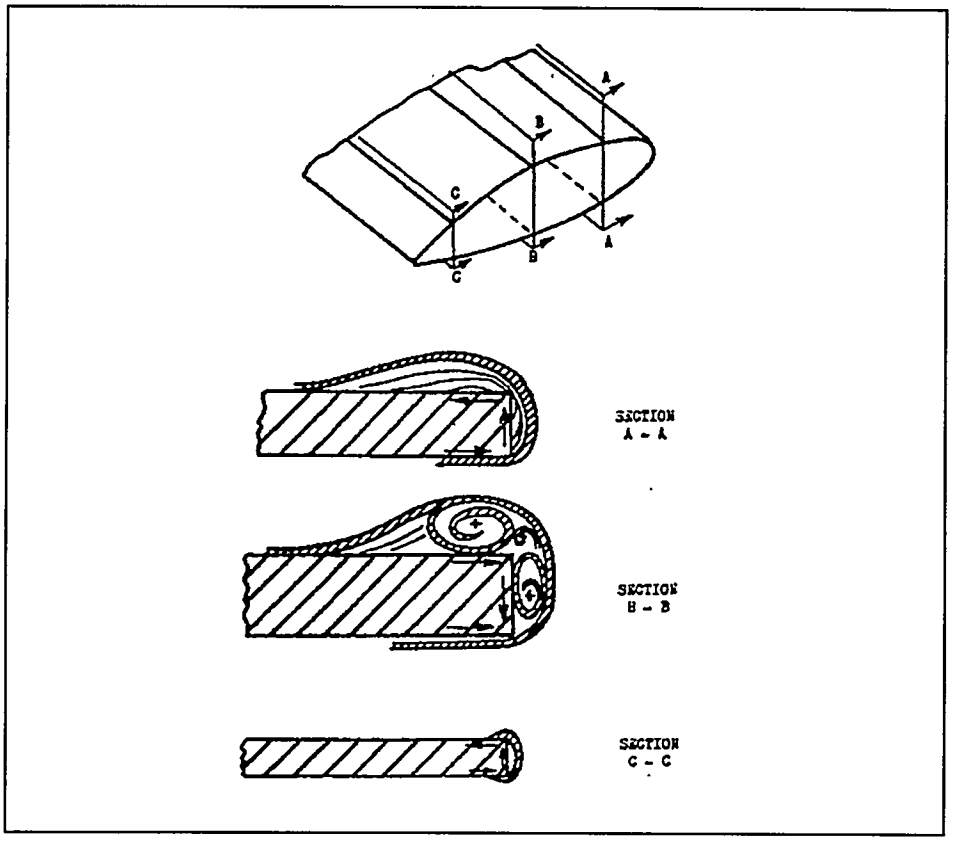

Figure 6-4 *Details of the creation of the tip vortex based on flow visualization with ammonia vapor,* ***Hoffman and Velkoff (1971)***

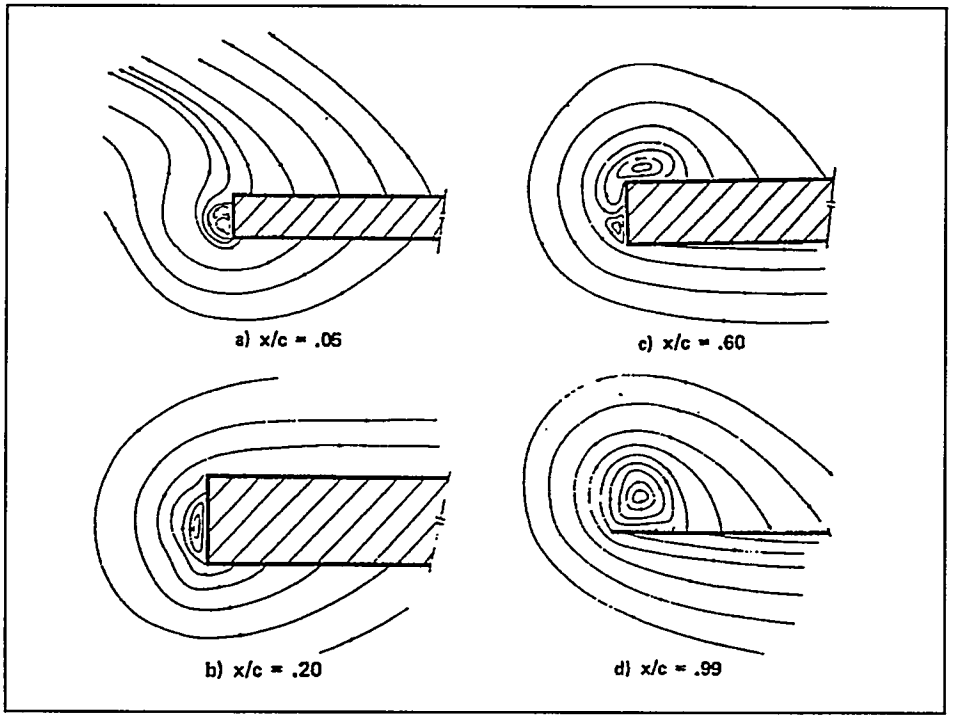

Figure 6-5 *Details of the tip vortex creation based on hot wire measurements,* ***Francis and Kennedy (1979).***

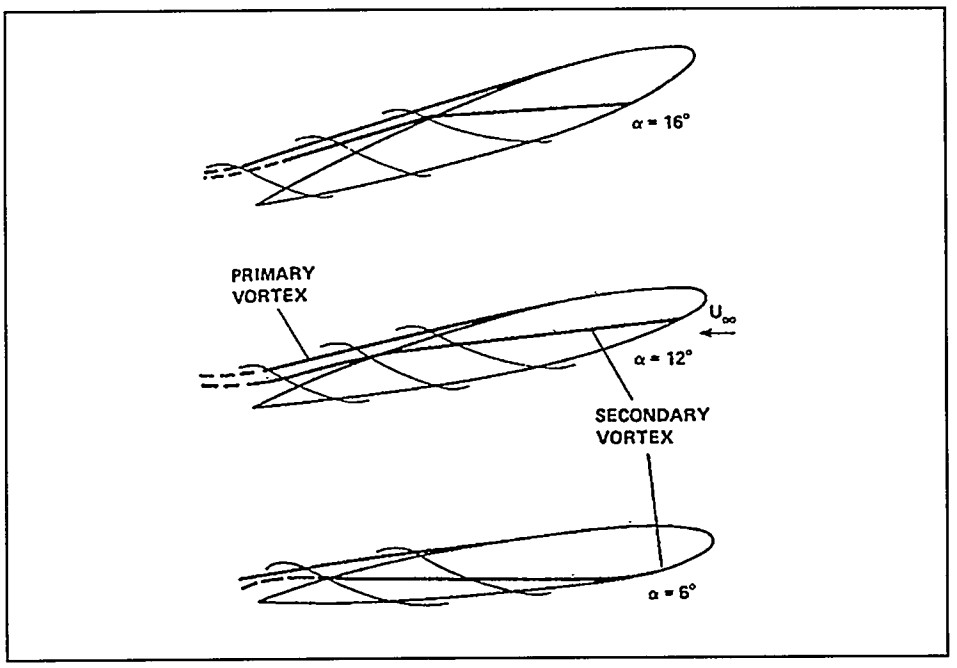

Figure 6-6 *Qualitative sketch of the tip vortex axis location (end view) based on pressure measurements,* ***McInerny and Meecham (1990).***

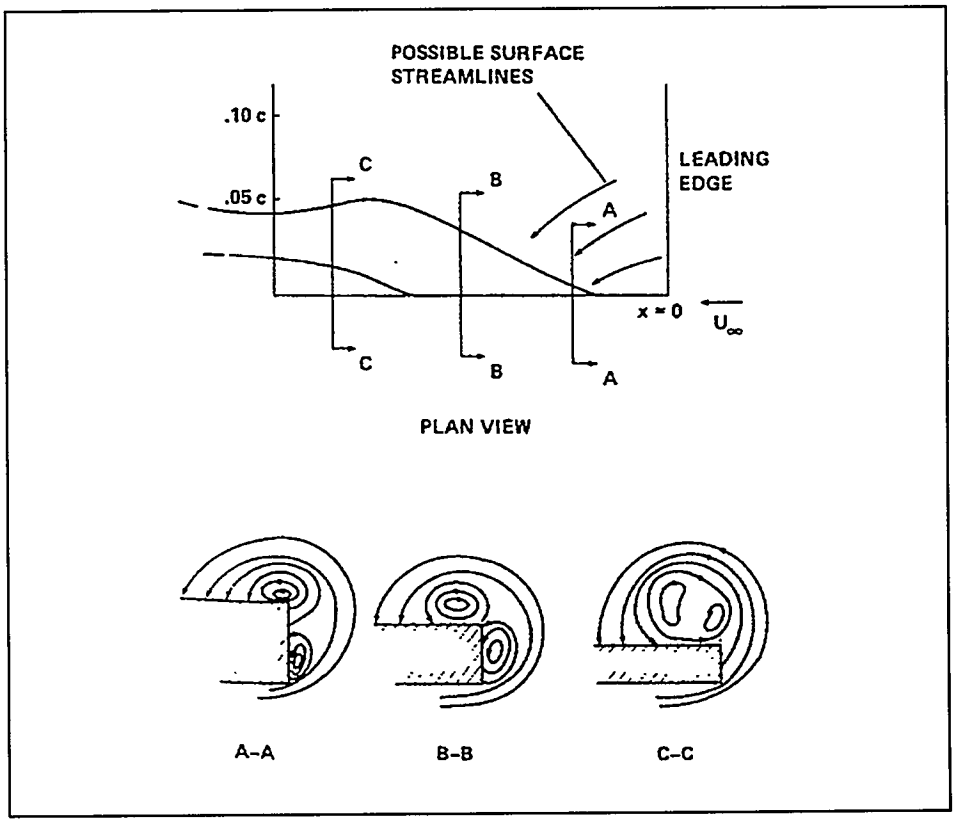

Figure 6-7 *Qualitative sketch of the tip vortex axis location (plan view) based on pressure measurements,* ***McInerny and Meecham (1990).***

Another source of information on the tip vortex formation is the CFD results from Chapter 5 of the present report. As an example is shown the velocity vectors at 75% chord in Figure 6-8.

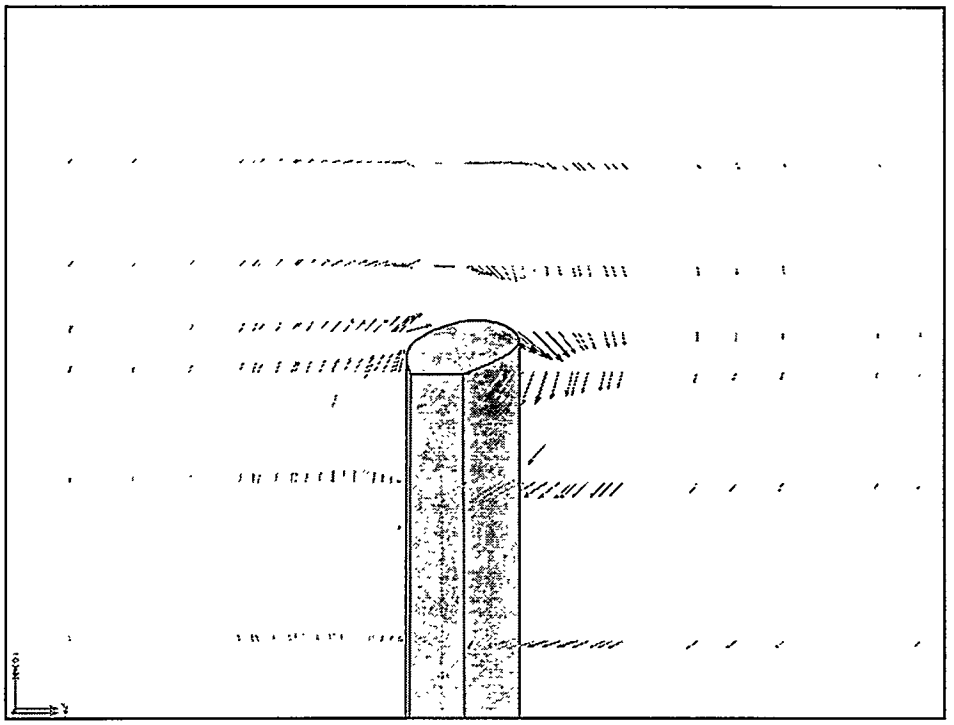

Figure 6-8 *The velocity vectors at 75 % chord position and at an angle of attack of 5 deg.*

The main tip vortex is clearly seen, but it is also evident that the details of the tip vortex inclusive the secondary vortices are not resolved with the present mesh density. To overcome this problem a 2D simulation of this crossflow was performed with a mesh covering just the tip region (about 2 chord length in x and y direction respectively and with velocity vectors imposed on these boundaries from the 3D simulation). The result of this simulation is shown in Figure 6-9 and Figure 6-10. Now the secondary vortices are clearly seen and the correlation with the above experimental results is good. However, to achieve a good set of velocity vector plots at different cross sections along the chord, a full 3D simulation with a high mesh density should be performed.

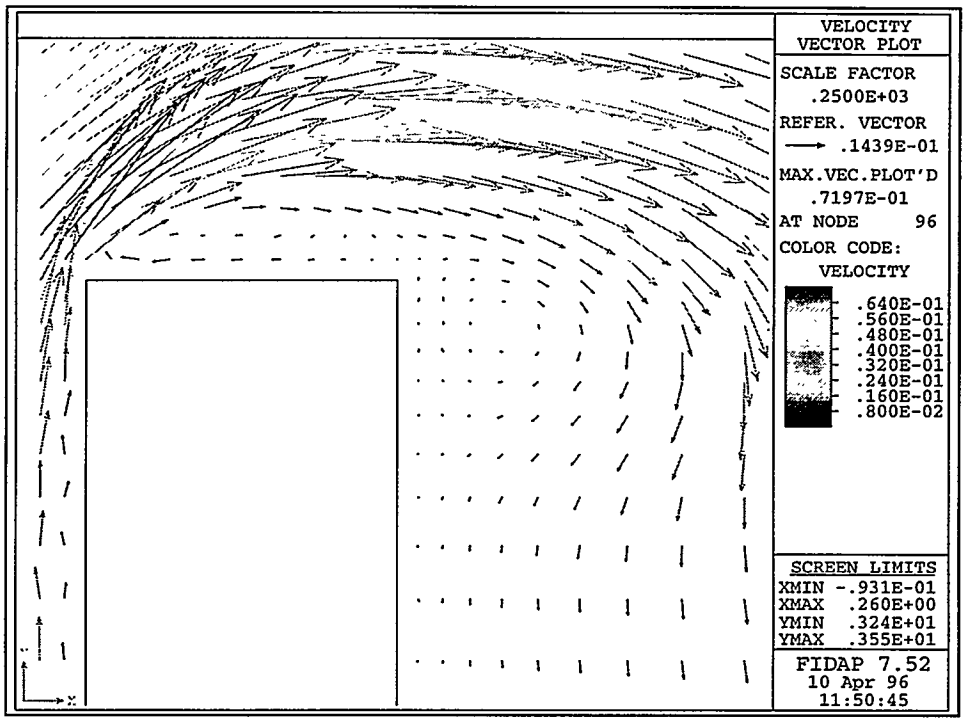

Figure 6-9 *A 2D simulation of the cross flow around the tip (velocity vectors).*

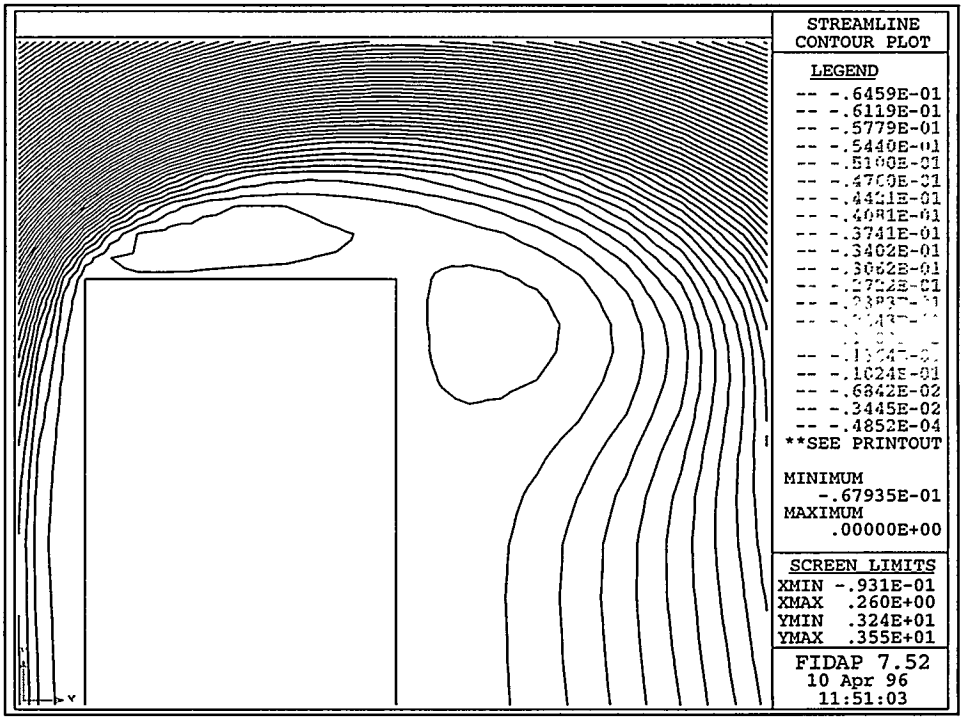

Figure 6-10 *2D simulation of the cross flow around the tip (streamlines).*

Based on the different pictures of the tip vortex flow shown above it is possible to estimate a tip shape with low or no separation by choosing a surface which coincides with the limiting streamlines of the tip vortex. Such a sketch is shown in Figure 6-11. It is believed that the tip noise will be minimal for this tip shape.

However, the details of the geometry should be based on CFD simulations on a fine mesh and probably also flow visualization studies in a wind tunnel.
A final proposal for a tip design could thus be to derive an optimized blade planform based on numerical optimization. Then to design the most outer part of the blade by choosing a minimum chord length of 0.2 m in order to avoid major contribution to the noise from laminar vortex shedding. Finally to design the tip according to the above sketch.

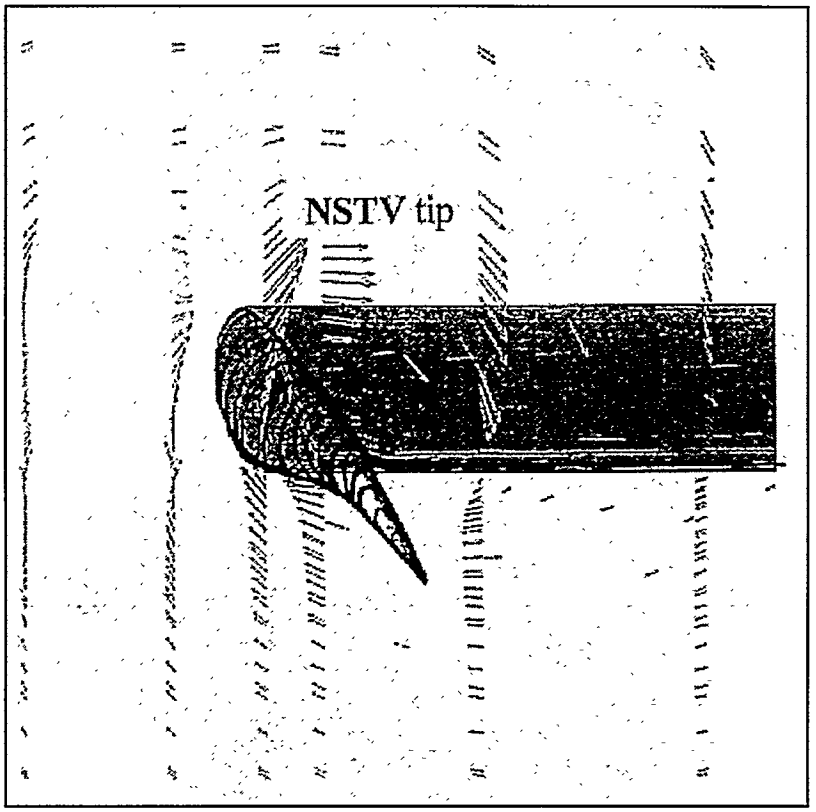

Figure 6-11 Sketch of a tip with a nonseparating tip vortex (NSTV tip).

6.3 Concluding remarks

In this Chapter the tip design was briefly commented and some conclusions can be listed:

- The strength and dimension of the tip vortex was identified as the main parameters for reducing the tip noise.
- Decreasing the chord and decreasing the effective angle of attack by local twist of the blade will reduce the above two parameters and thus also the noise.
- Noise from laminar vortex shedding can be a problem if the local Reynolds number is too low, e.g. below $0.9 \cdot 10^6$. For a tip speed of 60 m/s this corresponds to a chord length of around 0.2 m
- The tip vortex separation can be reduced by proper design of the tip shape and a non-separating tip vortex tip (NSTV tip) has been sketched

References

Antoniou I., Madsen H. A. and Paulsen U.S., 1993, "Theoretical and Experimental Investigation of New Tip Shapes". Proc. 1993 European Community Wind Energy Conference, Germany, 8-12 March 1993. pp 280-285.

Antoniou I., Madsen H. A. and Paulsen U.S., 1994, "Theoretical and Experimental Investigation of New Tip Shapes". Proceedings of the 1994 European Community Wind Energy Conference, held at Thessaloniki.

Bareiss, R. and Wagner, S., 1993, "Minutes of the 2nd Joint Project Meeting 'Development of An Aeroacoustic Tool for Noise Prediction of Wind Turbines, JOULE II, JOU2-CT92-0148' together with the projects JOUR-CT90-0107, JOU2-CT92-0148, JOU2-CT92-0205, JOU2-CT92-0124, JOU2-CT92-0233, TWIN
NL), RISØ (DK)" held in Stuttgart on November 15th-16th 1993.

Bareiss, R.; Guidati G. and Wagner, S., 1994, "Minutes of the 3rd Joint Project Meeting 'Development of An Aeroacoustic Tool for Noise Prediction of Wind Turbines, JOULE II, JOU2-CT92-0148' together with the projects JOUR-CT90-0107, JOU2-CT92-0148, JOU2-CT92-0205, JOU2-CT92-0124, JOU2-CT92-0233, TWIN (NL), RISØ (DK)" held in Thessaloniki on October 11th and 12th, 1994.

Brooks, T.F. and Marcolini, M.A., 1984, "Airfoil Tip Vortex Formation Noise". AIAA-84-2308. AIAA/NASA 9th Aeroacoustics Conference, October 15-17, 1984 Williamsburg, Virginia.

Brooks, T.F. and Marcolini, M.A., 1985, "Scaling of Airfoil Self-Noise Using Measured Flow Parameters". AIAA Journal, Vol. 23, No. 2.

Brooks, T.F. and Marcolini, M.A., 1986, "Airfoil Tip Vortex Formation Noise". AIAA Journal, Vol. 24, No. 2.

Chigier, N.A. and Corsiglia, V.R., 1971, "Tip Vortices - Velocity Distributions. NASA TM X-62087.

Drela, M. and Giles, M.B., 1987, "Viscous-Inviscid Analysis of Transonic and Low Reynolds Number Airfoils.", AIAA Jr., Vol 25, No. 10.

Ekaterinaris, J.A., Srinivasan, G.R., McCroskey, W.J., 1994, "Present Capabilities of Prediting Two-Dimensional Dynamic Stall." Prec. Agard 75th Fluid Dynamics Panel Meeting, Berlin, Germany.

FIDAP Documentation, 1993, "Fidap 7.0 Fluid Dynamics Analysis Package.", Fluid Dynamics Internationals, Inc.

Francis, M.S. and Kennedy, D.A. "Formation of a Trailing Vortex". Journal of Aircraft, Vol. 16, No. 3 March 1979.

Fuglsang P.L. and Madsen H.A., 1995, "A Design Study of a 1 MW Stall Regulated Rotor". Risø-R-799(EN), Risø National Laboratory, Roskilde, Denmark.

Fuglsang, P.L. and Madsen, H.A., 1996, "Implementation and verification of an Aeroacoustic Noise Prediction Model for Wind Turbines.", Risø-R-867(EN), Risø National Laboratory, Denmark.

George, A.R., Najiar, F.E., and Kim, Y.N., 1980, "Noise Due to Tip Vortex Formation on Lifting Rotors". AIAA Paper 80-1010.

George, A.R. and Chou, S-T., 1984, "Broadband Rotor Noise Analysis". NASA CR-3797.

Gray, R.B., McMahon, H.M., Shenoy, K.R. and Hammer,M.L., 1980, "Surface Pressure Measurements at Two Tips of a Model Helicopter Rotor in Hover. NASA CR-3281.

Hardin, J.C., 1980, "Noise Radiation from the Side Edges of Flaps". AIAA Journal Vol. 18 pp. 549-552. May 1980.

Harvey, J.K., 1961, "Some Measurements on a Yawed Slender Delta Wing with Leading-Edge Separation". Department of Aeoronautics, Imperial College, A.R.C. Technical Report No. 3160.

Hoffman, J.D. and Velkoff, H.R. "Vortex Flow over Helicopter Tips". Journal of Aircraft, Vol. 8, No. 9, September 1971.

Jakobsen, J and Andersen, B, 1993, "Aerodynamical noise from wind turbine generators". EFP j.nr. 1364/89-5, JOUR-CT 90-0107.

Jakobsen, J. and Andersen, B., 1993, "Aerodynamic Noise from Wind Turbines". Proceedings of the 1993 European Community Wind Energy Conference, held at Lübeck-Travemünde, Germany, 8-12 March 1993. pp 312-315.

Kida, S, 1994, "Vortex Reconnection.", Annual Review of Fluid Mechanics, Volume 26. Annual Reviews Inc.

Launder, B.E. and Spalding, D. B., 1972, "Lectures in Mathematical Models of Turbulence," Academic Press Inc., London and New York.

Lowson, M.V. and Fiddes, S.P., 1994, "Design Prediction Model for Wind Turbine Noise". ETSU W/13/00317/REP.

Madsen H.A., "Design af en 20 kW -12.6 m stallreguleret rotor". Risø-I-809(DA), Forskningscenter Risø, Roskilde , Maj 1994. (in Danish)

McInerny, S.A. and Meecham W.C., 1990, "Pressure Fluctuations in the Tip Region of a Blunt-Tipped Airfoil". AIAA Journal, Vol. 28 No. 1, January 1990.

Petersen K.Ø., Tenbrock S. and Medelbye K., 1993, "Noise Control on the Bonus 450 kW Mk III Turbine". Proceedings of the 1993 European Community Wind Energy Conference, held at Lübeck-Travemünde, Germany, 8-12 March 1993. pp 280-285.

Yakhot, V., et al., 1992, "Development of Turbulence Models for Shear Flows by a Double Expansion Technique," Physics of Fluids, A 4 (7), 1510 - 1520

A. Results from CFD calculations

This appendix contains figures from the CFD calculations in Chapter 5.

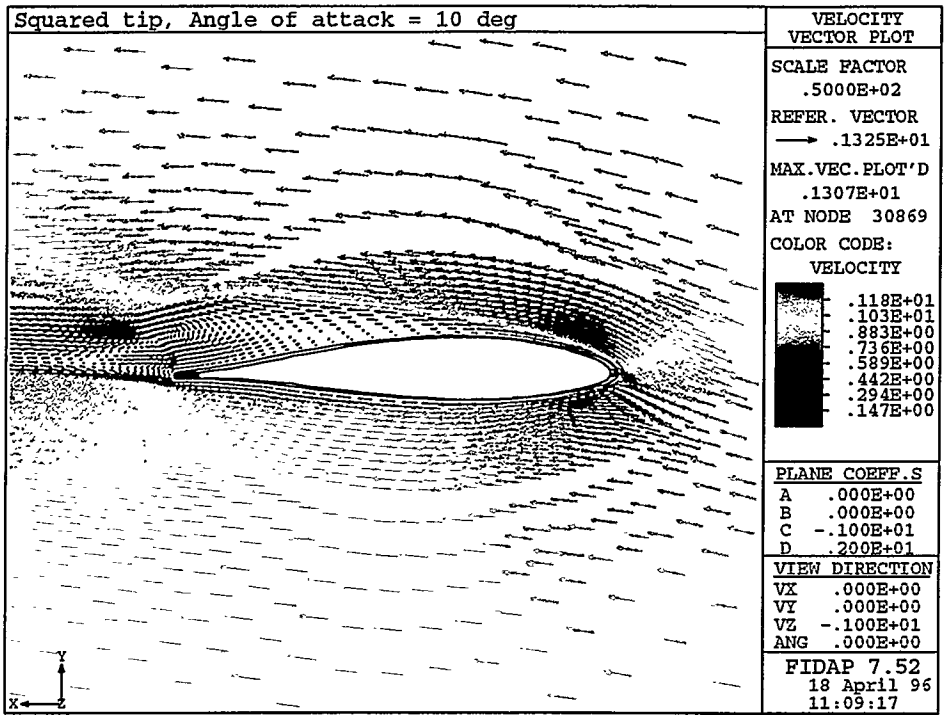

Figure A-1 *Velocity vectors in a plane perpendicular to the span, at the tip root section for the rectangular tip at an angle of attack = 10 deg.*

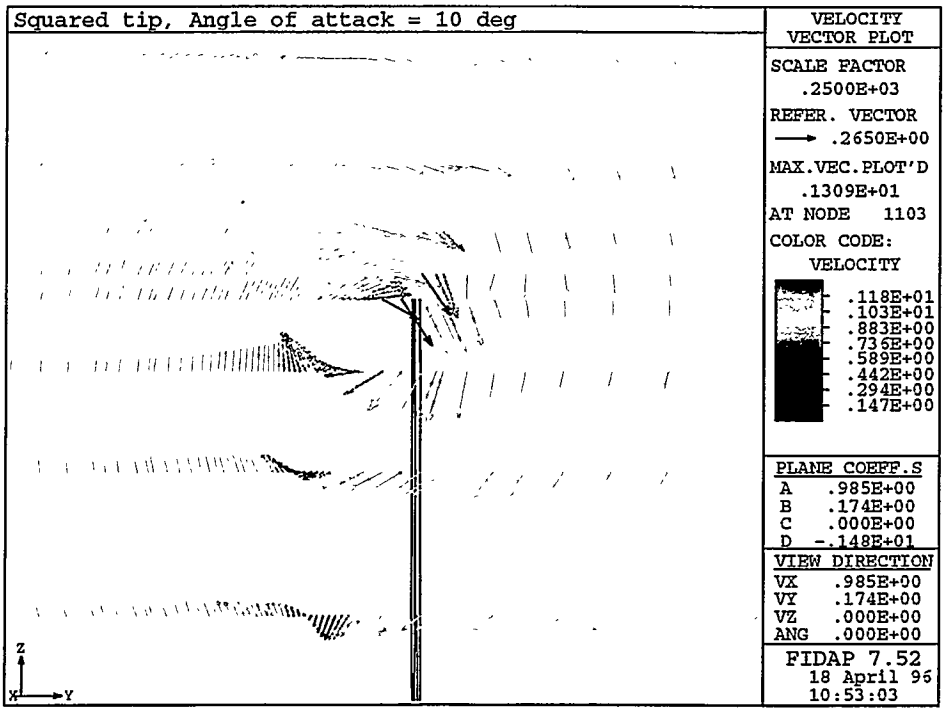

Figure A-2 *Velocity vectors in a plane perpendicular to the flow direction, 0.5 chordlength downstream from the trailing edge for the rectangular tip at and angle of attack = 10 deg.*

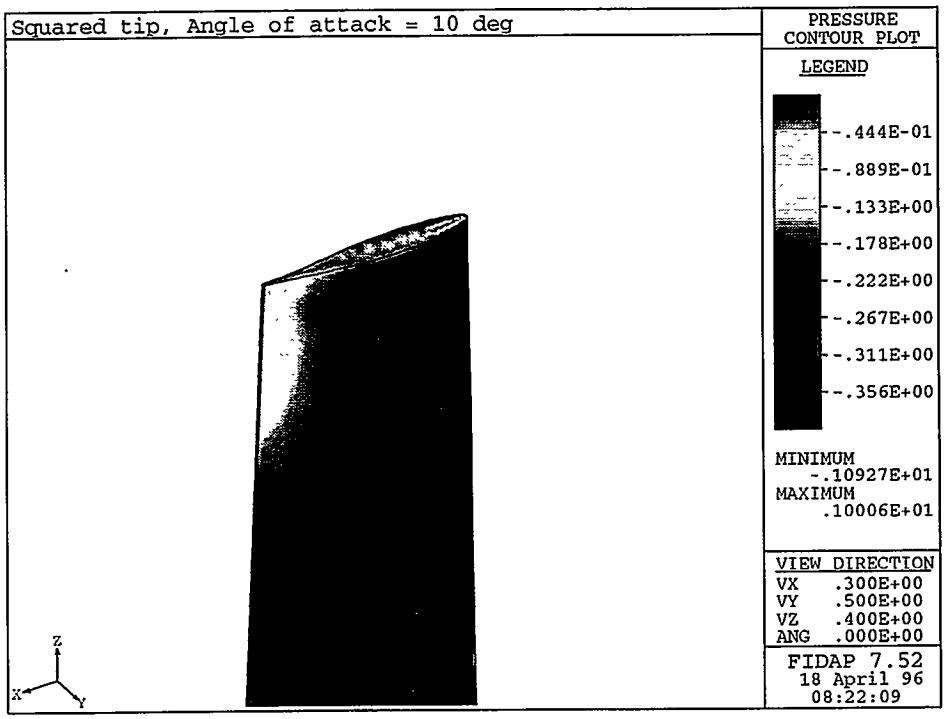

Figure A-3 *Suction side pressure distribution for the rectangular tip at an angle of attack = 10 deg.*

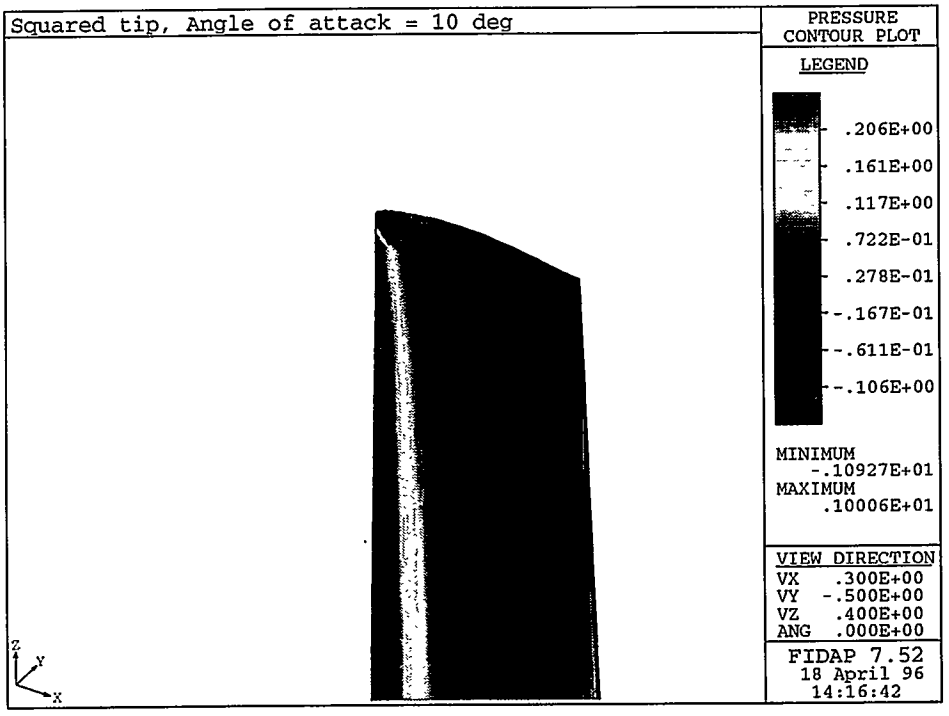

Figure A-4 *Pressure side pressure distribution for the rectangular tip at an angle of attack = 10 deg.*

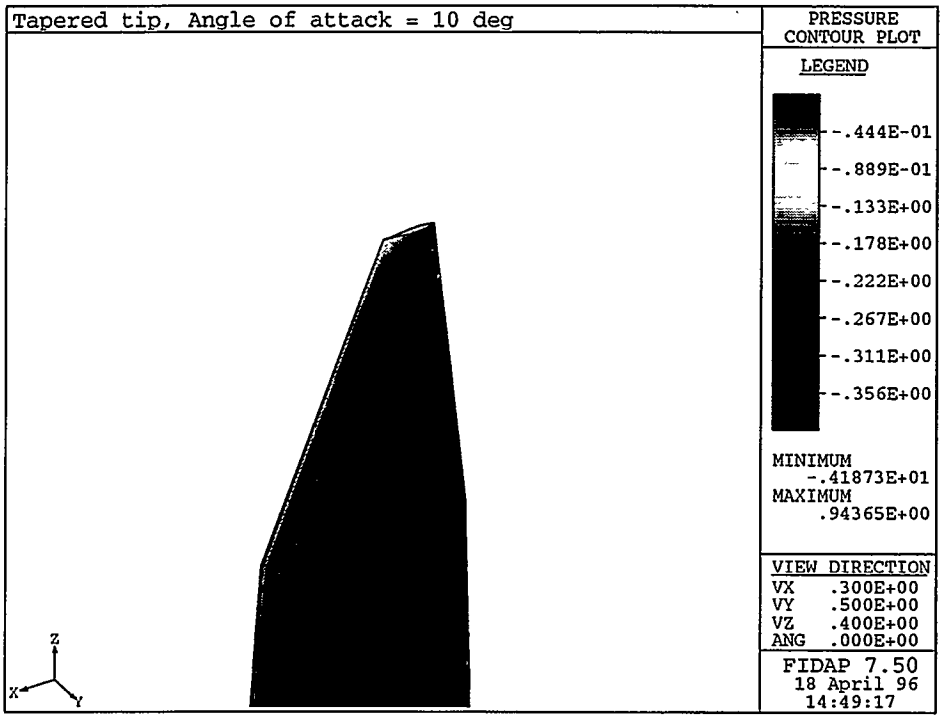

Figure A-5 *Suction side pressure distribution for the tapered tip at an angle of attack = 10 deg.*

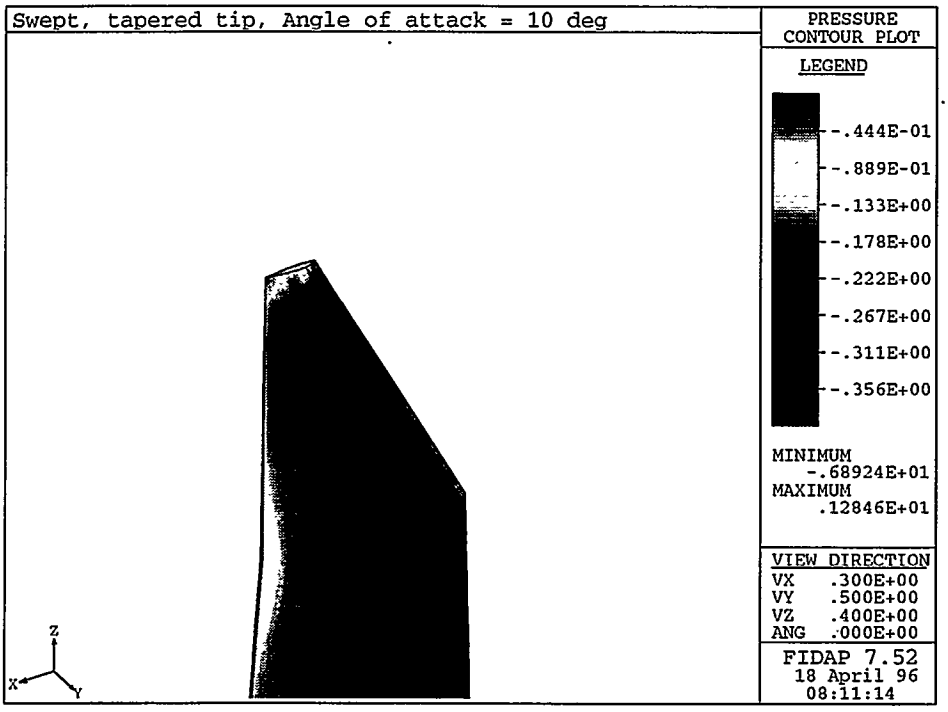

Figure A-6 *Suction side pressure distribution for the swept, tapered tip at an angle of attack = 10 deg.*

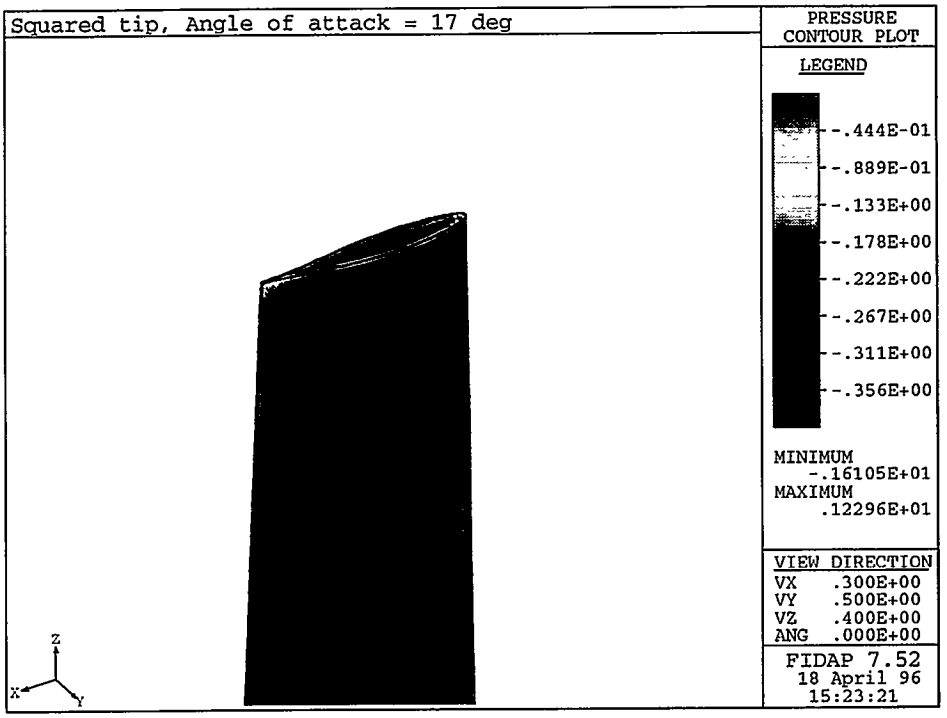

Figure A-7 *Suction side pressure distribution for the rectangular tip at an angle of attack = 17 deg.*

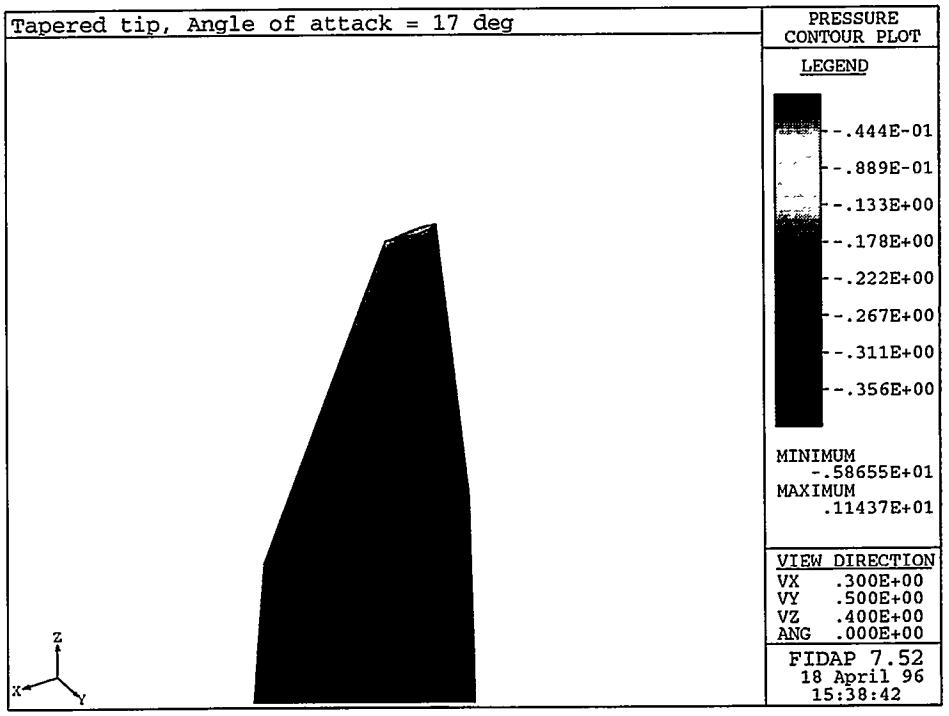

Figure A-8 *Suction side pressure distribution for the tapered tip at an angle of attack = 17 deg.*

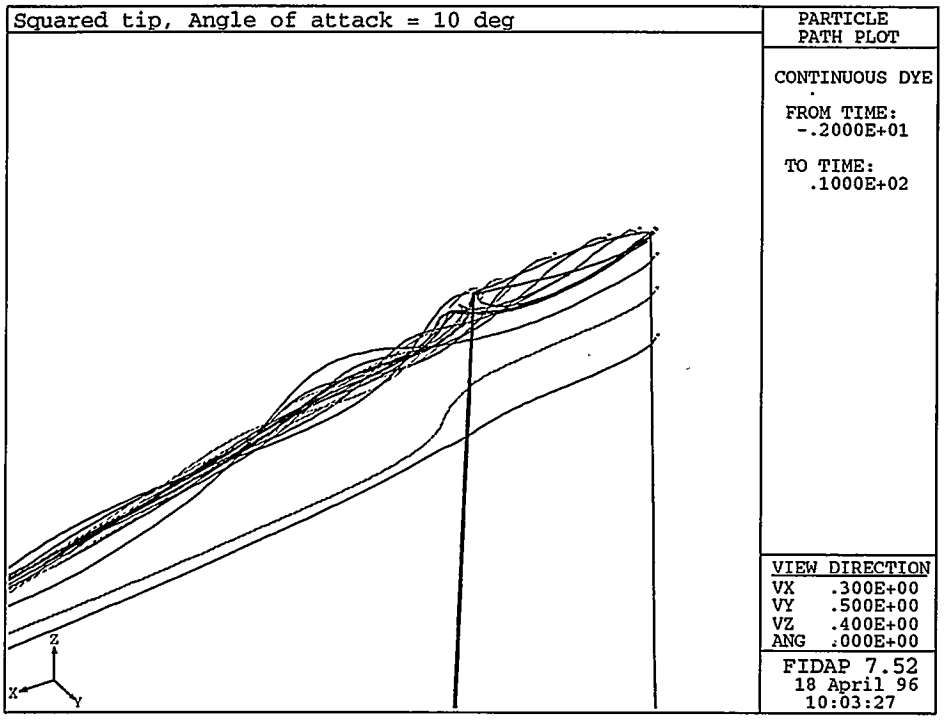

Figure A-9 *Particle trace of the tip vortex fluid motion downstream from the blade for the rectangular tip at an angle of attack = 10 deg.*

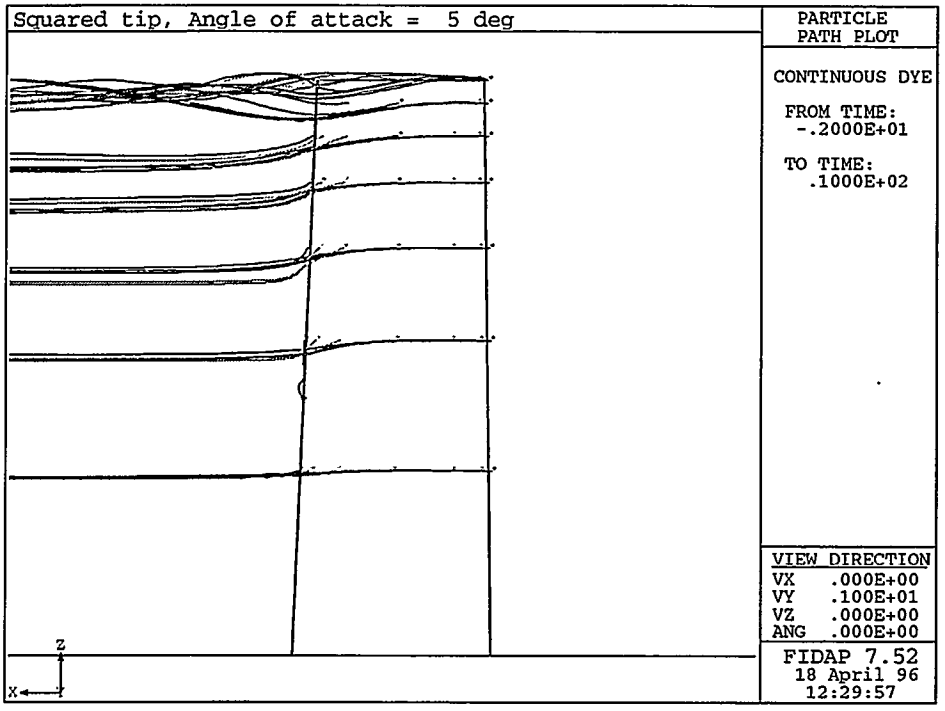

Figure A-10 *Particle trace of the fluid motion from the suction side, downstream from the blade for the rectangular tip at an angle of attack = 5 deg.*

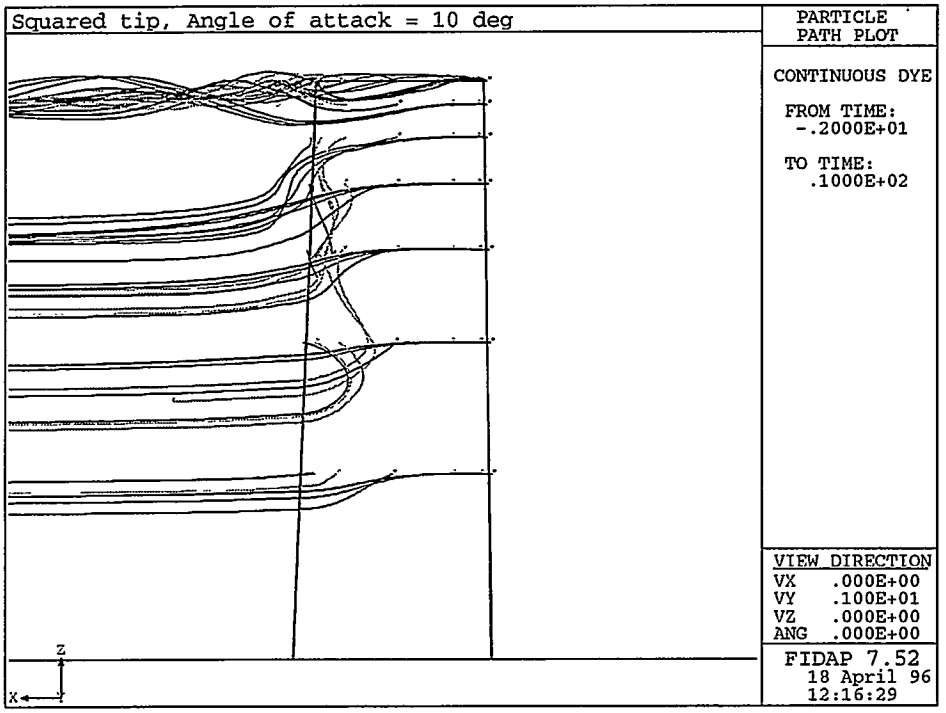

Figure A-11 *Particle trace of the fluid motion from the suction side, downstream from the blade for the rectangular at an angle of attack = 10 deg.*

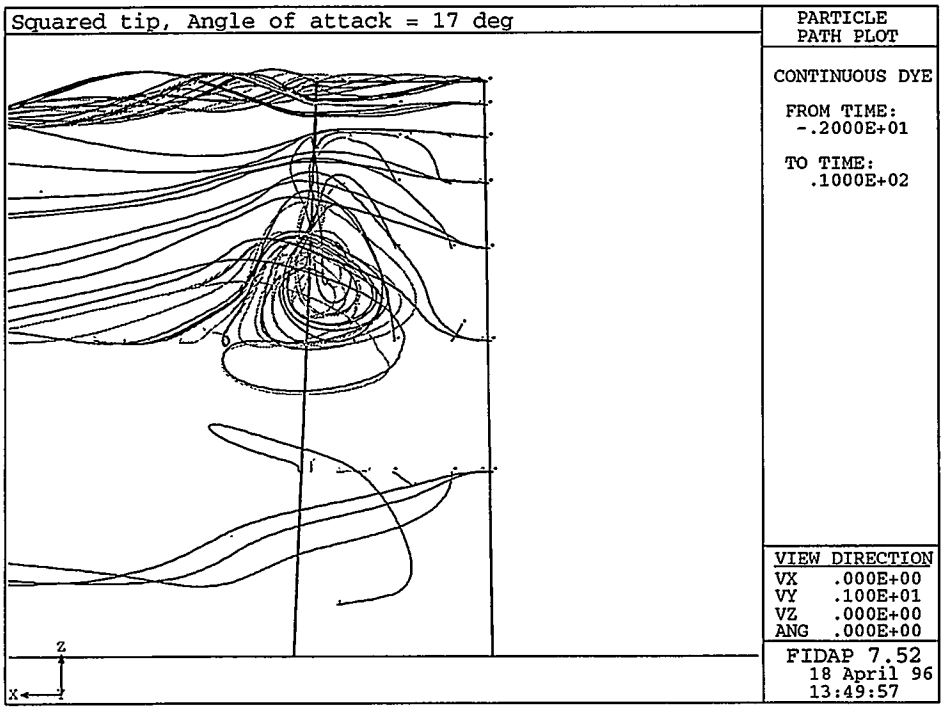

Figure A-12 *Particle trace of the fluid motion from the suction side, downstream from the blade for the rectangular tip at an angle of attack = 17 deg.*

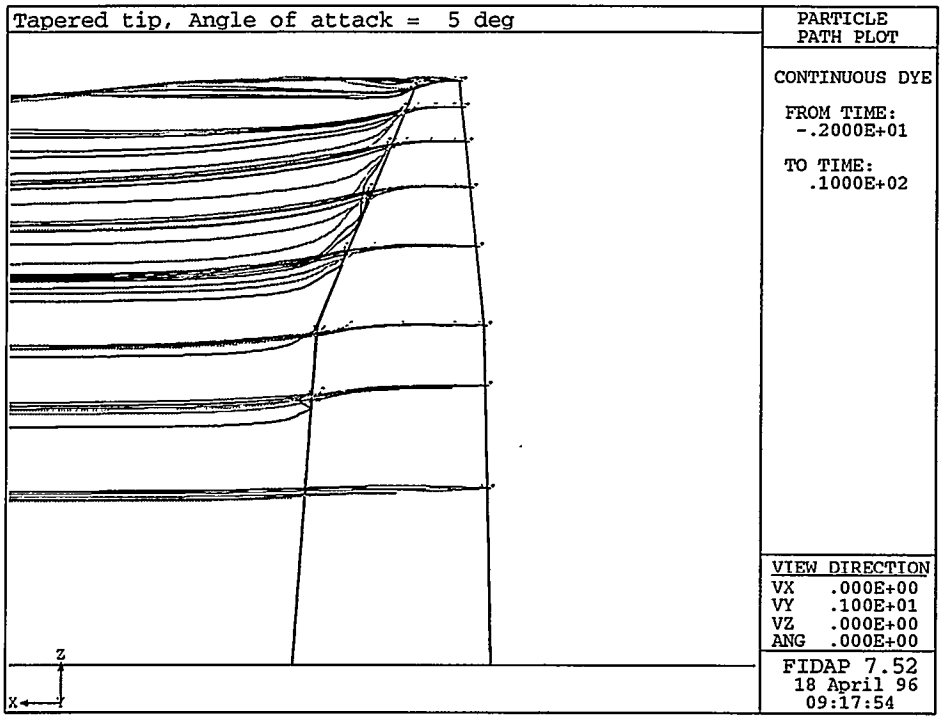

Figure A-13 *Particle trace of the fluid motion from the suction side, downstream from the blade for the tapered tip at an angle of attack = 5 deg.*

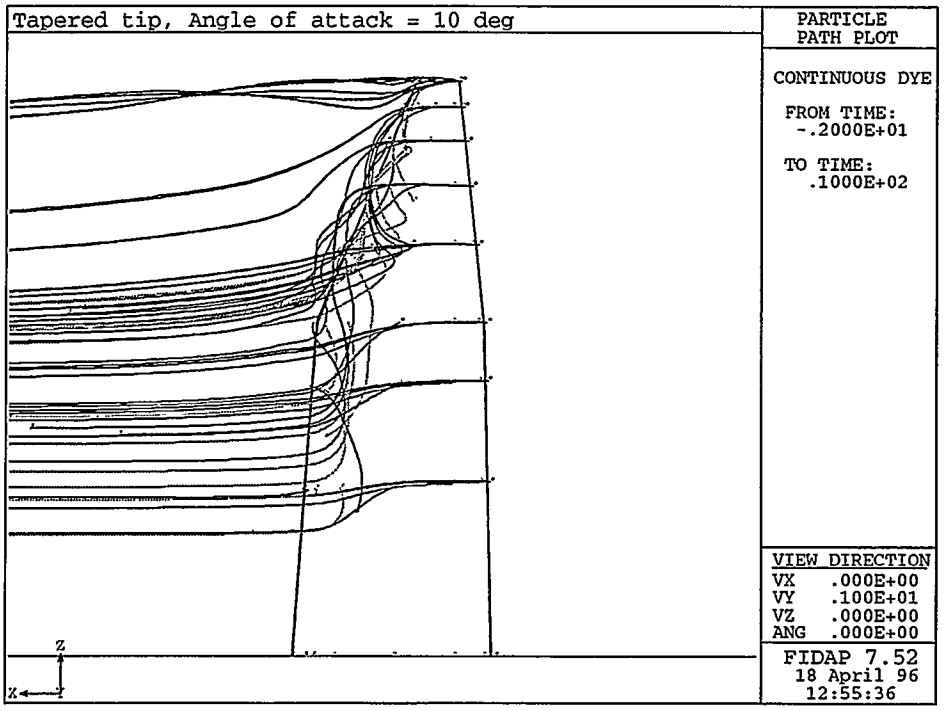

Figure A-14 *Particle trace of the fluid motion from the suction side, downstream from the blade for the tapered tip at an angle of attack = 10 deg.*

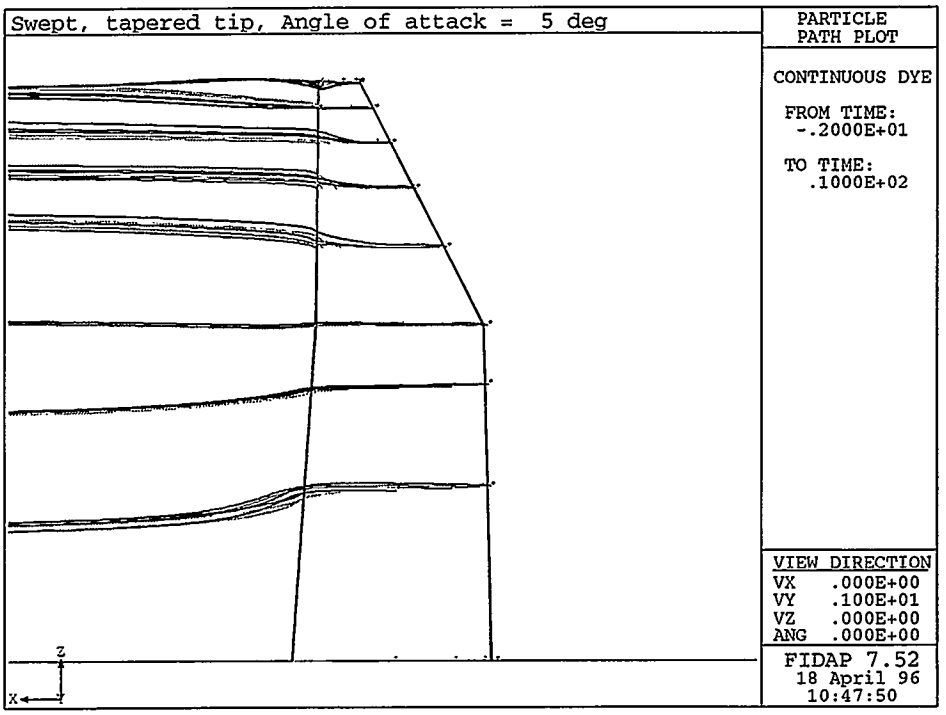

Figure A-15 *Particle trace of the fluid motion from the suction side, downstream from the blade for the swept, tapered tip at an angle of attack = 5 deg.*

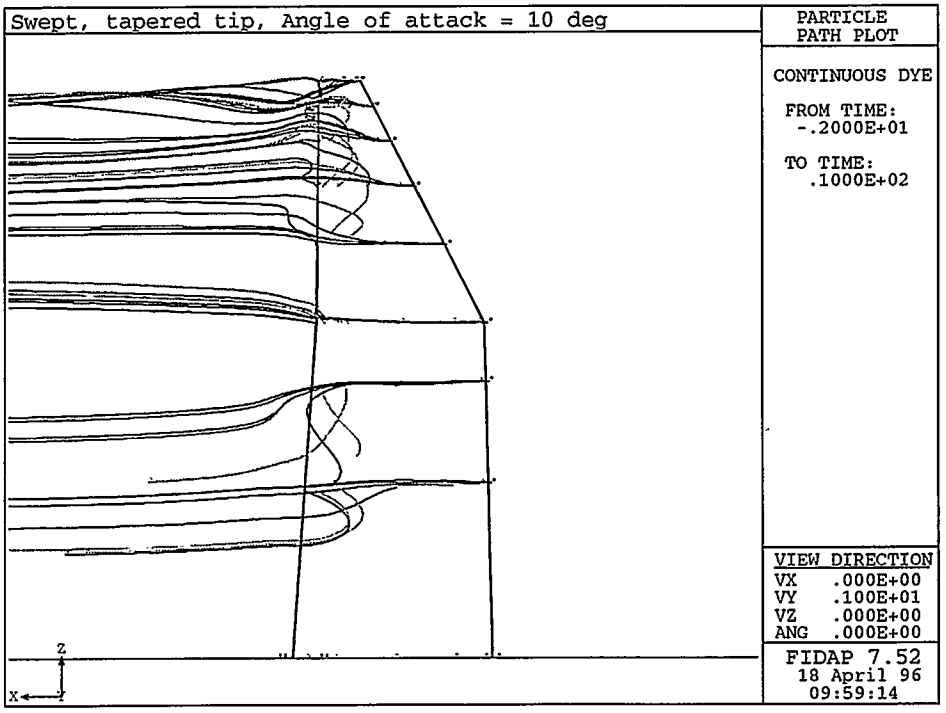

Figure A-16 *Particle trace of the fluid motion from the suction side, downstream from the blade for the swept, tapered tip at an angle of attack = 10 deg.*

Figure A-17 *Contour plot of local helicity in a plane perpendicular to the flow direction 0.5 chordlength downstream from the trailing edge for the rectangular tip at an angle of attack = 10 deg (corresponding to Figure A-2).*

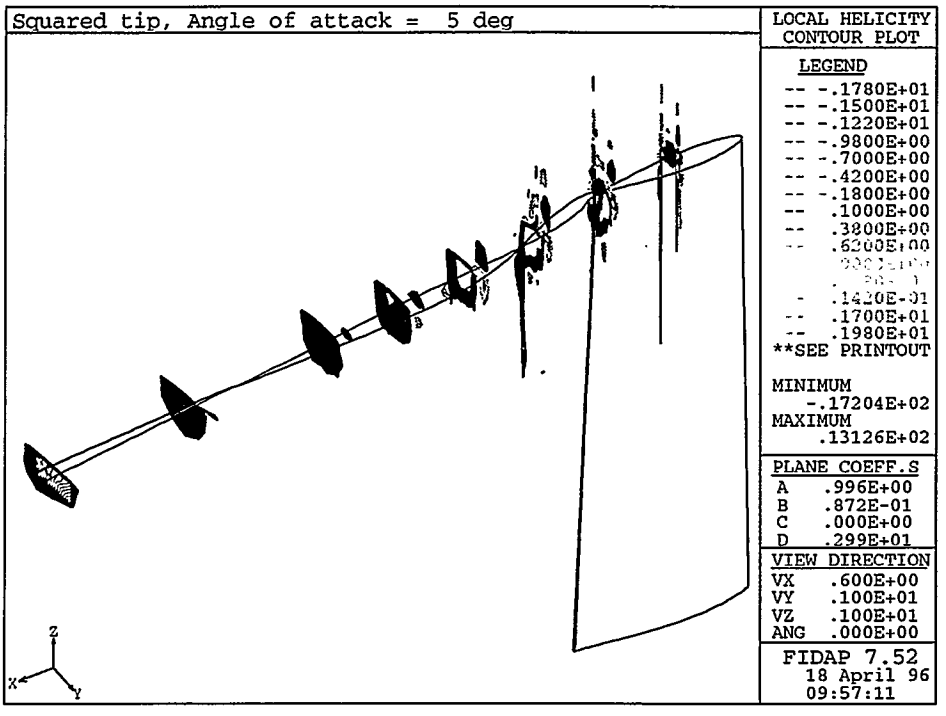

Figure A-18 *Contour plots of local helicity in planes perpendicular to the flow direction at different downstream locations from the trailing edge for the squared tip at an angle of attack = 5 deg.*

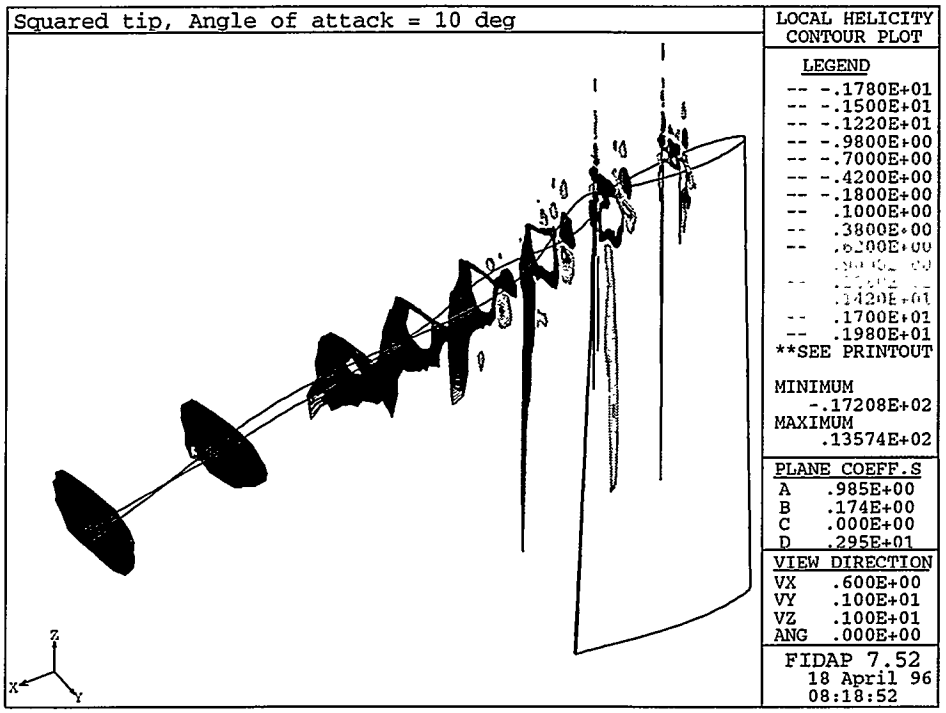

Figure A-19 *Contour plots of local helicity in planes perpendicular to the flow direction at different downstream locations from the trailing edge for the rectangular tip at an angle of attack = 10 deg*

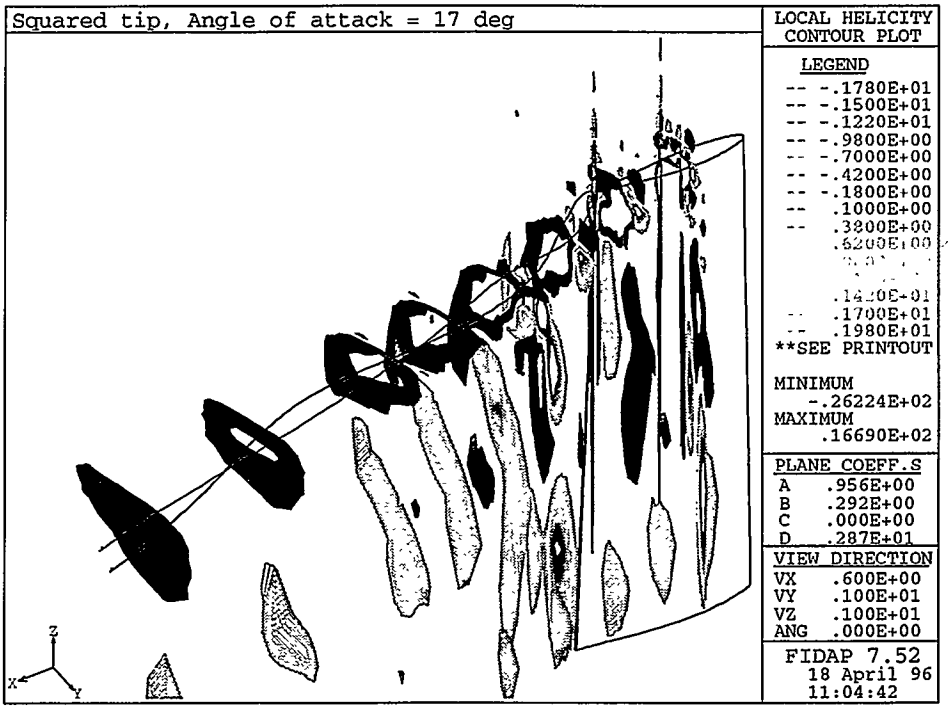

Figure A-20 *Contour plots of local helicity in planes perpendicular to the flow direction at different downstream locations from the trailing edge for the rectangular tip at an angle of attack = 17 deg.*

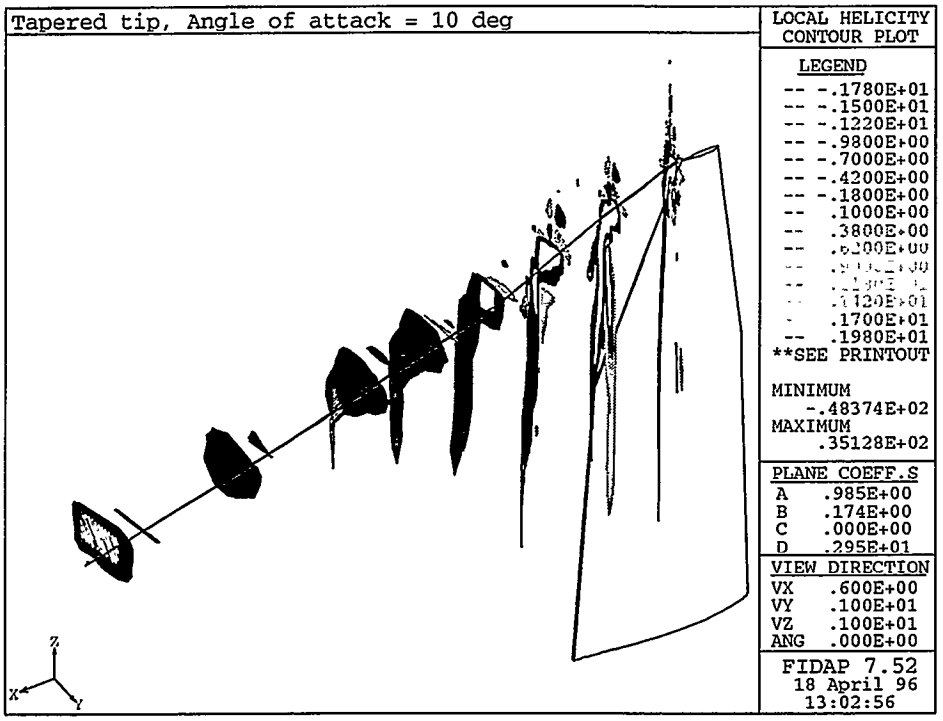

Figure A-21 *Contour plots of local helicity in planes perpendicular to the flow direction at different downstream locations from the trailing edge for the tapered tip at an angle of attack = 10 deg.*

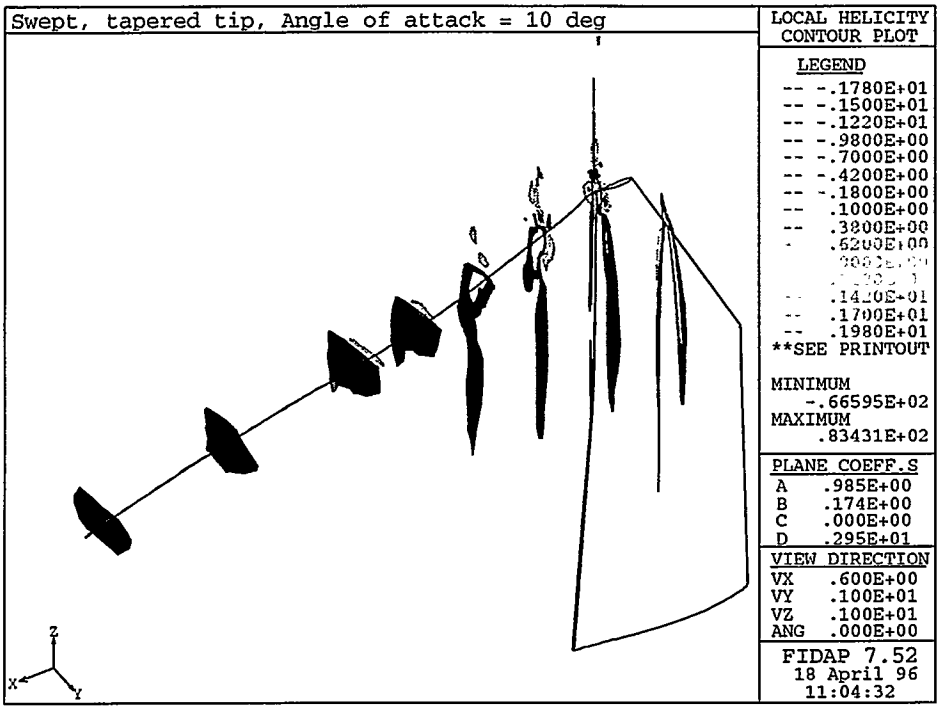

Figure A-22 *Contour plots of local helicity in planes perpendicular to the flow direction at different downstream locations from the trailing edge for the swept, tapered tip at an angle of attack = 10 deg.*

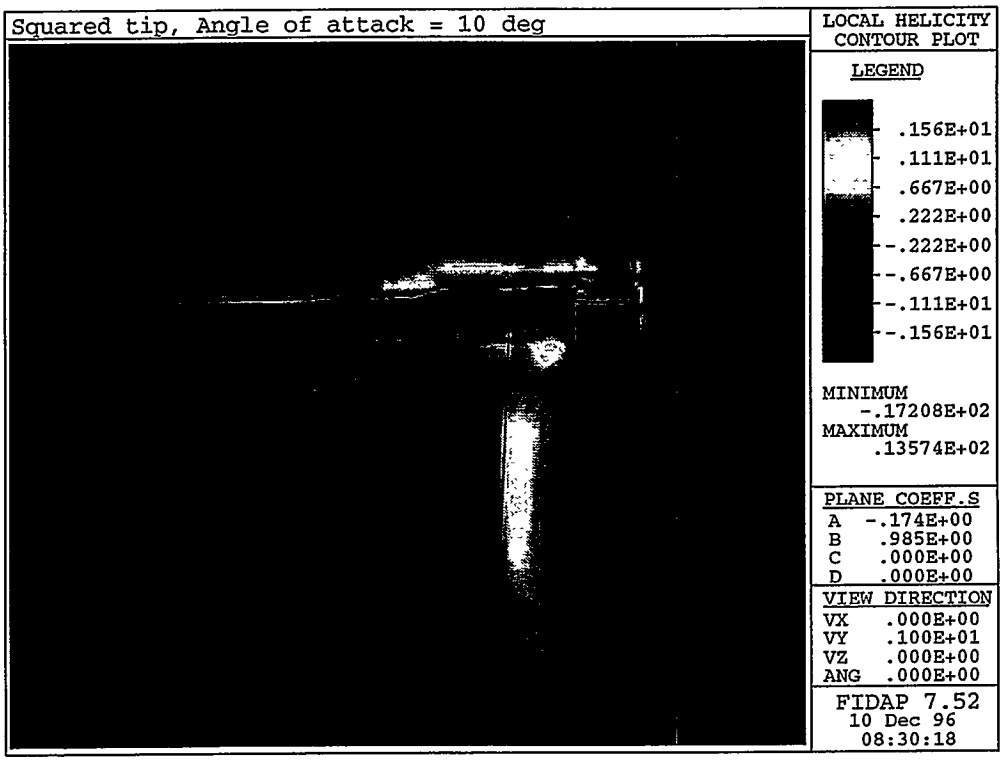

Figure A-23 *Contour plot of local helicity in a plane aligned with the flow direction for the rectangular tip at an angle of attack = 10 deg.*

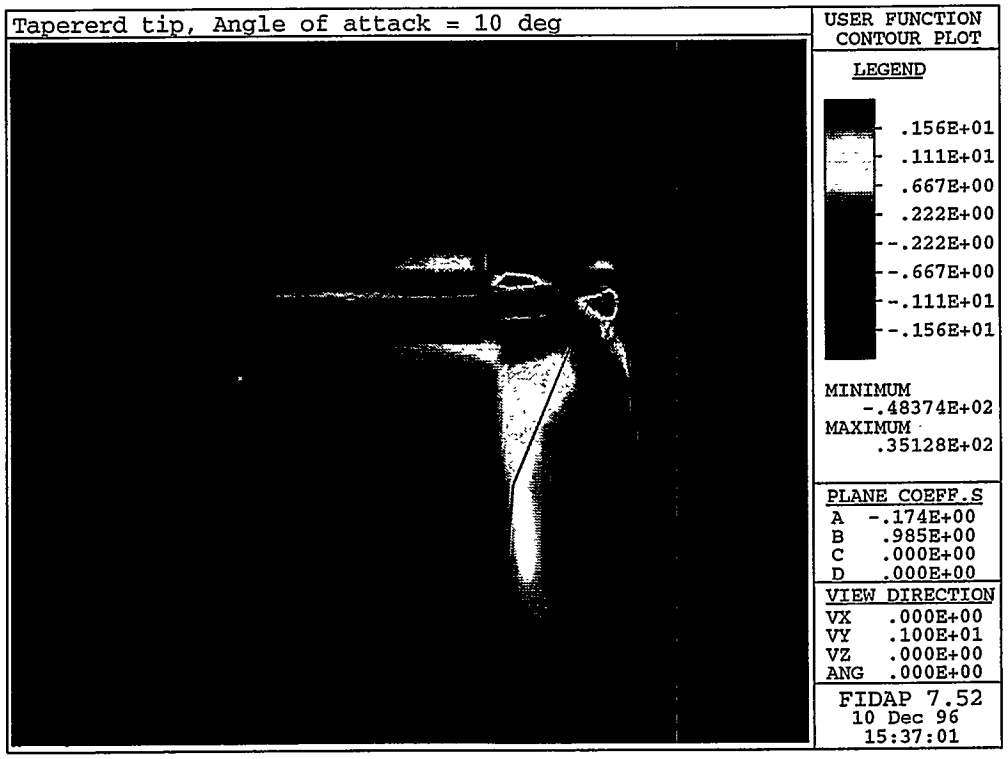

Figure A-24 *Contour plot of local helicity in a plane aligned with the flow direction for the tapered tip at an angle of attack = 10 deg.*

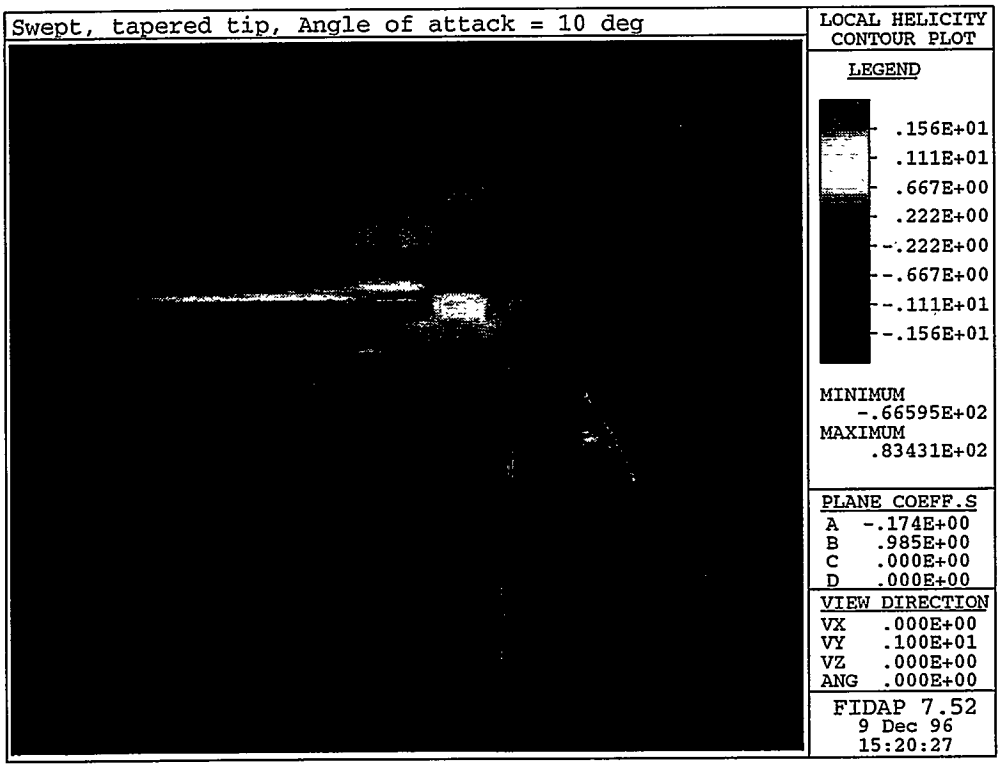

Figure A-25 *Contour plot of local helicity in a plane aligned with the flow direction for the swept, tapered tip at an angle of attack = 10 deg*

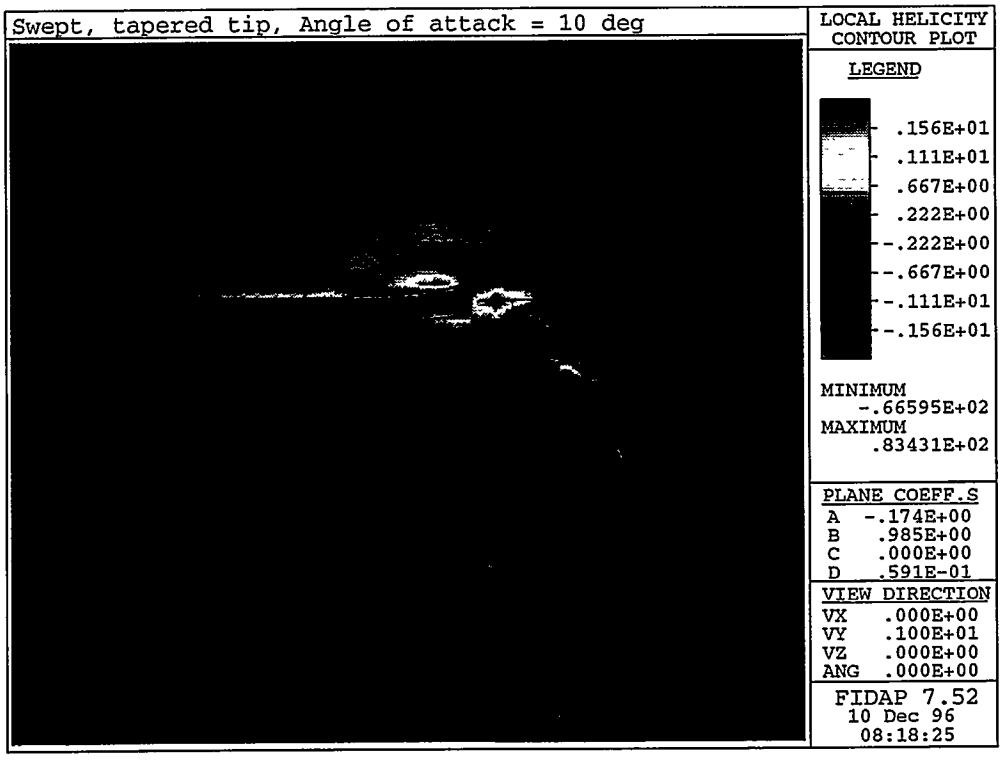

Figure A-26 *Contour plot of local helicity in a plane aligned with the flow direction for the swept, tapered tip at an angle of attack = 10 deg*

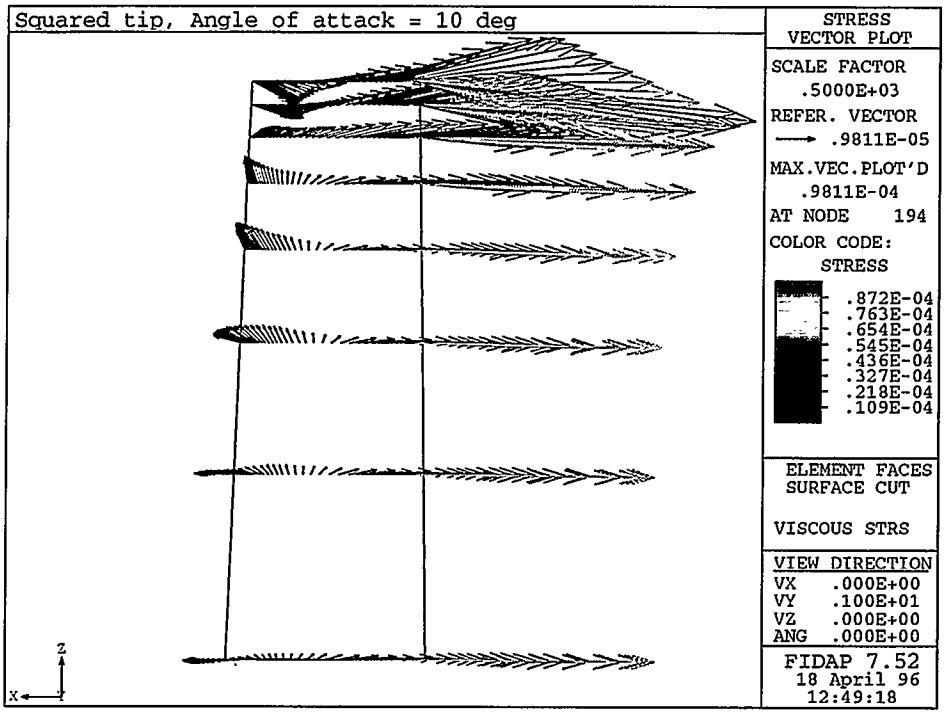

Figure A-27 *Vector plot of viscous force from the suction side surface acting on the fluid for the rectangular tip at an angle of attack = 10 deg.*

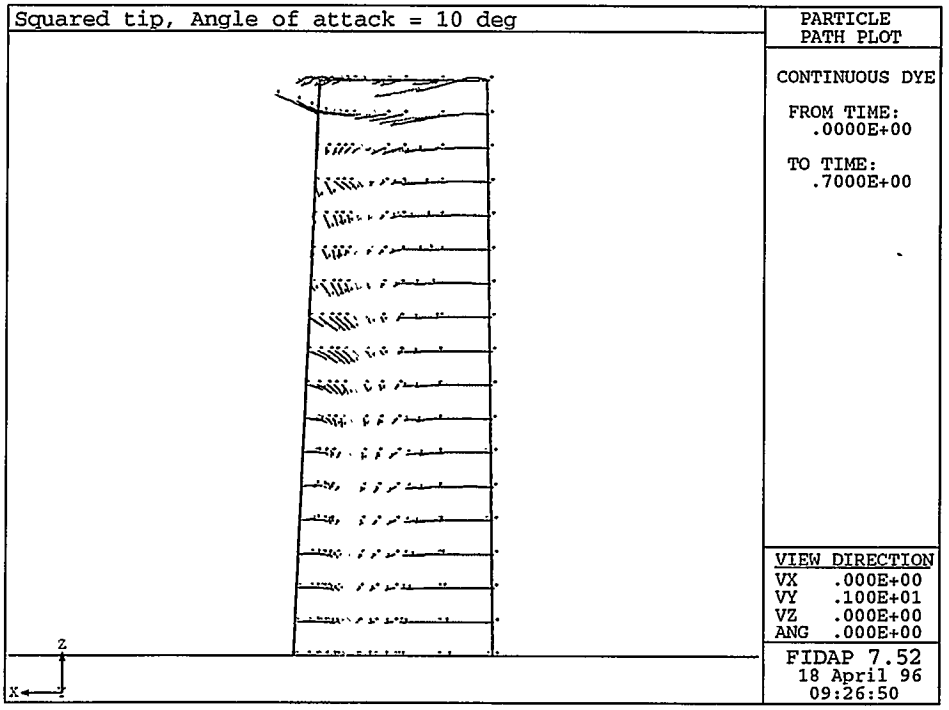

Figure A-28 *Particle trace of the fluid motion in the boundary layer of the suction side of the rectangular tip at an angle of attack = 10 deg.*

Bibliographic Data Sheet Risø-R-891(EN)

Title and author(s)

Numerical Investigation of Different Tip Shapes for Wind Turbine Blades
Aerodynamic and aeroacoustic aspects

Helge Aagaard Madsen, Peter Fuglsang

ISBN
87-550-2177-8

ISSN
0106-2840

Dept. or group
Test Station for Wind Turbines
Dept. of Meteorology and Wind Energy

Date
December 1996

Groups own reg. number(s)

Project/contract No.
ENS 1364/93-0006
ENS 1364/93-0001
ENS 1363/95-0001

Pages	Tables	Illustrations	References
83	0	90	29

Abstract (Max. 2000 char)
Aspects of the aerodynamics and aeroacoustics related to the design of the tip region of wind turbine blades are treated in the present report.

The aerodynamic optimization of the tip region is discussed and it is concluded that in principle there is no main difference to the optimization problem of the rest of the blade except that the performance of the aerodynamic models as, e.g., the blade element momentum theory (BEM) is more uncertain in this region due to the complex, three dimensional flow field. It is shown that an optimization of an entire blade in general leads to a slender tip with a chord decreasing to zero at the blade tip. Finally, the influence on the blade aerodynamics from minor changes of the planform in the tip region is illustrated.

Two common aeroacoustic models are reviewed. The aerodynamic input parameters to both models are the strength of the tip vortex and the length of the separated flow bubble formed by the tip vortex at the trailing edge. In the original aeroacoustic models these two parameters are calculated from empirical relations based on different experiments, e.g., using flow visualization. In the present work the two parameters was compared with the results of a CFD calculation of the flow around a rectangular shaped tip. The principal influence of sweep of the tip axis has also been investigated from detailed CFD simulations. It is found that sweeping the leading edge towards the trailing edge results in a stronger flow separation at moderate and high angles of attack compared to, when the trailing edge is swept towards the leading edge. This can have a considerable influence on the total loading on the blade. Similar tendencies have been found in full scale experiments.

At the end of the report the application of the results from the present study are discussed for practical tip design. As the tip noise is linked to the strength of the tip vortex and the extension of the separation region these two parameters should be reduced in order to lower the tip noise. Finally, a blade tip design with a nonseparating tip vortex (NSTV tip) is sketched and proposed as one way to reduce the tip noise.

Descriptors INIS/EDB
AERODYNAMICS, DESIGN, NOISE, NUMERICAL ANALYSIS, OPTIMIZATION, THREE-DIMENSIONAL CALCULATIONS, TURBINE BLADES, VORTEX FLOW

Available on request from:
Information Service Department, Risø National Laboratory (Afdelingen for Informationsservice, Forskningscenter Risø)
P.O. Box 49, DK-4000 Roskilde, Denmark
Phone (+45) 46 77 46 77, ext. 4004/4005 • Telex 43 116 • Fax (+45) 46 75 56 27

RISØ

Objective

Risø's objective is to provide society and industry with new opportunities for development in three main areas:

- *Energy technology and energy planning*
- *Environmental aspects of energy, industrial and agricultural production*
- *Materials and measuring techniques for industry*

In addition, Risø advises the authorities on nuclear issues.

Research profile

Risø's research is strategic, which means that it is long-term and directed towards areas in which technological solutions are called for, whether in Denmark or globally.
The research takes place within 11 programme areas:

- *Wind energy*
- *Energy materials and energy technologies for the future*
- *Energy planning*
- *Environmental impact of atmospheric processes*
- *Processes and cycling of matter in ecosystems*
- *Industrial safety*
- *Environmental aspects of agricultural production*
- *Nuclear safety and radiation protection*
- *Structural materials*
- *Materials with special physical and chemical properties*
- *Optical measurement techniques and information processing*

Transfer of Knowledge

Risø's research results are transferred to industry and authorities through:

- *Co-operation on research*
- *Co-operation in R&D consortia*
- *R&D clubs and exchange of researchers*
- *Centre for Advanced Technology*
- *Patenting and licencing activities*

And to the world of science through:

- *Publication activities*
- *Network co-operation*
- *PhD education and post docs*

Risø-R-891(EN)
ISBN 87-550-2177-8
ISSN 0106-2840

Available on request from:
Information Service Department
Risø National Laboratory
P.O. Box 49, DK-4000 Roskilde, Denmark
Phone +45 46 77 46 77, ext. 4004/4005
Telex 43116, Fax +45 46 75 56 27
http://www.risoe.dk
e-mail: risoe@risoe.dk

Key Figures

Risø has a staff of more than 900, including more than 300 researchers and 100 PhD students and post docs. Risø's 1996 budget totals DKK 471 m, of which 45 % come from research programmes and commercial contracts, while the remainder is covered by government appropriations.